Dottorato in Scienza e Tecnologia dei Materiali Innovativi

Roberto Jakomin

MOVPE GROWTH OF InP-BASED III-V COMPOUNDS DOPED WITH TRANSITION METALS (Fe,Mn)

Supervisor: Prof. Luciano Tarricone

Anno Accademico: 2007-2008

MOVPE GROWTH OF InP-BASED III-V COMPOUNDS DOPED WITH TRANSITION METALS (Fe,Mn)

Contents

Introduction……..………………………………………………6

Part I: Preparation and assessment of InP-based semiconductors

- **Chapter 1: III-V Semiconductor compounds**……………………………………...………….........11
    - 1.1 - General properties of Arsenides, Phosphides and Antimonides alloys……………………………..…........13
    - 1.2 - An outlook on Nitrides……………………..…......16
    - 1.3 - InGaP/GaAs……………….…………………..………18
    - 1.4 - InP/InP and InGaAs/InP...21
    - References I……………………………………………23
- **Chapter 2: An overview of the Metal-Organic-Vapor-Phase-Epitaxy**…………………...………………………………..…………...24
    - 2.1 - Introduction: Comparing MOVPE and MBE………………………………………………...24
    - 2.2 - General description of a MOVPE system………......25
    - 2.3 - Thermodynamics aspects…….……………………….27
    - 2.4 - Kinetics and mass transport………………………..29
        - 2.4.1 Reaction Kinetics………………………….30
        - 2.4.2 Homogeneous Reactions……………………31
        - 2.4.3 Heterogeneous Reactions……………………32
    - 2.5 - Growth regimes…...……………………………33
    - 2.6 - Fluidodynamics aspects……………….……………35

- 2.7 - Reactor pressure conditions………..…………….37
- 2.8 - Metal-organic precursors…...…………………….38
- 2.9 - MOVPE system at the Parma University…..……..40
- References II...44

- **Chapter 3: Diagnostic techniques**………………………..………45

- 3.1 Structural analysis
  - 3.1.1 RAS (Reflectance Anisotropy spectroscopy)…45
  - 3.1.2 HRXRD (High resolution X-ray diffraction)....50
  - 3.1.3 RBS (Rutherford backscattering spectroscopy)……………………………………..52
  - 3.1.4 PIXE (Proton induced X-ray emission) …….53
  - 3.1.5 SIMS (Secondary ions mass spectroscopy) …..54
- 3.2 Electrical analysis
  - 3.2.1 Hall effect measurements……..……………….56
  - 3.2.2 DLTS (Deep level transient spectroscopy)……61
  - 3.2.3 CV profiling and ECV (Etching Capacitance Voltage)…………………………………………..62
  - 3.2.4 I-V measurements……………………………..65
- 3.3 Optical analysis
  - 3.3.1 PL (Photoluminescence)..…………………….66
- References III……………………………………..68

Part II: Study of Iron implantation on InP-based layers grown by MOVPE……………………………………………..…69

- **Chapter 4: Ion Implantation**……………………….......................69

- 4.1 - The problem of realizing insulating regions in III-V semiconductors……………………………………….69
- 4.2 - The compensation effect………………………….....70
- 4.3 – The Iron role in InP and InGaP...............................71
- 4.4 - Ion implantation system……………………………72
  - 4.4.1 Comparison between Implantation and Diffusion……………………………….....…73
  - 4.4.2 Basic Physics of Implantation………………...75
- 4.5 - Implantation damages and annealing processes…….79

- References IV……………………………………………....81

- **Chapter 5: InGaP/GaAs**…………………………….……………82

  - 5.1 - Deposition of undoped InGaP/GaAs layers……..…82
  - 5.2 - Substrate preparation……………………………..83
  - 5.3 - InGaP/GaAs growth optimization…………………..84
  - 5.4 - Silicon doping..…………………………………..90
  - 5.5 - Study of InP and InGaP layers Implanted with Iron…………………………………………………92
    - 5.5.1 Electrical Measurements……..……..………96
    - 5.5.2 Structural analysis ………………………..100
  - 5.6 - Conclusions…………………………………..…104
  - References V……………………………………...…105

- **Chapter 6: InP growth optimization and InP:Zn re-growth on iron implanted InP**…………………………………...……106

  - 6.1 - Homoepitaxial growth of InP/InP(001)……..……106
  - 6.2 – Optimization of Zn doping…………………….....109
  - 6.3 - Study of the Zn diffusion ……………………...111
  - 6.4 - InP:Zn re-growth on InP substrates implanted with Iron…………………………………………………113
  - References VI………………………………………117

- **Chapter 7: InGaAs: preliminary results**..118

  - 7.1 - Substrate Treatment……………………………….118
  - 7.2 - Deposition of undoped InGaAs/InP layers………..118
  - 7.3 – Growth of n-doped InGaAs……………………….123
  - References VII……………………………………….125

Part III: MOVPE growth of InAsP/InP layers doped with a magnetic impurity (Mn)…………………………….126

- **Chapter 8: An introduction to Magnetic Semiconductors**….....126

  - 8.1 - Diluted Magnetic Semiconductors………………127

- 8.2 – The example of (Ga,Mn)As……………………….128
- 8.3 – Calculation of the Curie Temperature in DSM……………………..…………………………130
- Doping by ion implantation…………………………..133
- References VIII………………………………………135

- **Chapter 9: Tailoring of Mn-Acceptor depth in InAsP grown by MOVPE**……………………………………………………………136

- 9.1 - Introduction to the InAsP:Mn/InP system……...…136
- 9.2 - Growth of InAsP/InP Mn doped…………………..138
- 9.3 - HRXRD analysis……………………………………140
- 9.4 - RAS analysis..................……………………..……142
  - 9.4.1 Total Reflectance analysis……………..…142
  - 9.4.2 Reflectance anisotropy………..…………144
- 9.5 - Determination of Mn acceptor depth by Hall measurements…………………………………………...150
- 9.6 - PL measurements…………….…………...……….153
- 9.7 - Conclusions………………………………………158
- References IX…………………………………………161

Conclusions……………………………………………………162

Thanks to……………………………..………………………167

Introduction

The research on electronic and optical devices is oriented towards new material classes able to replace the traditional Silicon or Gallium Arsenide, due to their specific interesting features. The development of advanced epitaxial deposition techniques, in particular MOVPE and MBE, grant to obtain high purity structures, based on III-V semiconductors, also constituted by ternary or quaternary alloys. The flexibility of III-V semiconductors is a point of strong interest, thanks to their capability to cover applications over a large spectral range. The energy gap of the III-V semiconductors alloys, intended like Arsenic, Phosphorous or Antimony based, embraces a range between 0.18 and 2.42 eV, opening the possibility of optical communication applications, lasers and LEDs (from IR up to green). On the other hand, the advantageous electrical characteristics of III-V semiconductors allow their use in high frequency microelectronic devices, like HEMTs (High Electron Mobility Transistors) and HBTs (Heterojunction Bipolar Transistors).
By virtues of lower maintenance costs and the possibility of depositing on large areas substrates, MOVPE permits a massive production for industrial applications. Moreover, together with the other epitaxial methods, it allows a great control of the alloy composition, enabling the so called "band gap engineering", that means the achievement of a precise composition corresponding to a specific energy, depending on a desired application [1].
In the last years, the study and the production of InGaAsP based materials, lattice matched to GaAs or InP substrates, have found attention, having the advantage, in comparison with the Al-based alloys, to realize devices less reactive with Oxygen.
Instead of the more used GaAs, the new devices are based on InGaP/GaAs and InGaAs/InP heterostructures, because of their even better electrical characteristics (higher mobilities) and their specific optical features (in the case of InGaAs, a low Energy band gap of 0.8eV allows the realization of devices in the IR spectral region). For what concerns photovoltaic applications, they can contribute to reach solar cells with 30% of efficiency conversion and, in the microelectronic field, they make the high frequency devices able to get up 350 GHz regimes and even more.
Then, the choice to exploit different semiconductor systems to form heterostructures can lead to improvements for device performances. The $In_{0,48}Ga_{0,52}P$/GaAs heterostructure, for example,

represents a promising configuration for n-p-n HBT, thanks to the low conduction band discontinuity added to the high valence band discontinuity, favoring an efficient electron injection from the emitter to the base of the transistor [2,3].

The use of Silicon for planar technology, essential to fabricate microelectronic devices, is still more advantageous, especially thanks to the availability of its stable oxide to realize insulating matrixes or even high selective insulating regions. This could represent a strong drawback for III-V semiconductors, where the lack of stable oxides for the realization of high resistivity regions requires more difficult processes, like photolithographic methods and selective etching for "mesa" structures construction. A valid alternative is instead represented by the compensation effect, introducing a certain amount of an element, Iron, for example, able to introduce deep levels in the III-V semiconductor energy gap. The formation of deep centres, that contribute to trap the majority carriers, limits the transport and creates high resistivity areas. The simplest way for introducing such species is just during the deposition process or using diffusion techniques that operate in thermodynamical equilibrium.

However, the thermodynamic equilibrium techniques meet the obstacle of the solid state solubility limit, the concentration over which the host atoms cannot be incorporated without forming precipitates or complex species. Aiming to solve this limitation, a non-equilibrium technique like ion implantation can be used. The ion implantation is not only able to incorporate high concentration of elements beyond the solid solubility into the layer (Fe can for example overcome $10^{19}cm^{-3}$ in InP- based materials), but it is also important to form very selective semi-insulating regions and a well controlled doping profile [4]. In this case, however, some annealing treatments after implantation are necessary to recover the material, because the ions impact is responsible of lattice distortion and therefore structural defects that would prejudice the electrical and structural material quality. A large experience was developed on iron implantation into InP and in the following works on InGaP/GaAs, showing in both materials a good recovering of the damage caused by ion implantation after annealing processes [5,6].

The present PhD work is aimed to extend the study of Iron implantation effect on InGaP with different doping levels. To this purpose, a systematic study of the growth of InGaP on GaAs was performed, searching the best conditions for a lattice matched deposition, with a minimum background doping. Moreover, detailed analyses on structural, optical and electrical properties have been carried out. In this way, an optimization of silicon doping was performed. The n-doped InGaP samples were implanted with Iron to analyze more in details the role of Iron in compensation effects and its lattice collocation, considering that it is electrically active if it occupies a substitutional lattice site. Therefore, its substitutional fraction site was observed to change as a function of the

temperature by virtue of the electrical analysis, indispensable to verify the compensation effect for the realization of semi-insulating regions.
The Iron ion implantation was also intended to be extended to other III-V material systems, like InGaAs/InP, always starting from the growth optimization of unimplanted materials. Another important study, when one aims to integrate the implantation step in a microelectronic technology process, is to observe the influence between implanted Iron and other doping species. This purpose was pursued by performing an homoepitaxial re-growth of InP:Zn (p) doped on a InP substrate, previously Iron implanted. After that, we analyzed by SIMS the influence between Iron and Zinc, taking in consideration the high mobility of this latter species when it is diluted into III-V semiconductors.
Another investigated topic was suggested by the intention to explore the possibility of realizing magnetic semiconductors, through the introduction of Manganese in a InAsP/InP system, to form a so called diluted magnetic semiconductor [7,8]. In this way, the property of Mn to provide at the same time holes and magnetic dipoles were exploited. Due to the low solid solubility of Mn in III-V semiconductors and considering that a high holes concentration is necessary to obtain magnetic effects, another solution was proposed. Changing the As content in the alloy, a tailoring of the Mn level depth in the energy gap was performed, to obtain an increase of acceptor activation without overcoming the Mn solid solubility, responsible of clusters formations. The growth optimization of InAsP:Mn was monitored by a RAS system, operating during the deposition, able to analyze the surface reconstruction quality.

This PhD work was carried out thanks to the coordination of the following research groups. The InGaP, InP and InGaAs material growth optimization, PL analysis and electrical measurements were performed at the SEMLABS group of Physics Department at the Parma University. The iron implantation, RBS, PIXE and SIMS analysis were performed by Prof. Andrea Gasparotto and his workgroup at the Padova University, and realized at Legnaro (PD) Nuclear Physics laboratories. The post-implantation electrical measurements, I-V and DLTS, were performed by Dr. Beatrice Fraboni at the University of Bologna. The InAsP:Mn growth controlled by RAS were performed at the Physics Department of the Technische Universität Berlin in a collaboration with the workgroup of Prof. Michael Kneissl.

The topics of this thesis are presented as follows:

- The first part is introductive, regarding the preparation and assessment of InP-based materials. After an introduction on III-V semiconductors, the MOVPE deposition system is

briefly described. Then an overview on ion implantation is given, considering both technological aspects and some recent results in specific materials like InP and InGaP. After that, different measurement techniques used in this PhD work, will be described.

- The second part is on the study of iron implantation in InP-based materials. In particular, the MOVPE growth optimization of undoped and doped InGaP/GaAs, and the experimental evidences of iron compensation effect after implantation are shown. We present the growth optimization of InP, the study of Zn diffusion during deposition and the re-growth of InP:Zn layers on InP implanted with Iron, such that the observation of Zn-Fe inter-diffusion effects is possible by SIMS analysis. Moreover, preliminary results on InGaAs growth and optimization are presented.

- The third part involves a preliminary study on magnetic semiconductors; specifically, it concerns the obtained results on doped InAsP:Mn. After a brief introduction on spintronic and diluted magnetic semiconductors, the main argument is the activity on tailoring of Mn-acceptor depth in InAsP grown by MOVPE.

- In the last chapter the conclusions on this work are derived.

References

[1] Razeghi M., The MOCVD Challenge Vol.2 Institute of Physics Publishing, Bristol and Philadelphia, (1995)

[2] H.Kroemer, J.Vac.Sci.Techn.B1, 126(1983)

[3] F. Alexandre, J. L. Benchimol, P. Launay, J. Dangla and C. Dubon-Chevallier, Solid State electronics, 38, 9.pp.1667-1674 (1995)

[4] S.Lourdudoss and R. Holz, J.Cryst.Growth, 371-381, 179 (1997)

[5] Cesca T., Gasparotto A., Mattei G., Rampazzo V., Boscherini F., Fraboni B., Priolo F., Ciatto G., D'Acapito F., Bocchi C., Phys.Rev.B 68 (2003) 224113

[6] T. Cesca, A. Gasparotto, A. Verna, B. Fraboni, G. Impellizzeri, F. Priolo, L. Tarricone and M. Longo, Nucl.Instr.and Meth.B 242, 653 (2006)

[7] H. Ohno, A. Shen, F. Matsukura, A. Oiwa, A. Endo, S. Katsumoto, and Y. Iye., Appl.Phys.Lett. 69, 363 (1996)

[8] T. Story, R. R. Gaazka, R. B. Frankel, and P. A. Wolff., Phys. Rev. Lett. 56, 777 (1986)

Part 1: PREPARATION AND ASSESSMENT OF InP-BASED SEMICONDUCTORS

Chapter 1

III-V Semiconductor compounds

In the last years, the III-V semiconductors always deserved more space both in fundamental studies and in technological development, due to their wide applications in optoelectronic and high velocity microelectronic devices. Though Silicon covers even today the 95 % of the semiconductors market, the better performances of the III-V semiconductors in terms of higher mobilities, radiative recombination efficiency and better fitting with the spectral bandwidth, required from optical communication aspects, justify the growing interest of the researchers in this field.

The largest part of the III-V semiconductors is characterized by a direct band gap energy, which allows more efficient radiative transitions than in the case of an indirect gap material, like as for example Silicon. In this latter case, in fact, the assistance of lattice vibrations is necessary to permit a band to band transition. A more efficient radiative recombination represents a big advantage for what concerns optoelectronic applications. Moreover, III-V semiconductors have low carriers effective mass, therefore higher electronic mobilities that imply the possibility to realize high frequency electronic devices, up to 600 GHz [1.1].

Nevertheless, the realization of Silicon based devices remains still convenient because of the lower costs, the simpler growth (that permits to obtain large wafers, even up to 300 mm diameter in comparison with the 150 mm of GaAs) and the possibility to use the well known and relatively simple technique of the Silicon di-oxide (SiO_2) technology for integrated circuit applications. The latter is really an important aspect, because GaAs and the other III-V semiconductors cannot form a stabilized oxide layer over the surface, as SiO_2 for Si, and they are always characterized by an unavoidable background doping. These are certainly big drawbacks since microelectronic devices

require semi-insulating areas to confine the carriers in the active regions, such to limit current losses.
However, the evolution of the semiconductors growth methods, especially vapour phase epitaxy such as MBE (Molecular Beam Epitaxy) and MOVPE (Metal-Organic Vapour Phase Epitaxy) nowadays grant a high purity and controlled ultra-thin or bulk-like layer deposition.
These techniques allow epitaxial layer depositions, namely lattice matched to the substrate, that means a single crystal growth with thickness and doping control. The III-V semiconductors are composed by elements of the third and the fifth group in the periodic table, in the simplest case they are formed by a binary alloy in the 1:1 stoichiometric ratio. If the aim is to realize ternary or quaternary alloys, the vapour phase deposition techniques result really convenient. In fact, vapour phase techniques grant a good control of single elements incorporation, much better than in the case of melting growth, especially in materials with an incongruent melting. From this point of view, we can understand some of the main advantages of III-V semiconductors: (i) a composition flexibility, (ii) mixibility in large compositional ranges, (iii) the possibility to modulate the alloys composition to fit it with the required characteristics, in this way the desired energy band gap value (band gap engineering) is obtainable.
In particular, in a $III_xIII_{1-x}V$,$IIIV_xV_{1-x}$ type alloy, we observe the following empirical law that gives the composition as a function of the energy band gap value of the material:

$$E_g(x)=E_g(0)+bx+cx^2 \quad [1]$$

Where E_g (0) is the smallest bandgap among the starting binary compounds and c is the curvature parameter, which can be theoretically calculated.

In the case of MOVPE it is possible to perform large scale depositions, essential in the industrial production, with the deposition on 10 inches diameter substrates, in the so called planetary reactors, able to contain up to 30 substrates. It is not indeed surprising that today the biggest industries occupied in the semiconductors devices realization have many MOVPE implants available.
The possible technological applications of III-V semiconductors include several fields, and for these reason many important devices are involved. For example HBT (Hetero Bipolar Transistors), SDHT (Selectively Doped Heterojunction Transistors), HEMT (High Electron Mobility Transistors), FET (Field Effect Transistors), MOSFET (Metal Oxide-Semiconductor Transistors), MODFET (Modulation Doped Field Effect Transistor), TEGFET (Two-Dimensional electron Gas Field Transistors), high efficiency photovoltaic conversion solar cells, photodetectors, laser diodes,

VCSEL (Vertical Cavity Surface Emitting Laser) LED (Light Emitting Diodes), modulators, optical memories and so on.

1.1 General properties of Arsenides, Phosphides and Antimonides alloys

III-V compounds and their alloys are generally classified as Arsenides, Phosphides, Antimonides and Nitrides (namely As, P, Sb and N based). Apart from the case of Nitrides, under appropriate conditions of vapour phase growth, they can be grown lattice matched to proper substrates, therefore in principal dislocation free. Substrates as GaAs or InP are commercially available, easily produced and not really expansive, grown by melt techniques like Bridgman or Czochralski.
The opportunity to combine different species in ternary or even quaternary alloys makes the III-Vs based on arsenic, phosphorous and antimony, able to cover a large range of the electromagnetic spectrum, from 0.17 eV of InSb, an IR energy, up to 2.2 eV of GaP, at the energy of the green light. Their typical crystalline structure is the same of the IV element group, the Zinc blend structure. In this case the cell is constituted by two central faced sublattices, translated by ¾ along the diagonal direction. The basic cell is formed by two atoms, one of the III (cation) and the other of the V group (anion). If we consider the first, A atom, in the (0,0,0) position, the first neighbour of the B specie, displaced of d=1/4(1,1,1), is in the (1/4,1/4,1/4) position (fig.1.1).

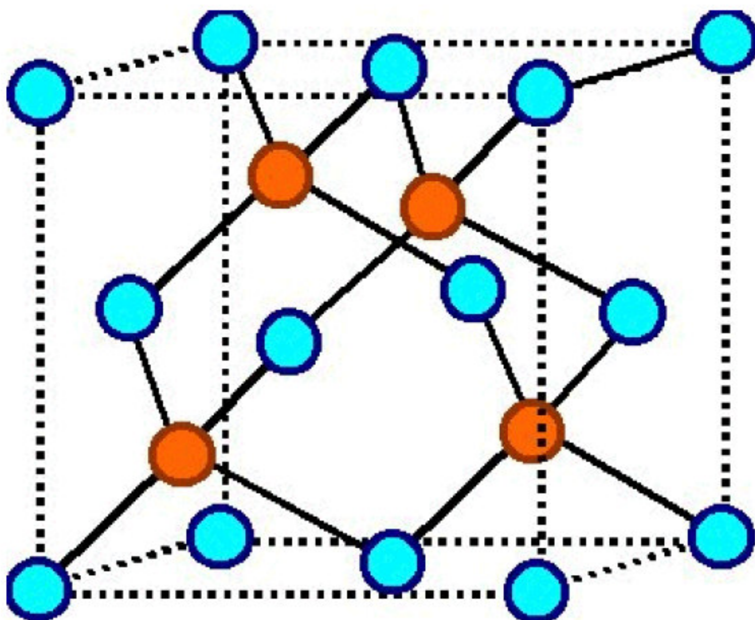

Fig.1.1: Face Centred Cubic lattice (fcc) where the unit cell is formed by two atoms, in (0,0,0) and in (1/4,1/4,1/4) positions.

As shown in table 1.1, the As and P based semiconductors have also very low effective masses, so that they can present very high electronic mobilities.

Semiconductor	**Energy gap (eV) at 300K**	**Lattice parameter (Å)**	**Effective mass (m_e/m_0)**	**Gap's type**
Si	1.12	0.54311	0.98	Indirect
Ge	0.66	0.565791 nm	1.64	Indirect
GaAs	1.424	5.65321	0.065	Direct
GaP	2.26	5.45117	0.35	Indirect
GaSb	0.73	6.09593	0.044	Direct
AlSb	1.58	6.1335	0.39	Indirect
AlAs	2.16	5.6622	0.11	Indirect
InP	1.35	5.86875	0.078	Direct
InSb	0.17	6.47937	0.0145	Direct
InAs	0.36	6.0584	0.022	Direct

Tab.1.1: Some physical constants of the main III-V Semiconductors compared with Si and Ge [1.14]

Here, an important aspect, in particular for the production of high frequency devices, is the lower effective mass of III-V materials if compared with that of Silicon. The most important material among the III-Vs is certainly GaAs. Its popularity is due both to the simplicity of its realization from the melt and its interesting properties.

If we consider the history, already since the eighties, it was possible to obtain GaAs by MOVPE with very good characteristics; working at opportune conditions, these samples showed a mobility of 127000 cm^2/Vs at 77K [1.2].

The excellent properties proved by GaAs soon to the fabrication of optimum performance FETs and HEMTs. On the other hand GaAs exhibits fundamental optical properties, a direct band gap and an emission peak, around 1.42 eV at 300 K that matches more or less with the energy of maximum intensity emission for the black body spectrum, property that makes it really suitable for

photovoltaic applications. The tandem cell composed by GaAs and InGaP together are characterized by a high conversion efficiency, over 30% [1.3]. They exploit the different energy gap of the InGaP lattice matched deposited over GaAs, around 1.9 eV, with respect to GaAs, extending the absorption range of the cell toward higher energies, thus giving a considerable increase of the efficiency.

An alloy like AlGaAs, characterized by a higher Energy gap and high refractive index, can be used as a window layer in solar cells. In fact, the window layer must be crossed by the solar light and is grown on the top of the structure in order to prevent that many surface defects are incorporated in the active layer below. Then, thanks to its higher refractive index with respect to the active region, it can minimize the reflection of the incident beam [1.4]. An advantageous aspect is also that the $Ga_xAl_{1-x}As$ alloy parameter is almost the same of GaAs, with a maximum mismatch of 0,14% [1.5]. Anyway, the great drawback of this kind of structures is the high reactivity of Al with Oxygen, which induces to prefer some other semiconductors.

Another As based material has instead interesting properties, due to a lower Energy Gap: InGaAs. It is used for detectors at the wavelength of 1.6 µm (or infrared cameras) or again for high velocity electronic devices, because of its high mobility (11900 cm^2/Vs at RT) [1.6].

In general, the flexibility of III-V semiconductors in terms of stoichiometry, their relatively simple lattice matched growth, the good thickness control and the easiness of the doping give the possibility of realizing also complex structures like Multi Quantum Wells (where an alternate sequence of nanometric thick layers of different materials is grown, for example InGaAs/InP or InGaP/GaAs). The elevate control of the layer thickness makes, indeed, possible the realization of very thin layers, from 1 to 10 nm, able to reach a carrier confinement along one or more directions. This permits the exploitation of quantum properties that contribute to enhance the devices performances, so that more efficient LEDs, LASERs or solar cells are possible [1.7, 1.8].

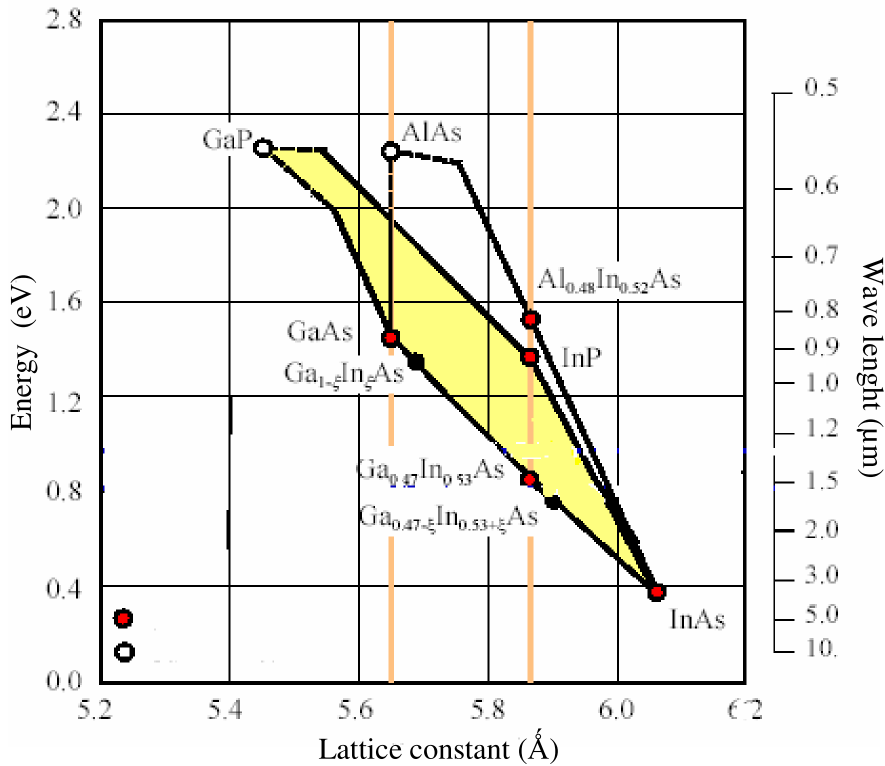

Fig.1.2: Energy gap and lattice constant of the most common III-V alloys.

1.2 An outlook on Nitrides

To understand why the interest in N based semiconductors is recently so much increasing, it is enough to have a look at their band gap range. A huge range is in fact covered, corresponding to a spectral width from IR for InN (0.8 eV) to UV for AlN (6 eV). Thanks to the nitrides, it is nowadays possible to produce blue led and lasers.

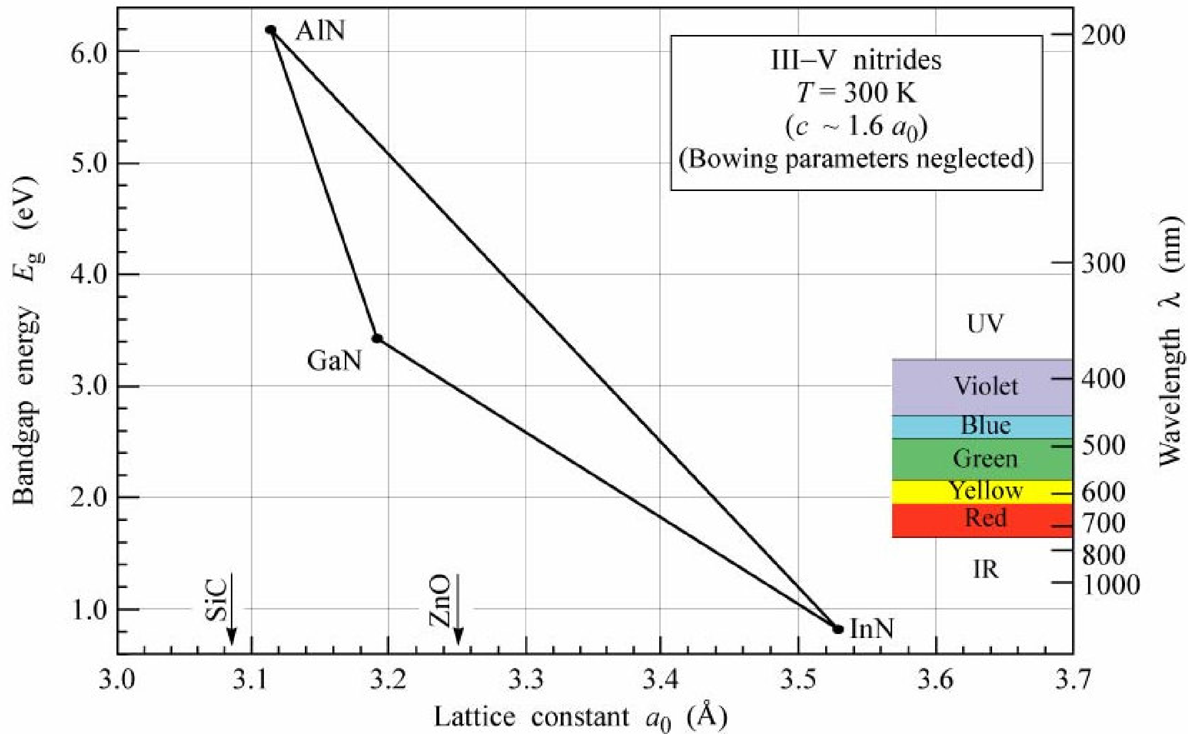

Fig.1.3: Energy gap of the most common Nitrides

The possibility to use the blue laser for the information storing has the consequence to enormously improve the available optical memories. Moreover, the realization of white light LEDs should cause, in the next future, the entire replacement of the old Tungsten bulbs with the new LED for ordinary illumination, in the way to obtain a considerably energetic saving and longer lifetimes.

The physical aspects of nitrides are different from the others III-V and their study was only recently performed. First of all, they grow, in most conditions, following a wurtzite structure; in other, less frequent conditions, they form a cubic centred body structure as the other III-Vs, when the periodic ABCABCABC structure takes the place of the hexagonal ABABAB.

The wurtzite phase is constituted by two hexagonal sublattices hcp (hexagonal closed packed), each formed by one of the alloy atoms, with a displacement along the c axe direction of 5/8 of the height cell.

Because high melting temperatures and dissociation pressures characterize the nitrides, the achievement of single macro-crystals is very complex. From this, it follows that the III-N based substrates are not so common and quite expansive, therefore normally different substrates are used. The most common is sapphire (Al_2O_3) largely used for GaN growth; but it has a different lattice parameter with respect to the grown layer, with the consequence of generating dislocations, due to the lattice mismatch.   Alternative substrates are SiC, Si, ZnO or GaAs, but each of them still

presents problems that actually bring to prefer sapphire. The possibility to obtain bulk GaN from LPE (Liquid Phase Epitaxy) at high pressure is currently studied, but it is naturally still complex to have big crystals in these conditions.

The absence of a lattice matched substrate leads to the growth of dislocations rich materials, particularly in the case of high thicknesses. Moreover, by considering also the different thermal expansion coefficients of substrate and deposited layer, during the post growth cooling, a thermal strain is originated that introduces further defects. The formed dislocations can reach density values around 10^{10} /cm^{-2}. But the extraordinary aspect of these materials is that even if the dislocation density is so high, the LED efficiency is not really sensitive to this, as in the other III-V case (where, for example in the AlGaAs or GaAsP case, a dislocation density of 10^3 cm^{-3} comes to have effects on the efficiency). In the nitride case, dislocations are not efficient recombination centres and it is possible to achieve high efficiency optical devices even with a defect concentration of more than six orders of magnitude higher than in the phosphides and arsenides case.

Nevertheless, other problems are connected with the growth: the high N_2 vapour pressure and the relative problems with p type doping.

The higher volatility of Nitrogen, respect to the other V elements, represents a substantial difficulty in the MOVPE growth. It is indeed in contrast with the necessity to use high growth temperatures to obtain good crystalline quality layers (typically, for a MOVPE growth of GaN, temperatures over 800°C are necessary). Consequently, a high density of N vacancies is generated. They act as donors centres, carrying the unintentional n carriers concentration to above 10^{19} cm^{-3} [1.9].

However, the evolution of vapour phase growth techniques granted the possibilities to obtain also complex structures characterized by high quality and efficiency. For example, InGaN/GaN based quantum wells for LEDs and displays are already available in commerce [1.10].

1.3 InGaP/GaAs

After this brief overview on III-V semiconductors, we focus particular attention to those materials studied in this PhD work and about which the experimental aspects, features and properties will be treated in the next chapters.

A particular technological interest regards the InGaP/GaAs structure, in which an InGaP layer is deposited on a GaAs substrate. The two semiconductors that form this heterostructure have different

properties, which optimally fit for defined applications, like the already mentioned solar cells for example.

Gallium arsenide (with a lattice parameter of 5.56 Ams and an Energy gap of 1.424 eV at 300K) is an extremely interesting material, as already said, thanks to its high mobility, ten times more than Silicon, and its direct energy gap. Moreover, it can be easily grown from the melt, providing relatively cheap wafers, useful for the vapour phase growth. In addition, GaAs based devices can operate at higher power levels than Silicon based ones, allowing applications in mobile telephony, satellite communication, exploiting higher breakdown voltages.

InGaP can be matched to GaAs, when the Indium molar fraction is 48.84% and Gallium, consequentially, is the 51,2%, yielding an Energy gap of 1.88 eV (at room temperature).

$In_{0.48}Ga_{0.52}P$, has interesting properties like a low electron effective mass, 0.111 m_0, high mobility (1850 cm^2/Vs at room temperature) and a direct band gap [1.11]. It can be mainly used in HEMTs, HCTs, pumping lasers for optical fibre amplifiers, doped with Erbium [1.12], but also for tandem cells in space applications and in combination with Al (AlGaInP) for high efficiency LEDs (emitting in green, yellow, orange and orange-red colours light).

In comparison with the Al based structures, the InGaP/GaAs heterostructure lattice matched grown, has a poor reactivity to Oxygen. However, the lattice matched deposition is a very difficult goal. In reality a slight displacement from the match condition always occurs, producing the so called mismatch. The isomorphic depositions, for which the difference between the substrate and layer lattices parameters is less than 1% are rare, so that more probable pseudomorphic depositions are obtained, where an elastic layer modulation is induced, in the way to fit the substrate structure. This lattice modification introduces a strain that can be tensile or compressive. It is introduces a parameter, lattice mismatch, defined as:

$$\frac{\Delta a}{a} = \frac{(a_L - a_S)}{a_S} \qquad (1,1)$$

Where a_L is the layer lattice parameter and a_S the substrate lattice parameter. The sign of this value characterizes a compressive (if positive) of tensile (if negative) strain. While the deformation can be described through two components, the first parallel to the plane of the surface and the second perpendicular to the surface, described as follows.

$$\varepsilon_{=} = \frac{(a_{=} - a_L)}{a_L}$$

$$\varepsilon_{\perp} = -\alpha\varepsilon_{=}$$

Where a_L is the deformed lattice parameter and α is near to 1, so that the distortion is tetragonal.

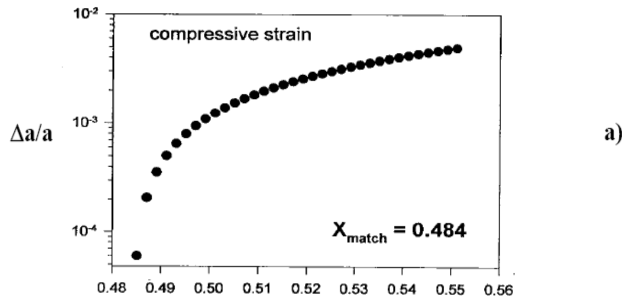

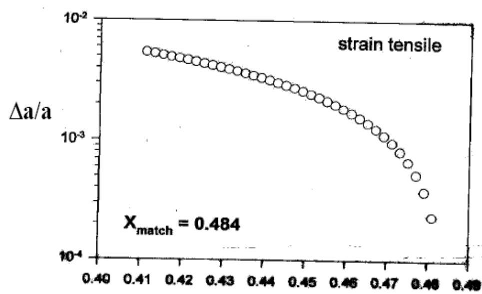

Fig.1.4: Trend of mismatch changing the InGaP composition, the case of tensile strain (a) and compressive strain (b) [1.13]

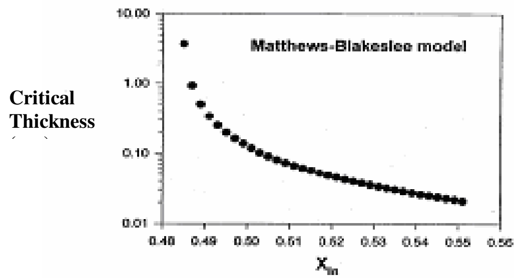

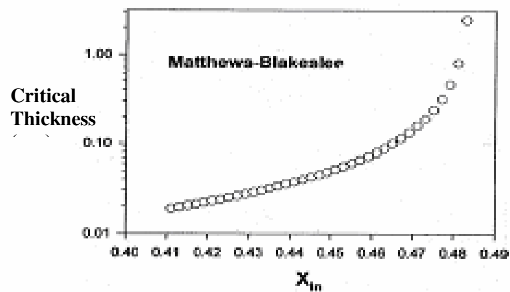

Fig.1.5: Critical thickness of an InGaP layer versus Indium moral fraction for tensile strain (a) and compressive strain (b) [1.13]

The case of InGaP/GaAs is particularly complex, as described by the graphs (Fig.1.4-1.5), in which the mismatch versus the Indium fraction in the alloy and the critical thickness (thickness above which the growing layer relaxes producing structural defects) as a function of the Indium fraction are presented.
The InGaP/GaAs heterostructure is indeed very sensitive to the stoichiometric composition: a slight variation of the composition from the lattice match causes a consistent deformation of the layer lattice (high mismatch), therefore a high parallel strain. This mismatch produces an elastic energy accumulation at the interface, which enhances as the layer thickness increases.
The lattice bears the consequent accumulation of elastic energy up to a certain value, corresponding to a critical thickness, above which all the stored energy forces the layer to a plastic relaxation, accompanied by the formation of a large amount of dislocations. The Mattews and Blakeslee model [1.13] predicts the critical thickness for InGaP on GaAs and it is connected to the Indium percentage in the alloy by the Vegard's law [1.14]:

$$a_{InGaP} = x a_{InP} + (1-x) a_{GaP} \tag{1,2}$$

Even a little displacement from the match conditions implies the formation of defects, responsible of a dramatic collapse of the electrical and optical material quality.
Therefore, it is of fundamental importance the study and optimization of the growth conditions in the way to obtain exactly the specific composition required for a lattice match.

1.4 InP/InP and InGaAs/InP

Indium Phosphide has an electronic velocity higher than Silicon but even than GaAs; for this reason it has possible applications in the high frequency range and power electronic devices. It is also characterized by a direct band gap, which encourages its use in optoelectronic devices.
It has moreover the highest carriers lifetime among Zinc-blend structures based on III-Vs.
So, like GaAs, it is possible to obtain InP from the melt, which can be utilized both like substrate for heteroepitaxial vapour phase growth of InGaAs or InGaAsP alloys and for homoepitaxial InP on InP growths.

InGaAs lattice matched with InP (In around 53%) is characterized by an Energy Gap with a correspondent wavelength, for band to band absorption or emission of light, around 1.68 μm. Therefore, it can be applied in the field of IR sensors, like IR cameras or photodetectors, but also for optical fibres communication, exploiting the wavelength between 1300 and 1550 nm. Thanks to its very low effective mass and to a high mobility, InGaAs based HEMT devices result the highest speed transistors.

The InGaAs/InP system finds moreover application in the form of Multi Quantum Wells for the production of high power Lasers [1.15].

References I

[1.1] C.Meliani, G.Post, J.Decobert, W.Mouzannar,G.Rondeau, E.Dutisseuil and R.Lefevre 180-GHz InP HEMT travelling-wave Amplifiers. IEEE Transactions on microwave theory and techniques, vol.46, N.12 (1998).

[1.2] T. Nakanishi, T. Udagawa, A. Tanaka and K. Kamei (1981) J.Cryst.Growth 55, 255.

[1.3] Takamoto T., Ohmori M; Applied Phys Lett 70, 3 , 381-383 (1997)

[1.4] C.Algora, E.Ortiz, I.Rey Stolle, V.Diaz, R.Pena, V.M.Andreev,V.P.Khovostikov and V.D.Rumyantsev, Electron Devices, IEEE Transactions, Volume 48, Issue 5, (2001) 840 - 844

[1.5] P.M. Frijlink, J.L. Nicolas and P. Suchet., J.Chrystal Growth, 107, (1991)

[1.6] M. Razeghi, M. A. Poisson, J. P. Larivain and J. P. Duchemin
Journal of electronic materials, Vol.12 n.2 (1983)

[1.7] Keith Barnham, Ian Ballard, Jenny Barnes, James Connolly, Paul Griffin, Benjamin Kluftinger, Jenny Nelson, Ernest Tsui and Alexander Zachariou, Applied Surface Science 113/114 p.722-733 (1997)

[1.8] J.D.Song Journal of Chrystal Growth, vol.270, 3-4, pp.295-300 (2004)

[1.9] Bernard Gil, “Group III Nitride Semiconductor Compounds. Physics and application” 1998

[1.10] T. Wang, P.J. Parbrook, M.A. Whitehead, W.H. Fan and A.M. Fox Journal of Crystal Growth Vol.273, 1-2, pp.48-53 (2004)

[1.11] C.Angulo Barros, Journ. Appl. Phys. Lett., 92(2002)

[1.12] Masafumi Yamaguchi, Takeshi Okuda, Stephen J. Taylor, Tatsuya Takamoto, Eiji Ikeda, and Hiroshi Kurita Appl. Phys. Lett. 70, 1566 (1997)

[1.13] Mattews J.W and Blakeslee A. E. J.Crystal Growth, 27, (118) 1974

[1.14] Razeghi M., The MOCVD Challenge Vol.2 Institute of Publishing Bristol and Philadelphia, 1995.

[1.15] T. Tanbun-Ek, H. Temkin, S. N. G. Chu, and R. A. Logan Volume 55, Issue 9, pp. 819-821

[1.16] “Semiconductors and Semimetals: Lightwave Communications Technology, Part B, Semiconductor Injection Lasers” (Hardcover) W.T.Tsang

[1.17] D.R Wight et al. (1981) J.Cryst.Growth 55, 1, 183-185

Chapter 2

An overview of the Metal-Organic Vapour Phase Epitaxy

2.1 Introduction: Comparing MOVPE and MBE

The term MOVPE (Metal-organic Vapour Phase Epitaxy) indicates a vapour phase epitaxial deposition which is based on the use of metal-organic precursors (combined in some cases with other types of precursors like hydrides, PH_3 for Phosphorus and AsH_3, for Arsenic).
More general speaking, MOVPE belongs to CVD (chemical vapour deposition) or MOCVD (metal-organic chemical vapour deposition) techniques which not imply an epitaxial growth. The MOVPE technology, developed during the 70ies of 1900, immediately revealed suitable to the growth of a wide range of III-V, II-VI, IV-VI compound semiconductors. Until nowadays, it is increasingly used in industrial and commercial production, for device applications.
MOVPE technology competes with alternative epitaxial growth technique (MBE, molecular beam epitaxy) particularly for large scale producing, in terms of cost savings, higher speed growth, deposition on large areas and adaptability in several types of materials. Over the years, high purity materials have been obtained, such as GaAs with mobilities over 100000 cm^2/Vs at low temperature and has been clearly demonstrated how this technique is very suitable for producing electronic devices with net interfaces.
The MOVPE deposition process takes place with the passage by a vapour phase to a solid one in a growth chamber in which, under opportune constant pressure and temperature conditions, several chemical reactions occur. The precursors that have been transported into the chamber undergo heterogeneous reactions in the vapour phase and homogeneous reactions with the substrate, realising for example, III and V elements that deposit on the substrate forming the III-V compound. The used pressures are usually around 10-100 mbar while the temperatures range usually from 500

to 700°C. In MBE, on the other hand, a molecular beam produced under Ultra High vacuum (UHV) conditions is exploited. This beam is supplied from holders (called "Knudsen cells") in the growth chamber, heated by Joule effect and containing elementary states sources. When the slits of the cells are opened the beam can be formed, then arriving on a heated substrate where the deposition occurs. The presence of ultra high vacuum, in the case of MBE, guarantees the growth of high purity samples with sharp interfaces and makes possible the use of in-situ (during growth) analysis techniques like RHEED (Reflection High Energy Electron Diffraction). The advantage of having a rapid source control, since the shutter can be opened and closed in terms of tenths of a second, allows a high compositional control and good interfaces, guaranteed by a lower temperature growth than in the case of MOVPE, usually around 450-550 ° C, or even lower.

On the other hand, the maintenance of an UHV system in terms of costs is one of the biggest disadvantages of this technique compared with MOVPE and the deposition is normally possible only on limited areas, only recently feasible up to 8 inches, limiting the possible use on an industrial scale. Another disadvantage of MBE is faced in the case of phosphides growth, due to the strong Phosphorous memory effect connected to the difficulty of cleaning a contaminated MBE chamber. In table 2.1, drawbacks and vantages of both the techniques are summarized.

Growth Tecnique	**Vantages**	**Disvantages**
MBE	- High purity - Defined interfaces - In situ monitoring (RHEED)	- Small areas deposition - UHV necessary - High costs - Memory effect for P species
MOVPE	- Not necessary UHV - Possibility of large scale deposition - In-situ monitoring (RAS) - C-self doping	- Toxic sources - Several growth parameters to control - C contamination

Tab 2.1: Comparison between MBE and MOVPE.

2.2 General description of a MOVPE system

A typical MOVPE system is schematized in Fig 2.1. The mechanism is based on the metal-organic precursor transport. A precursor-rich flux is obtained by letting the carrier gas, usually H_2, is

contained inside proper stainless steel cylinders (bubblers), containing the precursors (in liquid or solid form), kept under stable temperature and pressure conditions. The carrier gas is saturated with the metal-organic vapours, in the way to supply a controlled precursor quantity into the chamber. With this purpose it is fundamental to control the pressure K_{MO} and the temperature of the precursors inside the bubblers. Indeed the partial pressure of the reactors in chamber, p_{MO} depends on the thermodynamic conditions through this formula:

$$p_{MO} = \frac{\Pi_{MO}\Phi_{MO}p_{TOT}}{\Phi_{TOT}K_{MO}} \qquad (2.0)$$

Where p_{TOT} is the total pressure in the reaction chamber, Π_{MO} is the vapour pressure, Φ_{MO} is the precursor flux in the bubbler and Φ_{TOT} the total gas flux in the chamber. Only controlling the fluxes Φ is thus possible to modulate the partial pressure of the component in the chamber.
Here the basic reaction involves the reagents, which undergo pyrolysis (thermal dissociation) processes reacting together and with the substrate, to form a solid on the substrate surface. These processes can be described as follows:

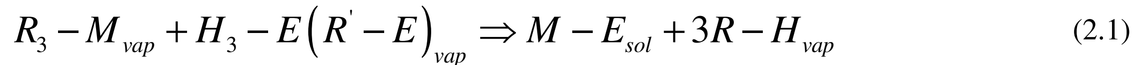

$$R_3 - M_{vap} + H_3 - E\left(R^{'} - E\right)_{vap} \Rightarrow M - E_{sol} + 3R - H_{vap} \qquad (2.1)$$

Where R and R' are generic alkyl radicals and M the group III metal, while E is a generic element of group V.
The reagents are conveyed by the carrier gas, with a flow rate between 0.1 and 1 m/s, toward the reaction chamber, where the substrate is placed and where the deposition occurs under certain temperature and pressure conditions. The growth rate is usually around 1 μm/h; as mentioned above, it is possible to deposit on a large scale, in fact the industries that currently produce devices using MOVPE deposition, use planetary reactors (such as that shown in fig.2.2) containing up to sixty substrates of 2 inches or 5 substrates up to 10'' (as in the case of the Aixtron planetary reactor) [2.1].
In order to understand the development of the growth mechanisms, it is important to consider the different involved processes: thermodynamic, kinetic and fluidodynamic. While thermodynamics is connected to the driving force of the process, kinetics determines the growth velocity, but also fluydodynamics, controlling the speed and the materials transport at the interface, influences the deposition rate.

For this reason, a detailed study must be carried out to analyse the different included macroscopic parameters.

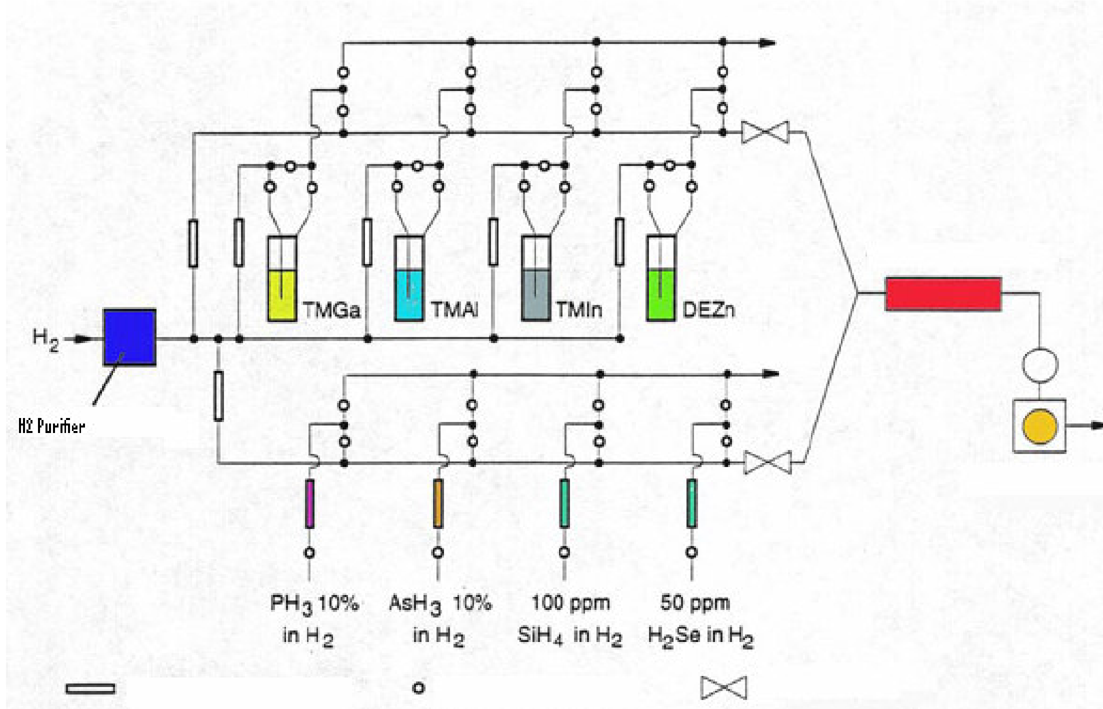

Fig.2.1: Sketch of a MOVPE system.

Fig.2.2: A Planetary reactor [2.1]

2.3 Thermodynamics aspects

The III-V semiconductors are very stable and this aspect allows a large range of choice concerning the alloys compositions, avoiding the creation of secondary phases. The only request is that the V/III ratio (ratio between the partial pressures of V and III elements in the gas phase) is higher than 1. This necessity is caused by the higher volatility of the V elements with respect to the group III

elements. This difference provokes an incongruent evaporation during growth, determining a lower incorporation of group V into the layer.

It is possible to consider the relationship between solid and vapour composition at the interface, during the deposition process, by assuming the thermodynamic equilibrium conditions. This condition is well-known and connected to the minimum of the Gibbs energy, such that:

$$G = E + PV - TS \tag{2.2}$$

Since in this case we have a 2 phases system:

$$G^{TOT} = G^{\alpha} + G^{\beta}$$

In equilibrium conditions, the total Energy must remain unchanged, so that the mole exchange between the two phases can be expressed as:

$$\left(\frac{\partial G}{\partial n}\right)^{\alpha}_{T,P,n_j} = \left(\frac{\partial G}{\partial n_i}\right)^{\beta}_{T,P,n_j} \tag{2.3}$$

The latter expression, since the derivative of the Gibbs Energy is defined as the chemical potential, can be expressed as:

$$\mu_i^{\alpha} = \mu_i^{\beta} \tag{2.4}$$

Where μ_i is:

$$\mu_i = \mu_{0i} + RT \ln\left(\frac{p_i}{p_{0i}}\right) \tag{2.5}$$

Where p_{0i} stands for an arbitrary state and p_i for the partial pressures (products between the moral fraction of the "i" product and the total pressure). In the real case, for not ideal solutions, the partial pressures ratio can be substituted by the activity:

$$\sum_i a_i A_i = M_{Crystal} + \sum_j b_j B_j \tag{2.6}$$

The reagents A_i enter in the rector submitting a pyrolysis and they react to form the layer $M_{Crystal}$ plus sub-products B_j, while a_j and b_j are stoichiometric coefficients.

The growth process, defined by an equilibrium constant K_p , can be expressed in this way, dependent on the precursors partial pressures:

$$K_P = \exp\left(-\frac{\Delta G_r}{RT}\right) = \frac{\prod_j \left(p^e_{B_j}\right)^{b_j}}{\prod_i \left(p^e_{A_i}\right)^{a_i}} \tag{2.7}$$

The expression 2.4 can thus be modified in:

$$\mu_{cryst} = \mu^e_{vap} = \sum_i a_i \mu_i^0 - \sum_j b_j \mu_j^0 - RT \ln K_P \tag{2.8}$$

The deposition on the substrate occurs under supersaturation conditions, when the reaction in equation 2.6 is completely displaced to the right. In this case, the sum of the gas species chemical potentials overcomes the crystal phase ones. So that:

$$\Delta\mu = \mu_{vap} - \mu_{sol} > 0 \tag{2.9}$$

If in the supposed reaction, A_i are the reagents leading to the formation of the B_i species, that are the products, the latter reaction becomes:

$$\Delta\mu = RT\ln\left(\frac{K_p(T)\prod_{j=1}^{n} p_{A_j}^{a_j}}{\prod_{i=1}^{m} p_{B_i}^{b_i}}\right) = RT\ln\left(\frac{\prod_{j=1}^{n}\left(\frac{p_{A_j}}{p_{Aj}^{eq}}\right)^{a_j}}{\prod_{i=1}^{m}\left(\frac{p_{B_i}}{p_{B_i}^{eq}}\right)^{b_j}}\right) > 0 \tag{2.10}$$

The supersaturation conditions are achieved with the rapid elimination of the reaction sub-products, enriching in this way the incoming flux with reagents.
The MOVPE process is endothermic, namely the deposition occurs with heating absorption. This means that to grant the crystal growth, beyond supersaturation conditions, also heating during the process must be supplied.

2.4 Kinetic and mass transport

The core of the MOVPE technology is of course the growth chamber. But it is useful to consider the processes steps that occur both outside and inside the reactor (sketched in the Fig. 2.3), from the precursors transport to the deposition. The gas mixing, composed by hydrogen and reagents, gets, after forced convection, into the growth chamber, reaching the region where the heated substrate is placed. Here, the reagents can be pyrolysed (dissociation of the metal-organic molecule stimulated by heating) already in vapour phase or after being adsorbed by the substrate surface (in the case of catalyzed pyrolysis). In the pressure range of 10^3 to 10^5 Pa, mass transport is governed by convection and diffusion. Near the substrate the convective flow is near 0 and diffusion will be dominant. Therefore diffusion is the mechanism pushing the species toward the substrate. The

adsorbed species on the solid surface start to diffuse on it until they are incorporated into the lattice sites. Instead, the species that are not adsorbed, or the reaction sub-products, are removed or desorbed and pushed away by the carrying gas flow. By convection, the carrier gas, with the sub-products, is moved away from the growth surface.

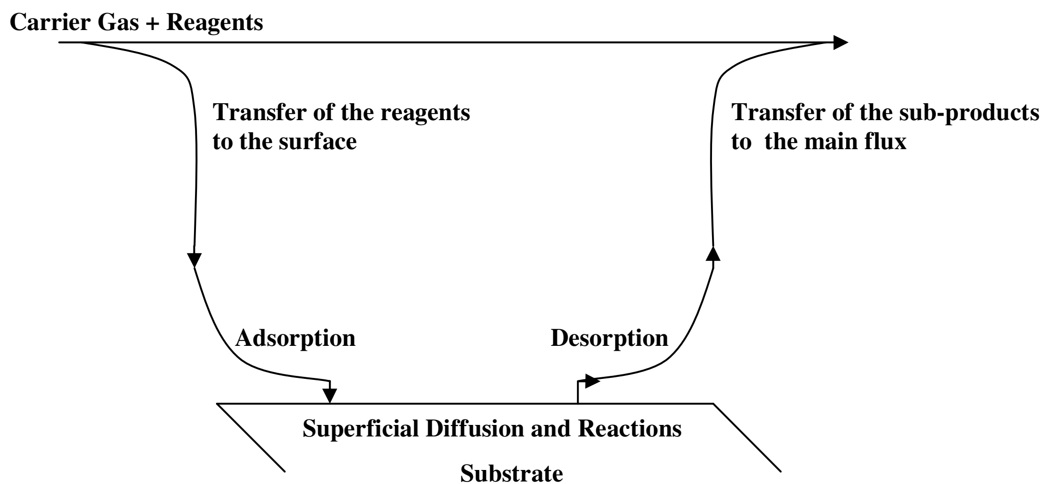

Fig.2.3: Transport and diffusion mechanism during a VPE process

2.4.1 Reaction Kinetics

The reaction kinetics depends on the type of reactions involved. The homogeneous reaction rate is in fact proportional to the first power of the species concentration, when the solid phase intervenes, the absorption must be considered.

With the purpose to study the atoms absorption phenomenon, from a quantitative point of view, the Langmuir model turns to be useful. It is based on the concept that the surface is composed by a fixed number of sites, of which the fraction θ_i is occupied. The simplified assumption is that the activation energy of the absorption is the same for each site and it is not dependent on the overlaying. A chemical bond between the adsorbed atom from the vapour phase and the surface is

established. The process occurs through two steps: the atom is at first physically absorbed, through a weak attraction with the surface, due to Van Der Waals force. The atom or the molecule, after this first step, can be desorbed, or find another superficial site, with which a new chemical bond can be formed, stronger than the physical one. In this latter case a chemical absorption takes place. The absorption rate can be expressed by the following formula [2.3]:

$$\Theta_i = \frac{k_a p_i}{(k_d + k_a p_i)} \tag{2.11}$$

when Θ_i<<1, for low surface recovers, Θ_i is a linear function with the partial pressure . The Θi value is proportional to the growth rate. So, the formula becomes:

$$r = K\Theta_i\Theta_j \tag{2.12}$$

That, in function of the partial pressures, can be expressed as:

$$r = K\frac{\beta_i\beta_j p_j^{\frac{1}{n}} p_j^{\frac{1}{m}}}{\left(1+\beta_i p_i^{\frac{1}{n}} + \beta_j p_j^{\frac{1}{m}}\right)^2} \tag{2.13}$$

Where n and m are the superficial sites, β the ratios between adsorption and desorption constants and K the constant expressed in the Arrhenius formula.

2.4.2 Homogeneous Reactions

The MOVPE process starts from a gas mixing, including the molecular components of the elements to be incorporated and the carrier gas, usually H_2. The choice of the precursors leans on the desired deposition alloy. The most common are TMGa (Trimethylgallium) for Gallium, TMIn (Trimethylindium) for Indium, AsH_3 (Arsine) for Arsenic and PH_3 (Phosphine) for Phosphorous. The last two are often opportunely replaced, because of their elevate toxicity, by the lower toxic TBP and TBAs (Terz-butyl phosphine and Terz-butyl Arsine). The metalorganic precursors, in high temperature conditions, undergo a thermal decomposition, pyrolisis, that makes available the atomic species of the elements to be deposited. During the growth process, different reactions take place. Those that occur entirely in the vapour phase are called homogeneous, those that occur on the solid surface are called, instead, heterogeneous. Both can be divided into unimolecular, in the case that only a molecule is involved, or bimolecular when the reaction is activated in the presence of two reactive species. The most important unimolecolar and homogeneous reaction, for a $M(CH_3)$ specie is naturally the pyrolysis, or rather the simple scission of an AB bond in the precursor, with the following production of methyl radicals. In the case of precursors formed by longer radical chains

(ethylic, propylic and buthylic), also the hydrogen beta-eliminations reaction, with the formation of alkenes and M-H bonds molecules, is induced (in the case of TBAs the beta elimination produces a C_4H_8 and a AsH_3 molecule) [2.4].

The pyrolysis reactions involve cationic or anionic sources:

- **Pyrolysis Reaction for a cationic source**

  Homolityc Fission

  $M(CH_3)_n = M(CH_3)_{n-1} + CH_3$

  Hydrogenolisis

  $H_2 + M(CH_3)_n = CH_4 + HM(CH_3)_{n-1}$

  Radical reactions

  $CH_3 + M(CH_3)_n = CH_4 + CH_2M(CH_3)_{n-1}$

  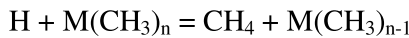

  $H + M(CH_3)_n = CH_4 + M(CH_3)_{n-1}$

  In the case that R is a buthylic, propylic, ethylic group a β-elimination reaction occurs:

  $MR_n = HMR_{n-1}$ + alkenes

- **Pyrolysis Reaction for an anionic source**

  In the case of anionic precursors, homolityc dissociations and hydrogenolysis occur and, with respect to the beta elimination, rapider and more favoured reactions occur.

  Dissociations of the X-H bond are therefore observed:

  $XH_3 = H_2 + XH$

  So as α-eliminations of a H_2 molecule:

  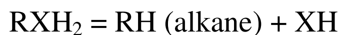

  $RXH_2 = RH$ (alkane) + XH

2.4.3 Heterogeneous Reactions

In case the reaction interests also interactions between vapour phase and surface, it is called heterogeneous reactions. The first step is the adsorption of the precursors on the surface and the possible consequent desorption. The heterogeneous reaction rate is directly proportional to the reagent partial pressure. The effect due to the surface is a weakening of the molecule bond, accompanied by the favouring of the reaction. In this way, the material growth rate is increased. Though the intermediate reactions mechanisms are not completely understood, it is possible to describe some general reactions, like:

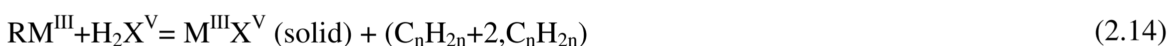

$$RM^{III} + H_2X^{V} = M^{III}X^{V} \text{ (solid)} + (C_nH_{2n}+2, C_nH_{2n}) \quad (2.14)$$

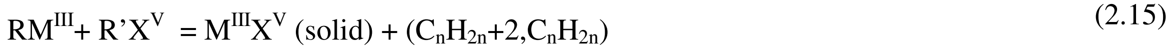

$$RM^{III} + R'X^{V} = M^{III}X^{V}\ (solid) + (C_nH_{2n}+2, C_nH_{2n}) \qquad (2.15)$$

Where M^{III} and X^{V} are, respectively, the III and V group elements, while R ed R' are the alkyl radicals [2.5].

2.5 Growth's Regimes

Two mechanisms limit the growth rate, one is the gas transport (mass transport), carrying the precursors towards the substrate, the other is determined by the interface reactions that take from the precursors the metallic elements able to form the layer. The two mechanisms have a completely different dependence on the temperature. The mass transport regime, in a pressure range between 10 and 1000 mbar, is governed by convection and diffusion. Nearby the substrate, the convection flux is practically close to 0 and the diffusion results therefore dominant; in the temperature range typically between 550 and 750°C, the diffusion is slightly temperature dependent. The situation is very different when the growth rate is limited by chemical reactions (kinetic regime). In this case, in fact, the growth rate depends exponentially on the temperature. To achieve more control on the growth rate and a better quality of the grown layer, setting in the mass transport limited regime is convenient. In almost all the III-V alloys, for example, the growth rate shows a linear dependence on the supplied III group element.

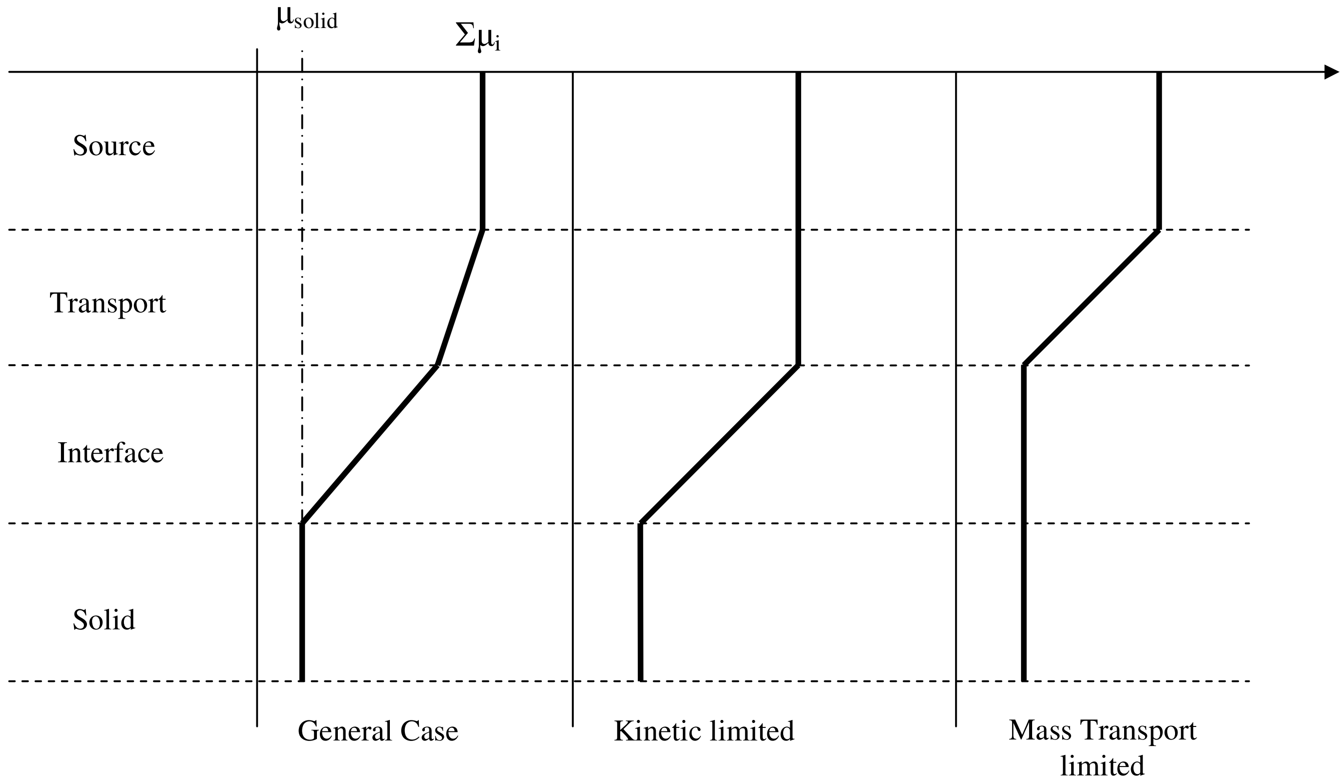

Fig.2.4: Profile of the chemical potential in different regimes.

The growth rate dependence on the temperature is connected to the graph of fig.2.4, in which the chemical potential profile in the different regimes is described. In the general case, the chemical potential is limited by both the transport and interfacial reactions. In the case of a kinetic regime, the chemical potential drops only at the interface, because the transport is very fast. On the contrary, when the process is mass transport limited, it influences the chemical potential. This situation occurs when the growth temperature is low and the precursor fluxes high, therefore, as described in the graph of fig.2.5 (part 1) the growth rate increases exponentially with the temperature increasing. As the temperature are higher (between 450 and 750°C) the rate keeps substantially independent of the temperature (mass transport, part 2), while a decreasing of the growth rate is observable at further lower temperatures (part 3), where the desorption from the surface starts to influence the process growth [2.6].

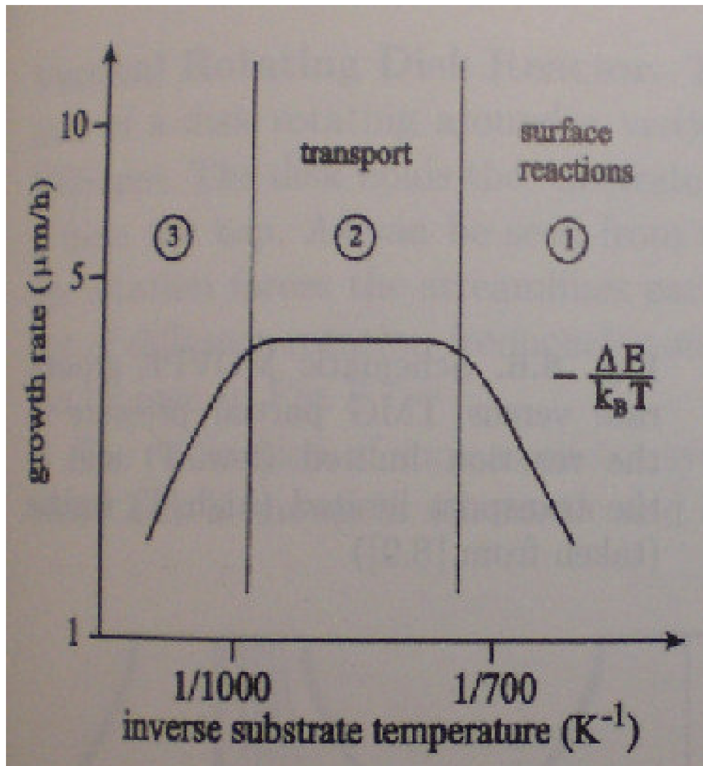

Fig.2.5: Example of GaAs growth rate: 1) kinetic regime 2) transport regime 3) high temperatures

2.6 Fluidodynamics aspects

The most common geometry used in the MOVPE technology is that of a horizontal reactor, formed by Quartz walls, cooled by the flux of the same carrier gas. The chosen geometry is very important for the aim to obtain a lateral homogeneous growth, exploiting a gas flux as laminar as possible. The horizontal chamber, with rectangular and constant section, appears to be the more ideal for this goal. The fluidodynamic aspects are highly influenced by the reactor configuration. The consideration of fluidodynamic aspects requires the solution of complex equations, the three dimensions continuity equations for mass, momentum and energy. The continuity equation for each species can be expressed as follows:

$$\frac{\partial \rho_i}{\partial t} = -\nabla\left(\rho_i \vec{v} + \vec{j}_i\right) \tag{2.16}$$

Where j_i is the diffusive flux with respect to the average velocity of the i species and ρ_i is the mass density of the i species and t is the time.

The Navier-Stokes formula describes instead the momentum conservation in a multi component system.

$$\frac{\partial \rho \vec{v}}{\partial t} = -\left[\nabla\left(\rho \vec{v}\vec{v} + \vec{\Pi}\right)\right] + \sum_i \rho_i \vec{g} \tag{2.17}$$

Where ρ is the total density, $\vec{v}\vec{v}$ the dyadic product (second order tensor in which the matrix elements are the products of the components of the two vectors), Π is the forces tensor (derived from the sum between pressures tensor and attrite forces) and g_i is the sum of external forces per mass unity on an i component.

From the first thermodynamic law the energy conversion law derives:

$$\frac{\partial \rho\left(E + \frac{v^2}{2}\right)}{\partial t} = -\nabla\left\{\rho\left(E + \frac{v^2}{2}\right)\vec{v} + \vec{q} + \left[\vec{\Pi}\cdot\vec{v}\right]\right\} + \sum_i \left(\vec{n}_i \cdot \vec{g}_i\right) \tag{2.18}$$

where E is the internal energy per mass unity, q is the heat flux and n_i the total mass of component i. The three equations above citied need, for their solution, the border conditions employed into the model of the boundary layer.

In these conditions, the gas velocity at the height of the substrate and of the walls reactor is 0 because of the viscose friction forces. As a consequence, the parallel component of the flux vector is progressively damped, approaching the interface with the surface. While leaving the surface it increases up to the main flux velocity and nearby the walls each flux component is 0, assuming therefore that deposition occurs above the walls. The layer, in which the gas flows with a speed lower than 1% than that of the main flux, is called boundary layer, or limit layer. In this situation, the fluidodynamic equations can be solved, for a $z>\delta_0$, giving:

$$\delta(x) \cong 5\left(\frac{v_x(x,y)x}{v_0}\right)^{\frac{1}{2}} \tag{2.18}$$

Where v_o is the not perturbed gas flow velocity, while v_x is the flux velocity at the x distance from the substrate.

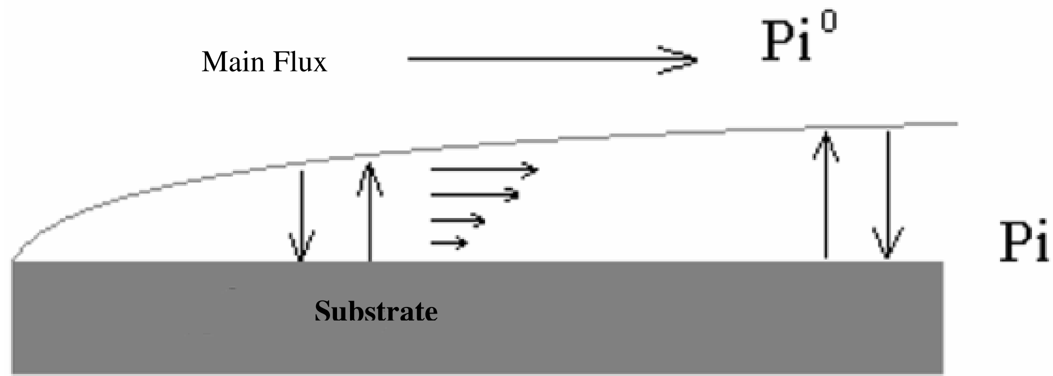

Fig.2.6: boundary layer model

Through the boundary layer, the diffusion from the precursors flux to the substrate occurs, so its properties, like the degree of homogeneity, influences the quality of the deposited layer. Therefore it is necessary to reduce the boundary layer thickness, in the way to optimize the reagents diffusion.

2.7 Reactor pressure conditions

With the purpose to reduce the boundary layer, the choice of low working pressures, in the range of 10-100 mbar, is really important. A growth realized at low pressures is also favourable because it can reduce the pre-reactions effect in the gas phase (the partial pressures of the different gases are indeed very low). In the particular case which the precursors of the III group are used, it was clarified that low pressures are important to avoid parasitic reactions. There are many examples that can prove this conception, in systems like InGaAs or InP.

Moreover, low pressure reactors are required for large scale depositions, where the large dimensions would make unavoidable, at atmospheric pressure, the presence of turbulences and unintentional reactions. On the other hand, at low pressures the growth selectivity is increased, so that, if dielectric masks are used, the deposition occurs only on uncovered areas. Other favourable aspects are the lowering of the species diffusion coefficients, less uncontrolled doping and, in general, the reduction of the undesired species incorporation (also thanks to the possibility to realize the deposition at lower temperatures). Moreover, at low growth pressures, sharper interfaces are observed. Also, a reduction of the memory's effect and a better compositional homogeneity and thickness control have to be considered. But the use of low pressures reduces the pyrolysis rate, forcing to use higher V/III ratios and, in addition, the interactions between groups V and III precursors are reduced.

2.8 Metal-organic precursors

As already in part described, before entering the reaction chamber, the carrier gas must be enriched with the metalorganic vapours, after its passage in the bubblers (sketched in figure 2.7).

.

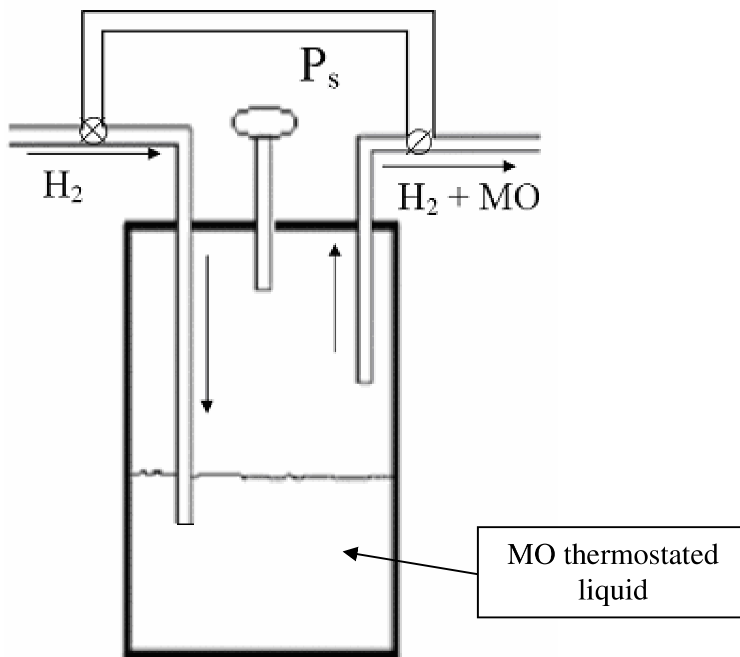

Fig.2.7: Sketch of the bubbler

The metalorganics contain metal-alchilic group bonds and are featured by relatively high vapour pressures, around 100 torr at the working temperatures. The metal-organic sources are highly reactive with Oxygen and water, the more utilized are the thrimethyls, because of their high stability [2.7].

Depending on the group of the metallic element, different chemical properties are present. The group II precursors are MR_2 kind molecules, as Dimethylzinc or Dimethylcadmium. The group II element has 2 electrons in the s type orbital, in the external shell: to provide two covalent bonds, an sp hybridization occurs, that forms two sp linear orbitals. The so built molecules are electron acceptors, or Lewis acids, thanks to the not completed p orbitals. In the case of the group III precursors, a sp_2 type hybridization takes place (example in Fig.2.8), with the formation of a trigonal planar molecule, characterized by 3 ligands, separated by 120°. Thus after the formation of 3 covalent bonds, the p orbital, perpendicular to the molecule plane, remains unoccupied, making

the molecule electrophile, a Lewis acid also in this case. Differently in case of group V metalorganics, where 3 p and 2s electrons are present, the formation of 3 covalent bonds and a sp_3, hybridization occurs with tetragonal configuration. They form bond angles around 109,5° with 2 unbound electrons at disposal. The present electron pair makes the molecule a Lewis basis or electron donor.

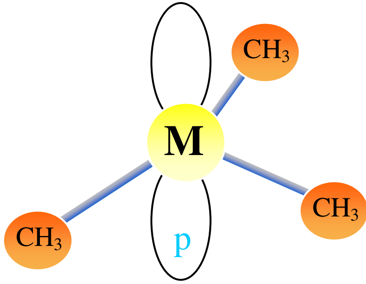

Fig.2.8: M-$(CH_3)_3$ structure (TMIn and TMGa).

The VI group precursors have two s and 4 p electrons. Two covalent bonds occupy two of the tetrahedral sp^3 positions.

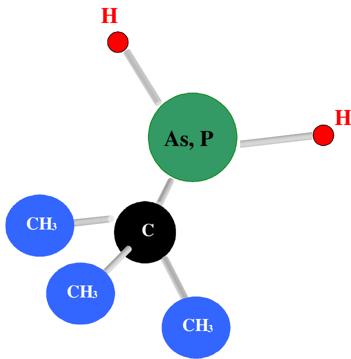

Fig.2.9: $MH_2C(CH_3)_3$ structure (TBA and TBP)

In general, the metalorganic precursors must have specific properties in the way to be particularly suitable for the growth: a low pyrolysis temperature, the absence of pre-reactions in the gas phase, a high purity (electronic grade) and low toxicity. TBAs (tertiarybutylarsine) and TBP (tertiarybutylphosphine), satisfy quite well these features, mainly the low toxicity and the reduced dissociation temperature [2.8]. Their composition is illustrated in fig.2.9. They present very suitable features for the MOVPE process. First, they are characterized by proper vapour pressures: TBP shows a high vapour pressure, 286 torr at room temperature, while the TBAs is of 96 torr at 10°C. With respect to the more traditional Arsine and Phosphine, one of the Metal-hydrogen bonds is replaced by a metal-carbon bond, sensibly reducing the toxicity. Indeed the limit threshold values

(TLV, toxic index defined as the maximum acceptable concentration in a 8 hours/daily use), for AsH_3 and PH_3 are respectively 0.05 and 0.03 ppm, while the LC50 (lethal concentration for 50% of the rats population tested) is between 11 and 50 ppm for AsH_3, 77 for TBAs and 1100 ppm for TBP.
Moreover while AsH_3 undergoes a 50% pyrolysis at a temperature around 600°C, and PH_3 shows pyrolysis temperatures even higher (over 850°C), TBA has a pyrolysis of 50% at 425°C (450°C for TBP). These characteristics grant a lower materials consumption and lower V/III ratios, whose typical values are between 1 and 100, to be compared with the 1000 of the hydrides.

The use of these alternative precursors evidenced the experimental reduction of the unintentional Carbon incorporations, and with this, of the background doping [2.9]. This effect, widely documented in the case of TBAs, is naturally consequence of the lower pyrolysis temperatures. This dissociation mechanism causes intra-molecular reactions that end to produce H_2 species in higher quantities than in the case of hydrides. H_2 plays a role in removing radical species from the surfaces. The hydrogen atmosphere that the ethylic and tetiarybuthilic species tend to form products such as C_2H_4 and C_4H_8, much more stable than CH_2, and much less responsible of Carbon incorporation into the grown layer. Another important vantage is that by lowering the reagents a lower usury of the vacuum system and of the drainage gas synthesis follow.
For the growth of doped layers, in the case of III-V InGaAsP-type semiconductors, Zinc for p doping and Silicon for n doping are used. The most common zinc precursors is Dimethilzinc, DMZn, that undergoes the 50% of the pyrolysis at a temperature of only 250°C. Silicon in general is supplied by a gas source, Disilane.

2.9 MOVPE system at The Parma University

It is certainly opportune to describe the MOVPE system that we used in this PhD work and its peculiarities. The MOVPE reactor operating at the SEMLABS group of the Parma University is an AIX200, working at low pressures, up to 1 mbar, and constituted by the following elements:

- a rotating sample holder sited on a graphite susceptor (gas foil rotation)
- a quartz reactor chamber
- the metalorganic sources, contained in stainless steel cylinders, dipped in thermostated baths

- the gas lines and the mass flow controllers that constitute the transport/dilution system for the precursors
- The heating system, based on IR lamps, able to heat the graphite holder up to 850°C.
- The vacuum system, equipped with a rotary pump and a throttle valve for the pressure in the growth chamber
- A panel for the management of electro-pneumatic valves, of the mass flow controllers and of the reactor pressure
- A glove box with ultra-pure nitrogen for substrate loading
- A pc interfaced with the machine for the growth processes management
- A sophisticated alarm system and monitoring of harmful gasses and hydrogen
- A system for the chemical abatement of harmful gasses, called scrubber

Fig.2.10: MOVPE system at the University of Parma.

The available precursors are: DMZn (Dimethylzinc) for Zinc, p-doping in III-V semiconductors, TMIn (Trimethyl-Indium), TMGa (Trimethyl-Gallium), TBP (Tertiary-buthilphosphine) and TBAs (Tertiary-buthyl-Arsine). Moreover, a gas source for n-doping, Disilane diluted at 200 ppm in pure hydrogen.

With the aim to obtain a high purity level, indispensable for microelectronic application, the used gasses are ultra-pure and the pipes electro-polished. The working gasses are nitrogen and hydrogen. During the growth processes, Hydrogen is used because it favours the precursor pyrolysis and can be highly purified (the hydrogen flux undergoes a further purification through a filter based on a Palladium cell, operating at 400°C, reducing the impurity concentrations below 0.1 ppm), Nitrogen is used in service/standby conditions, for security reasons.

The growth chamber is a reactor, a cylinder shape pipe with a rectangular section, made of pyrolitic quartz. The susceptor, on which the rotating sample holder is placed, is made of graphite. The sample holder rotation is induced by a hydrogen flow operating on the bottom side of the susceptor. The susceptor is heated by 5 couples of IR lamps placed beneath, and the temperature is measured by a thermocouple sited inside the susceptor. The rectangular section chamber is contained in an external cylinder. In the gap between the external cylinder and the chamber a flux of H_2 flows. It allows cooling the walls of the internal chamber.

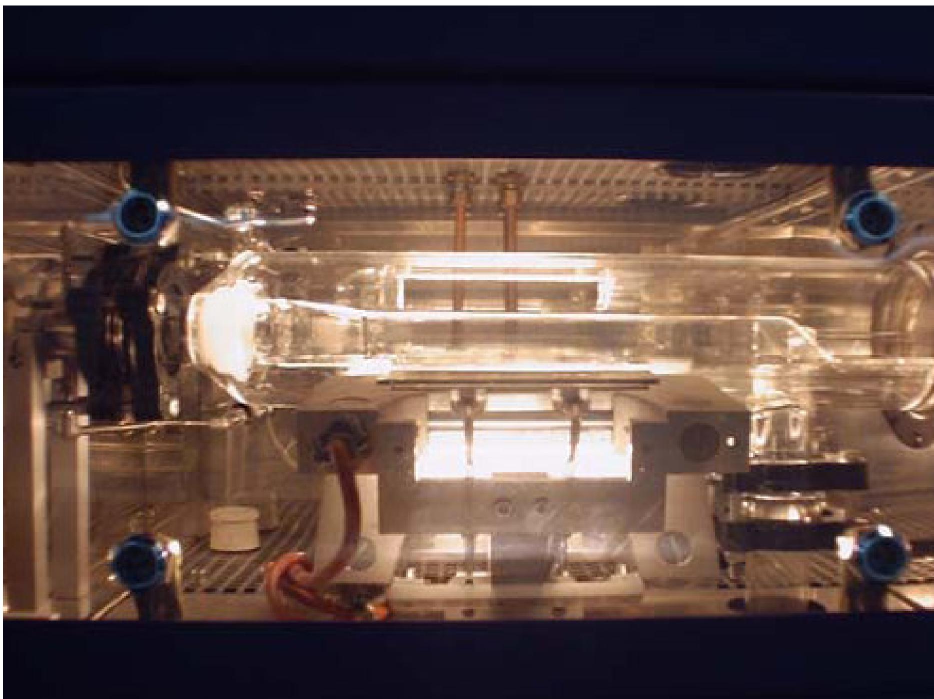

Fig.2.11: The Reactor at the SEMLABS

A PID system, proportional-integral-differential, permits to control the set substrate temperature within a tenth of degree sensitivity. The hydrogen fluxes control, important for reagents carrying, occurs through mass flow controllers, MFC, with a precision of 1% with respect to the full scale value. The bubblers temperature is controlled by thermostat baths, within a 0.1°C error that, influencing itself the regulation, brings the sensitivity of entering fluxes to be however lower than 2%.

References II

[2.1] http://www.aixtron.com/

[2.2] G.B.Stringfellow, Organometallic Vapour-Phase Epitaxy: Theory and Practice, Accademic press

[2.3] T.Ksharma et.al. Journal of Crystal Growth 221, (2000) p 509

[2.4] "Organometallic Vapour Phase Epitaxy" Gerald B.Stringfellow

[2.5] "Epitaxy" M.A.Herman,W.Richter, H.Sitter

[2.6] "Optical Characterization of Epitaxial Semiconductor Layers" G. Bauer, W.Richter

[2.7] Mattews J.W and A.E.Blakeslee, J.Chryst.Growth, 27, (118) 1974

[2.8] Stoltz W., Compound Semiconductors, 5, p.29 (1999)

[2.9] H. Tanaka, T. Kikkawa, K. Kasai and J. Komeno: Jpn. J. Appl. Phys. 28 (1989) L901

[2.10] E. Vanelle, N. Grandjean C. D Jpn.Jour.Appl.Phys.37, (1998), p15

Chapter 3

Diagnostic Techniques

In this chapter the experimental techniques, used for investigation of the structural, electrical and optical properties of the epitaxial layers studied in this PhD project, will be briefly resumed. The different diagnostic techniques can be classified in this way:

A) Structural analysis of as-grown layers: HRXRD High Resolution X-ray Diffraction, for the determination of thickness, composition and lattice mismatch. In some cases (TUB activity), an in-situ technique (RAS: Reflectance Analysis Spectroscopy) has been applied in order to monitoring the MOVPE-growth (surface morphology, composition, doping and thickness) during the growth process.

B) Structural analysis of implanted layers :(RBS Rutherford Backscattering Spectroscopy, PIXE Proton induced X-ray Emission, SIMS Secondary ions Mass Spectroscopy) for the investigation of the lattice damage and thermal annealing recovering effects, depth profile of the implanted impurity, efficiency of the activation process of the implanted species.

C) Electrical analysis : (I-V, Hall Effect, C/V and DLTS) for the measure of conductivity and mobility, carriers concentration, compensation ratio, localization energies of the electrically active defects in the band gap and electrical compensation efficiency in the case of implanted layers.

D) Optical analysis: (PL photoluminescence): study of the optically active defects in the band gap.

3.1 Structural Analysis

3.1.1 RAS (Reflectance Anisotropy Spectroscopy)

Since the last years, one of the main disadvantages of MOVPE, in respect to others advanced epitaxial techniques, caused by the lacking of a real time monitoring of the growth process, has

been removed through the application of optical techniques which do not require an high vacuum environment (as for RHEED analysis in a MBE apparatus).
In case of RHEED, the diffracted electrons analysis leads to the determination of the atomic periodicity structure and, through this, the valuation of the composition of the growing layer. Observing the signal oscillations (connected to the Frank-van Merve type growth) the layer thickness can be also obtained. RHEED cannot be used at the moderately low pressure value (10-50 mbar) which characterizes the MOVPE growth process, because the electrons beam would be strongly damped by the too high pressure. On the contrary, the optical techniques (spectroscopic ellipsometry, RDS reflection difference spectroscopy or RAS) have been successfully applied for in situ monitoring of MOVPE growth processes.
The first RAS-type systems were built by Cardona in 1966 [3.1] and latterly improved by Aspnes and his group [3.2]. They applied the reflectance anisotropy analysis for the surface study, performed at the beginning on RDS (reflectance difference spectroscopy). The RAS measurement is substantially an ellipsometric measure technique, a linear optical measure, performed at a normal incidence angle (while the spectroscopic ellipsometry exploits an incidence angle around 45°).
RAS measures the spectral dependence of the light polarization changing of a linearly polarized light after being reflected from a surface. A time resolution, of 50 ms, leads to control of single monolayer growth with a high sensitivity to the atomic bonds rearrangements during the surface reconstruction.
A typical RAS system is described in the following scheme (fig.3.1). A Xenon lamp at a permitted energy range, between 1.5 and 6 eV, provides light that is immediately focused through MgF_2 or quartz based optical focus. Then it is linearly polarized along the [110] and [-110] directions, parallel directions to the growing surface and driven toward the sample. When any anisotropy is present, like in the case of a bulk material with a cubic structures, r [110]= r [110], no RAS signal should be generated, but this does not occur at the surface, where the bonds are in construction and the structure is not yet formed. The reflected light shows a change in the amplitude and phase, therefore a contribution to the anisotropy in the detected signal occurs. In this way the RAS signal is given by: the relation reported in the frame of Fig. 3.1 illustrating a typical RAS set-up.

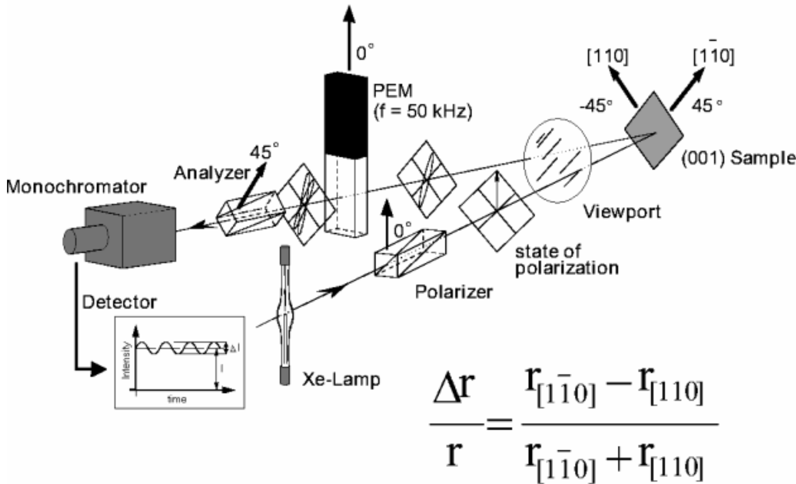

Fig.3.1: A typical RAS set-up

The RAS signal is practically the real part of reflectance anisotropy along the main surface axis divided by the total reflectance, provided from the direct current signal measured on the detector. It will be dependent by the atomic structure reconstruction of the growing layer. A PEM (Photoelastic Modulator) and an analyzer, set at 45° respect the mean PEM axe polarization, analyze the polarization state of the reflected light beam. The PEM is formed by a crystalline quartz part glued to a glass. Applying an alternate voltage (of 50 Hz) to the crystal, vibrations in the applied electric field direction are induced from the piezoelectric effect. They produce a strain on glass quartz, which makes it birifrangent. As a consequence a phase difference between perpendicular and parallel polarized light occurs. Therefore, the lock in amplifier (phase sensitive detector) is able to distinguish between two different perpendicular light contributions, transforming the polarization difference in intensity modulation, and finally extracting the RAS signal.
The RAS cannot be applied to any surface crystal structure. It is necessary that the two mean axes are perpendicular to the crystal surface. The most common case is the 001 surface of a fcc lattice, where the RAS sensitive direction are [110] and [1-10]. On the contrary, the [111] and [-1-1-1] oriented surface gives a null signal because the main axes forms an angle equal to 60° and the anisotropy at 90° is cancelled [3.3]

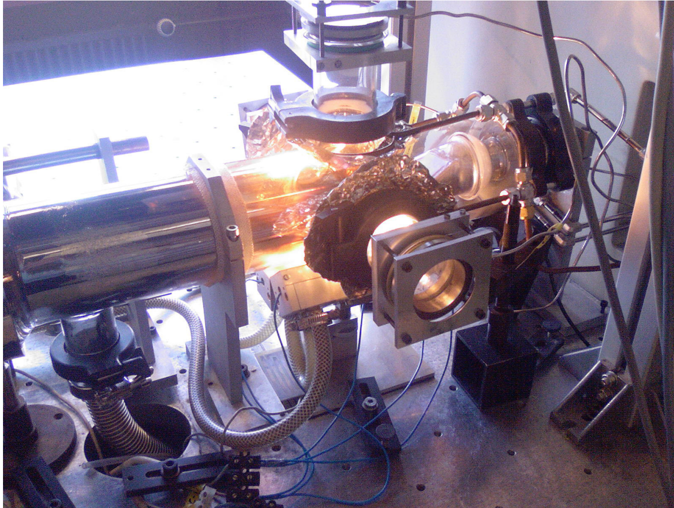

Fig.3.2: RAS system at AG Kneissl, TUBerlin

To understand the potentiality of this technique, we could observe, for example, the information obtainable applying the RAS analysis to GaAs 001 (fig.3.3).
An epitaxially growing Gallium Arsenide shows a surface reconstruction respectively as: (i) α or β2 (2X4), (ii) c (4X4), (iii) (2X6), which are illustrated in Fig. 3.3 with the related RAS spectra. The different reconstructions depend from the growth conditions and from the stoichiometry ratio. Under arsine the c(4X4) reconstruction is favoured. Stopping the Arsenic supply, at higher temperatures, arsenic desorption is caused with the consequent formation of a (2X4) surface reconstruction. If the growth rate is raised, at moderate temperatures, a mixture between c(4X4) and (2X6) occurs, evidencing the presence of Ga dimers at the surface (since the 2X6 is a Ga-rich reconstruction). Considering more carefully the spectra shapes c(4X4) and (2X4) one can realizes that the GaAs(001)-(2X4) surface has a typical camel shoulder shape, while the GaAs (001)-4X4 is characterized by a minimum at 2,6 eV. These peaks are due to the electronic transitions between bands occupied by a As dimers pair to unoccupied bands. The different spectra are associated with different atomic surface distribution. In fact, in the two different reconstructions the As pairs take a different direction in respect to the [110] and the [-110] axes, therefore they give different sign contributions to the RAS signal, which produces fully different RAS spectra.

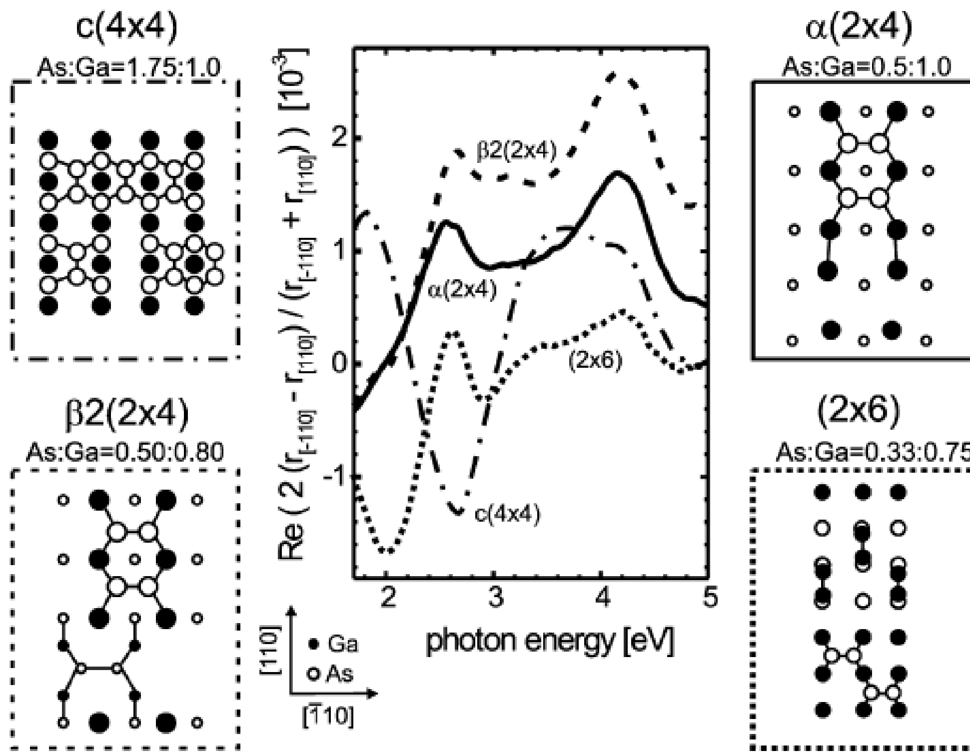

Fig.3.3: Different GaAs reconstructions and related spectra [3.4]

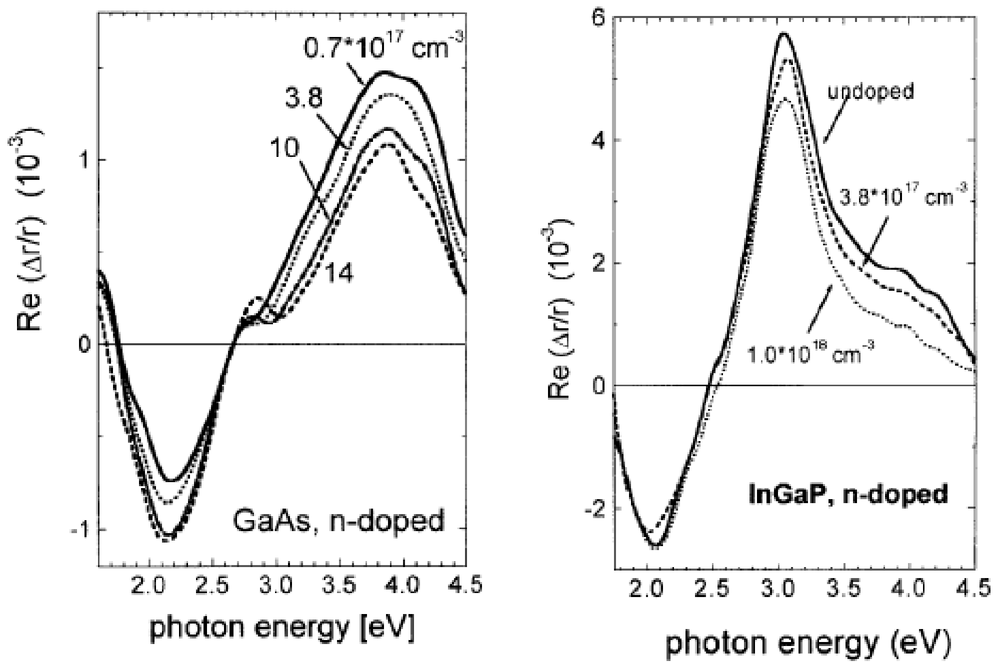

Fig.3.4: RAS response to high n-doping levels (a)GaAs and (b)InGaP [3.4]

The sensitivity of the RAS spectra for different doping concentrations offers a further performance of this system. In fact, in this case, an electric field (see fig.3.4) within the surface and the depletion layer arises. The dependence of the RAS response with the doping has been studied for GaAs and InP bulk materials. It has been shown that it influences the RAS spectrum shape at around 3 eV and this feature was attributed to LEO (linear electro-optic) effect.
The type of doping can be also determined, since n or p carriers originate different RAS signs. For example, the spectrum obtained on n-type doped GaAs, as it is shown in the picture (fig.3.5) has a shape apparently indicating it to be less As-rich, since the group-III dangling bonds are empty and the group V dangling bonds occupied by electrons and higher numbers of new III dimers are expected to be formed.

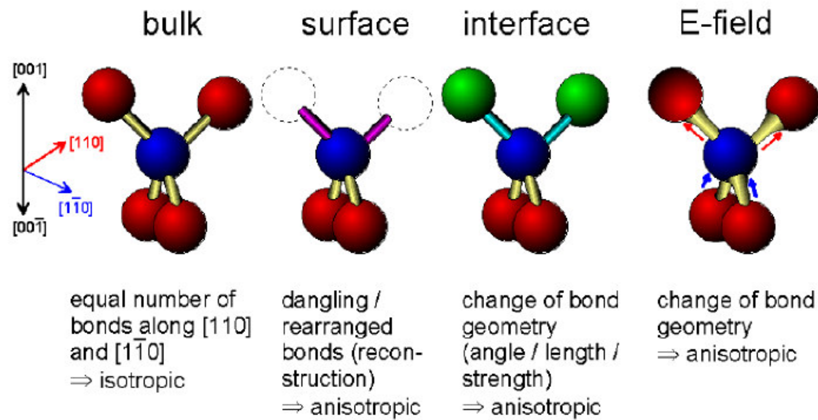

Fig.3.5: Contributions to the RAS signal

3.1.2 HRXRD (High resolution X ray Diffraction)

When a light radiation interacts with a structure of elements outdistanced by a length comparable to its wavelength, interference phenomena are induced. This is the case between X rays and an atomic lattice and it is the base of the diffraction analysis.
In a single crystal the X radiation submits different scattering events, impacting with the crystal and penetrating into its bulk. Coming out the ray produces an interference, figure 3.6. It is the so called Bragg diffraction, consequence of interference between waves reflecting from different crystal planes. The condition of constructive interference is given by Bragg's law:

$$m\lambda = 2d\sin\theta_B \tag{3.1}$$

where: λ is the wavelength of the incident radiation, d is the distance between crystal planes,

θ_B is the angle of the diffracted wave and m is an integer number, the order of the diffracted beam. Known the crystal symmetry, the Miller indexes for each planes order and their distances are also known, therefore comparing the wave vector of the incident and the diffuse light, information on the lattice parameter and the sample thickness can be obtained. Then, since the Vegaard law connects the lattice parameters to the composition, the alloy composition (in a ternary compose for example) can be derived.

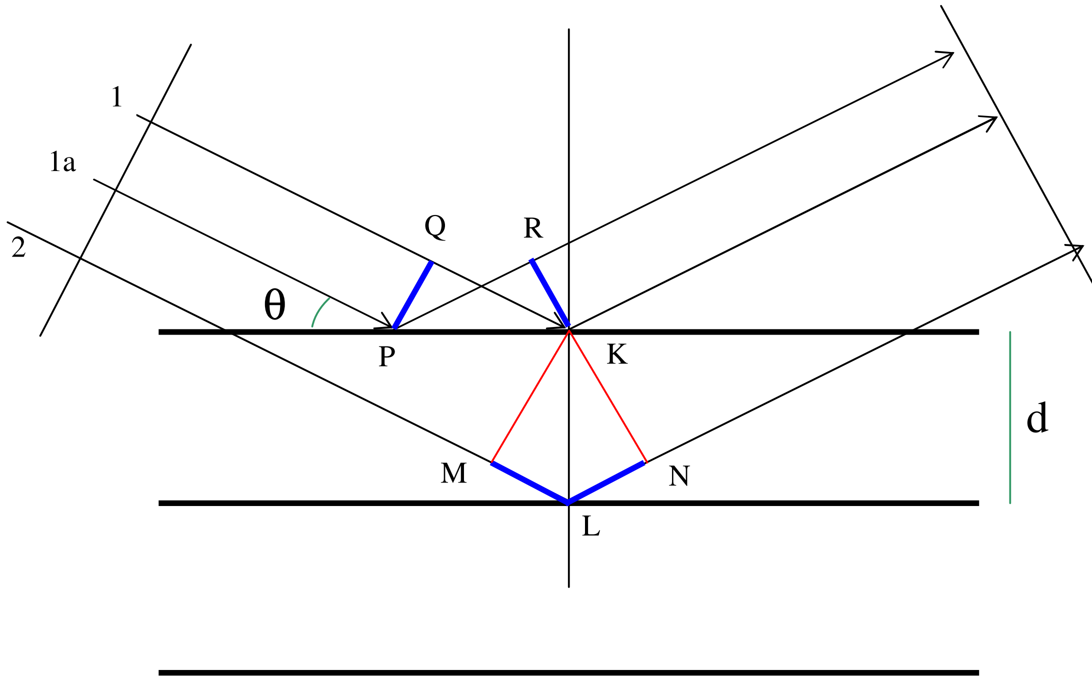

Fig.3.6: Bragg diffraction between planes in a crystal

In a heterostructure, when the grown layer has a different lattice parameter than the substrate, a mismatch occurs and in a diffraction spectrum, an angular separation between the two relative peaks can be observed. This separation is dependent to the perpendicular mismatch to the surface in this way:

$$\left(\frac{\Delta a}{a}\right)_{\perp} = -\cot\theta_B \Delta\theta \qquad (3.2)$$

And the angular distance between each epitaxial layer permits to obtain the grown layer thickness considering the following formula:

$$d = \frac{\lambda}{2\Delta\theta\cos\theta_B} \qquad (3.3)$$

That is possible to use only when the lattice mismatch is different from zero.
It is possible to examine the diffraction spectra through calculation software based on dynamic diffraction theory. Performing a fit with the experimental diffraction curve, especially a valuation of the composition and the thickness is possible.
The instrument used in this study is a high resolution x ray diffractometer with a Cu source at 2200 W, from which a spectral line K_{Al} is selected through a double crystal Ge monocromator.
A four-circles goniometer with an angular scansion (fig.3.7) of 0.5 seconds is used and it is possible to detect minimum mismatch variations around $5X10^{-6}$. The spectra are obtained at 004 diffraction conditions.

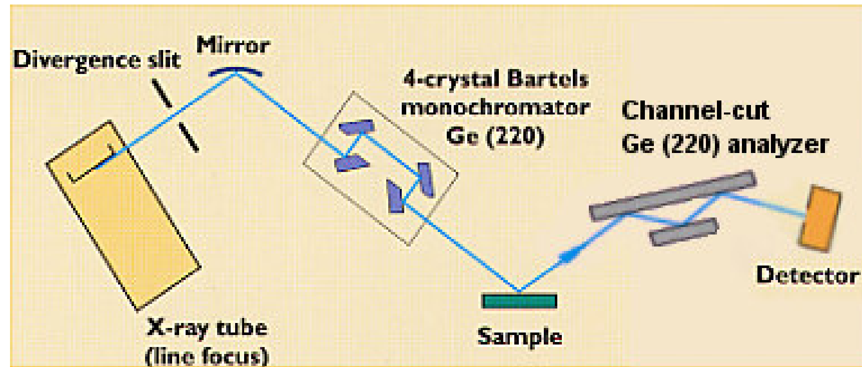

Fig.3.7: Four-crystals monochromator system HRXR configuration

3.1.3 RBS (Rutherford Backscattering Spectroscopy)

RBS, together with PIXE, permits to investigate the structure of the implanted samples, estimating the damage produced and the recovering after a subsequent thermal annealing; in addition, it lets to detect the concentration and the fraction of lattice sites occupied by the introduced impurities [3.5]. RBS uses a beam of light ions, as He, which, accelerated toward a sample, impacts the investigated material. By colliding elastically with the atomic species contiguous the surface, the exciting ion beam diffuses in all the directions. Only the backscattered particles (that after the collision invert their motion) are detected. The count of He ions backscattered is detected and measured in dependence of a magnitude, defined as channel number, connected to the residual energy of the scattered ions. This residual energy is part of the particle kinetic energy before impact and it is associated to the atoms properties, constituting the matrix against which it collides, particularly mass and depth. To localize the impurity position it is necessary to operate in channelling conditions, when the beam is parallel oriented to the crystal directions, so that it meets a minor particles number in comparison to a random orientation. In these conditions it submits a lower number of collisions. The channelled ions consequently reach higher penetration depths and a lower

number of backscattered ions are detected. Since they meet impurities placed into the channel, anyway, the scattering has more probability to occur and the RBS signal assumes a higher intensity. Naturally, this is the case of a sample after implantation, where host atoms are introduced. They can also place in interstitial positions, into the channels, or they could displace the matrix atoms, distorting the crystal and moving them in the way to obstacle the channels. Therefore the channelling results a very useful technique to estimate the crystal damage of the material after implantation, since the presence of clusters and amorphous regions tend to enhance the so-called de-channeling (deflecting the particles out from the channel toward the lattice atoms), consequently increasing the RBS signal. In the case of a zinc blend crystal, the main axis, <100> <110> <111> are the crystal channels.

3.1.4 PIXE (Proton Induced X Ray Emission)

The PIXE (Proton Induced X-Ray Emission) technique is quite similar to RBS. So that often, like in the cases mentioned in this PhD activity, they can be performed simultaneously, using different detectors. Again, a Helium protons beam is used and the sample is positioned in the same chamber, at a 10^{-6}mbar pressure, but this time the analysis is on the X-ray emissions. The X ray detector, a Si (Li), must be places at a 135° angle from the beam direction.

The proton beam, in fact, induces an excitation on internal shells electrons (K for the light and K and L for weight atoms) to external shells. Coming back to their original positions, the electrons cause X radiation emissions dependent on the hit atom. A spectrum PIXE can be therefore derived. It consists in peaks connected to X transitions, coming out from the sample. The signal is superimposed with the background, caused by γ rays, emitted after interaction between the beam particles and the matrix nucleuses, and with the Bremsstrahlumg processes. In the way to minimize this background signal, filters of Cu or Al with 75 microns thickness are used.

As already mentioned, with the aim to localize the impurity in the lattice, the comparison between PIXE and RBS is necessary. It is impossible in fact to compare the PIXE impurity intensity with the matrix, because the matrix contribute comes from the entire depth, while the impurity one takes origin only at the selected implanted area. Therefore, the PIXE signal, coming from the impurity, must be compared with the RBS signal coming from the matrix, in a detailed referring region and in channelling conditions (Fig. 3.8).

.

Comparing RBS signal and PIXE in channelling conditions it is possible to detect the implanted atoms positions in the lattice. In particular this procedure permits to quantify the fraction of impurities atoms localized in substitutional (therefore electrically active) or interstitial positions.

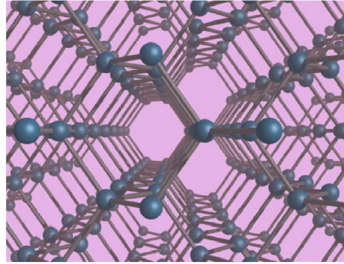

Fig.3.8: channels in a zinc-blend crystal

3.1.5 SIMS (secondary ion mass spectroscopy)

The SIMS technique is really useful in many fields of material science because it allows an analysis of the elements contained in a sample, permitting the detection of elements up to a concentration of around 1 ppb [3.6].
In a SIMS measurement a primary ions beam, accelerated at energies around keV, bombards the sample. In consequence of the ions impact a secondary ions quantity is pulled up from the surface (Fig.3.9). Only a little percentage of them, about 1%, is ionized and driven toward a mass spectrometer. The particles are therefore detected, giving an imprint of the chemical elements present in the sample and their concentrations. Calibrating the depth with the erosion time is then possible to perform a profile of the elements concentrations, consenting to detect the distribution of each element along the depth of the epitaxial layers.
Thus, in order to obtain the higher possible quantity of secondary ions, the sputtering of a primary beam, constituted by a suitable ion specie, is suggested. In this way, this latter is able to create many ionic species. In particular, Oxygen and Cesius are generally used.
The secondary ions formed are directed and accelerated toward the mass analyzer by a bias voltage (more than 4500 V). Here, knowing the mass/charge ratio of every element, the nature of the species can be recognized. The detection is based on the use of a mass magnetic analyzer or a quadrupole that permits to detect each different element, selecting in base of its deflection caused by its own mass/charge ratio.

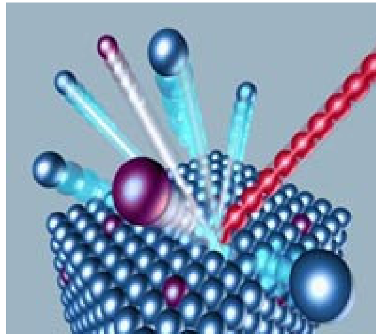

Fig. 3.9: Secondary ions production [3.7]

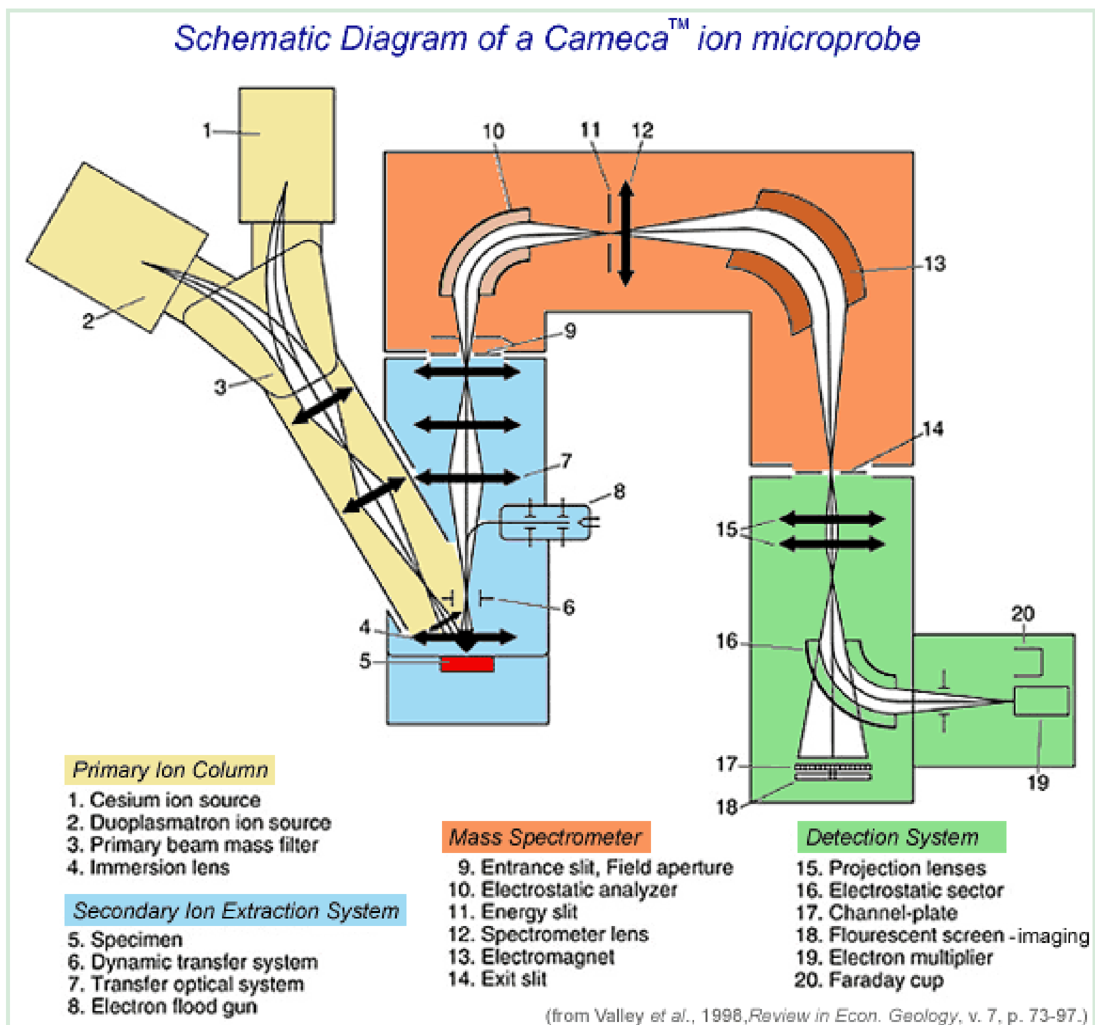

Fig.3.10: SIMS measurement scheme [3.8]

3.2 Electrical Measurements

3.2.1 Hall Effect Measurements

The Hall effect originates by the Lorentz force that is induced on carriers driven by an electric field under the simultaneous presence of a transverse magnetic field. For a single particle having a charge q and moving with a drift velocity ***v*** under a constant electric field E, the electromagnetic force is given by:

$$\vec{F} = q\vec{v} \times \vec{B} \tag{3.4}$$

If we consider an electrical current flowing along the x and a magnetic field B= (0,0,B), oriented along the z-direction, an electrical field E_y along the y- direction is built up and the related voltage is the Hall voltage.

The general experimental scheme for the Hall measurements is sketched in Fig.3.11. Actually, an accurate measurement requires particularly shaped test patterns (six-arms rectangular bar, clover leaf, Corbino disk etc.) which need of particular etching procedures, the availability of special mask and UV photolithographic processes. Nevertheless, the application of the Van der Pauw theorem to a continue surface, having an arbitrary shape, avoids the use of time-consuming technological steps if they are not necessary. Thus, the most popular geometry for the measurements of carrier concentration and mobility through the Hall effect is the Van der Pauw geometry, which is illustrated in Fig.3.12)

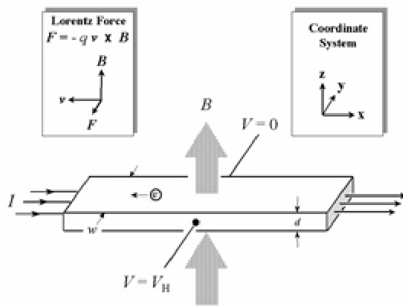

Fig.3.11: Hall measurement sketch [3.9]

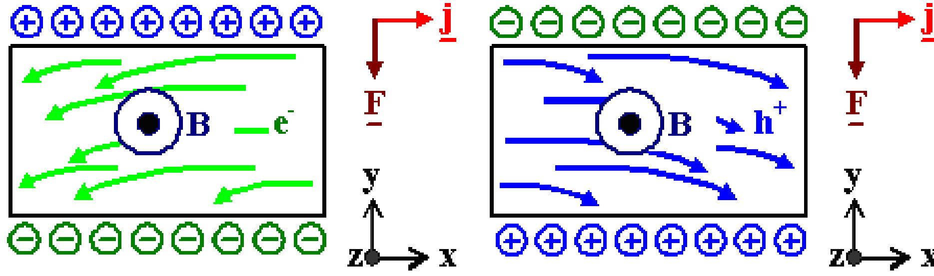

Fig.3.12: Hall effect on electrons and holes in a semiconductor sample [3.10]

The steady state equation of motion is showed in the 3.5 [3.11]

$$m^* \frac{\partial \vec{v}}{\partial t} = q\left(\vec{E} + \vec{v} \times \vec{B}\right) \tag{3.5}$$

for a strongly extrinsic case (n>>p or p >>n), only one type of carrier (majority carrier) can be considered, so that the drift velocity and the current density can be expressed as:

$$v_x = \mu E_x \tag{3.6}$$

and :

$$J_x = \sigma E_x = qnv_x \tag{3.7}$$

and by keeping the condition j_y=0 it results:

$$E_y = -\mu B_z E_x \tag{3.8}$$

and

$$j_x = \sigma_0 E_x \tag{3.9}$$

Where μ and j are respectively the mobility and the current density of the majority carriers. For extrinsic semiconductor (n-type or p-type). Assuming the simplest boundary conditions (single carrier, non degenerate condition, single donor and single acceptor approximations, isotropic conduction band and scalar electron effective mass, low electric field etc.) the Hall coefficient is:

$$R_H = \frac{E_y}{j_x B} \tag{3.10}$$

$$R_H = \frac{r_H}{qn} \tag{3.11}$$

Were r_H (Hall scattering factor) is generally approximated to 1.

So that, the Hall coefficient R_H can be calculated by considering the constant B field, applied along the z-direction, by keeping constant the current along the x direction and by measuring

$E_y=V_yW$ (where W is the distance between the Hall contacts and V_y the Hall voltage), at a fixed temperature T.

Moreover, combining the equations 3.8-3.10

$$R_H = -\frac{\mu E_x B_z}{\sigma E_x B_z} = -\frac{\mu}{\sigma} \qquad (3.12)$$

both the carrier concentration , at a fixed temperature, and the electron mobility are directly derivable from the simultaneous measurement of the Hall voltage and of the electrical conductivity (at B=0).

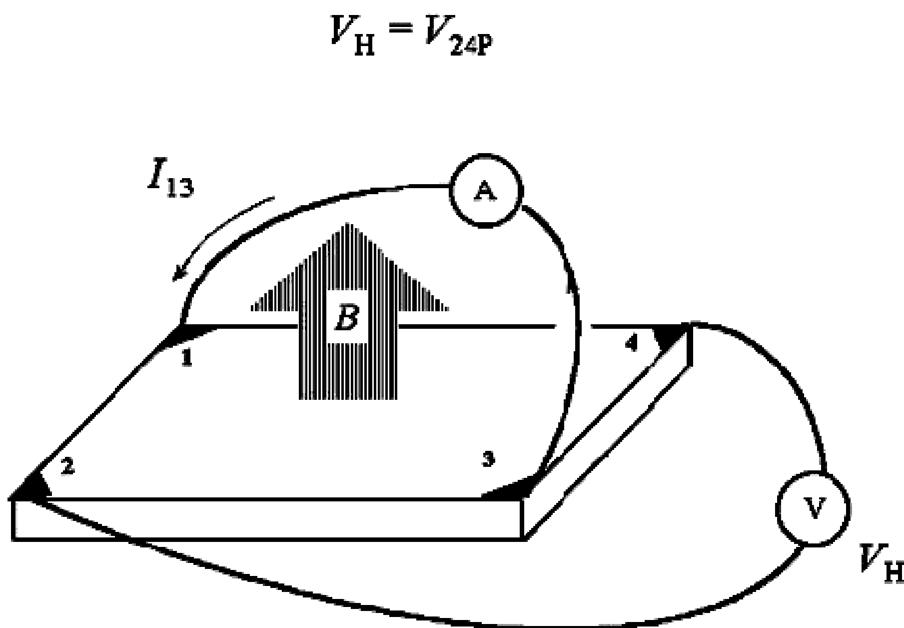

Fig.3.13: Van der Pauw geometry [3.12].

A similar result can be derived, under the same assumptions, if the electrical conductivity of the semiconductor is controlled by shallow acceptor levels (p-type conductivity).

If the Hall measurement are carried out as a function of the temperature, both the variation of the majority carrier concentration (electron or holes in n-type or p-type semiconductor respectively) as well as the energy ionization of the impurity level, which is responsible of the electrical conductivity (shallow donor levels for n-type), are obtainable.

In particular, by considering the logarithm of the carrier density as a function of the reciprocal of T, in a wide temperature range across room temperature, one should expect the behaviour illustrated in

fig.3.14. The density of majority carriers (electrons in the case of n-type semiconductor) changes with the reciprocal temperature following three different regimes.

In the first region, at very low temperatures, the carriers are frozen into the donors levels. Therefore, the free carriers' concentration is very low and increases with the temperature because the electron are ionized into the conduction band. In this low temperature regime (frozen region) n increases with T with an energy activation which is the energy distance of the fundamental state (1s) of the donor level, from the conduction band minimum. In this case, if one takes into account the contribution of both majority and minority carriers (if both acceptors and donors are simultaneously present) at the thermodynamic equilibrium, the charge neutrality equation gives [3.13]:

$$-n + p - N_A^- + N_D^+ = 0 \qquad (3.13)$$

and the majority carrier density has the following expression 3.14 [3.14]:

$$n(T) \approx \beta_1 N_C \left(\frac{N_d - N_a}{N_a} \right) \exp\left(-\frac{E_d}{kT} \right) \qquad (3.14)$$

Where β_1 is the degeneracy factor for the ground state, N_C is the effective density of states in the conduction band, N_d and N_a are respectively the donors and acceptors impurities density and E_d the donor energy level.

According the compensation ratio and the measurement temperature range, two different slope can be obtained in the frozen regime: at very low temperatures. If $n(T)<N_A<N_D$ the exponential n(T) slope is given by E_D/K_B ,while at higher temperatures where $N_A< n(T)<<N_D$ a slope - $E_D/2k_B$ is expected. Thus a semi-logarithmic plot of $T^{-3/2}$ n (T) versus T^{-1} changes its slope from (- $E_D/2k$) to (- E_D/K) as n(T) falls below a value corresponding to N_A. Thus, in this frozen region, the compensation ratio which increases, at higher N_A values, determines the prevalence of one of the two behaviour, varying from ($-E_D/2k$) to ($-E_D/K$), respectively for a low or a heavily compensated semiconductor. Thus, in the cases in which a single-donor single-acceptor model can be assumed, the impurity concentrations N_D and N_A and the donor activation energy E_D can be obtained by fitting the eq. 3.14 to the experimental data.

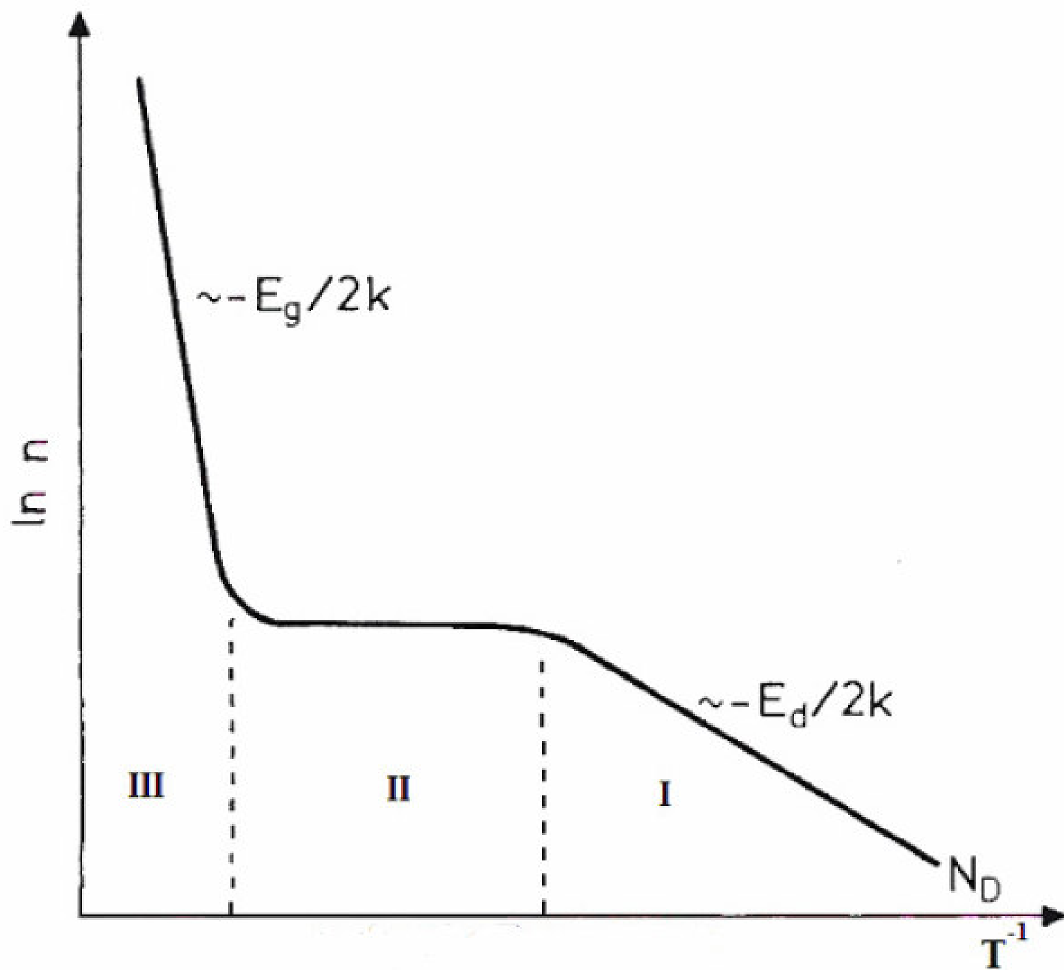

Fig.3.14: ideal behaviour of the semi-log plot of n(T) versus T^{-1} in case of low compensation ratio.

In the second region (exhaustion region), over a certain temperature, all the donor levels are ionized so that no more electrons can reach the conduction band from the donors levels and the electrons density is given by:

$$N = N_D^+ - N_A^- \cong N_D - N_A \qquad (3.15)$$

Where N_D^+ and N_A^- are the density of the ionized donors and acceptors.

In the third region, at temperature higher than RT, the thermal energy is enough to upgrade the carriers from the valence band to the conduction band; the electron density would be determined by the intrinsic carrier, and the activation energy of the log n versus 1/T curve approaches the energy gap of the semiconductor. However, it is significant to specify that this region can be experimentally investigated only in case of low energy gap materials.

3.2.2 DLTS (Deep Level Transition Spectroscopy)

Deep level transient spectroscopy (DLTS, D.V. Lang, J. Appl. Phys. **45**, 3023 (1974)) [3.15] is a very sensitive method to study deep levels in semiconductors. The method is based on the capacitance change of a reverse biased diode when deep levels emit their carriers after they were charged by a forward bias pulse (see the scheme illustrated, fig.3.15).

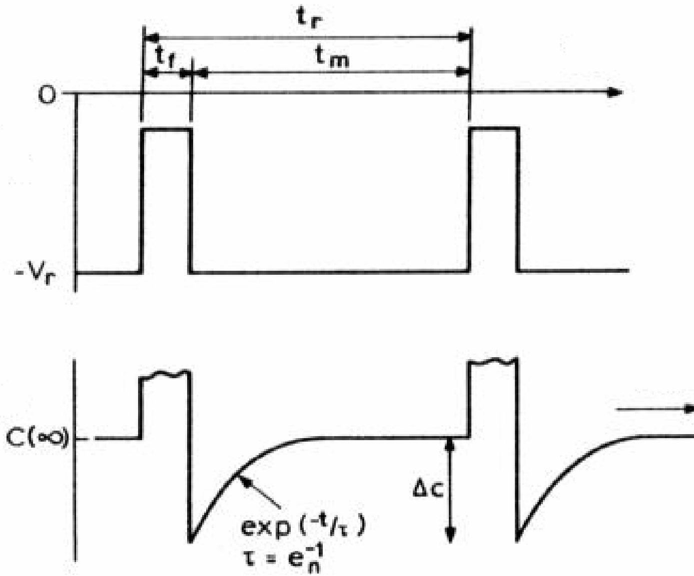

Fig.3.15: DLTS measurement, a) voltage pulses b) consequent capacitance variations; here e_n represents the emission rate of majority carriers out from the traps

The zero bias conditions are maintained for a t_f time, during which the traps are filled with majority carriers. Instead, during the reverse bias pulse, the trapped carriers are emitted with a rate $\mathbf{e_n}$ [3.14]. This emission process produces an exponential transient in the capacitance, which therefore can be written as:

$$C(t) = C(\infty) + \Delta C_0 e^{-\frac{t}{\tau}} \quad (3.16)$$

Where the time constant τ is equal to $(\mathbf{e_n})^{-1}$

It is necessary to consider a "rate window" which provides a maximum output, when the time constant is known as a preset time constant τ_{ref}.

If $\ln(\tau)$ is reported versus T^{-1} different curves are obtained following the majority carrier traps. As the temperature of the diode is increased also the emission rate increases until a peak occurs in the rate window output, when τ passes through τ_{ref}. In fact, the emission rate $\mathbf{e_n}$ is temperature

dependent and characteristic for each type of defect. From the temperature dependence of the emission rate the activation energy of a deep level can be deduced. In particular, by repeating the scan with different values of τ_{ref} , $\mathbf{e_n}$, an Arrhenius plot of T_{pk} versus T^{-1} can be obtained. Therefore, E_{na} (the trap energy activation) and σ_{na} (the trap cross section) can be derived. Indeed every trap has its own characteristic temperature for which $\tau=\tau_{ref}$. The peaks height is also proportional to ΔC_0 that is proportional to the N_t concentration traps. DLTS can usually detect deep levels until concentrations around $10^{11}cm^{-3}$. The sensitivity depends very much on the diodes properties and in particular from the density of shallow doping levels. DLTS makes also possible to measure the capture cross section of a deep level, by varying the pulse width. So making the signal amplitude is varied and a capture cross section can be deduced from this variation. The largest capture cross section one can measure depends on the minimum pulse width (typically > 50ns) and the shallow density of the doping levels. Also the electric field dependence of the emission rate of a deep level can be investigated. By modelling these data it is sometimes possible to identify the defects nature. There are other experimental variations of DLTS technique, widely used, like e.g. deep level optical spectroscopy [3.16], or relatively unknown, like e.g. Acousto-Electric Deep Level Transient Spectroscopy (AE-DLTS) or Q-DLTS. A good overview on DLTS and related techniques is contained in *"The Electrical Characterisation of Semiconductors: Majority Carriers and Electron States"* by P. Blood and J.W. Orton, Academic Press London (1992) (ISBN 0-12-528627-9) [3.14]

3.2.3 C-V Profiling and ECV (Etching Capacitance Voltage)

The measurement of the depletion capacitance can give information about the doping profile. The capacitance depletion is associated with a band bending region of a metal Schottky contact or a p-n junction. By assuming certain approximations, the depletion region, behaves like a parallel plates capacitor.

At room temperature and under a reverse bias, the expression of this capacitance in terms of the total Voltage across the region is:

$$C = A\left(\frac{\varepsilon\varepsilon_0 e N_d}{2}\right)^{\frac{1}{2}}\left(V - \frac{kT}{e}\right)^{-\frac{1}{2}} \tag{3.17}$$

As it follows from the equation a plot of C^{-2} versus applied reverse bias V_r per a homogeneously doped material, is linear and its slope is proportional to $N^{+}_{d}{}^{-1}$ for n doped semiconductors (or N^{+}_{d} <- N^{-}_{a} for compensated semiconductors).

Moreover, from the expression of the bending voltage:

$$V = \frac{eN_d}{2\varepsilon\varepsilon_0} x_d^2 \tag{3.18}$$

By assuming V>>kT/e, the capacitance is the same of that of two parallel plates of area A containing a dielectric of permittivity ε and spaced by a distance equal to the depletion layer width. For a non uniform doped semiconductors a linear plot from C^{-2} versus N_d cannot be obtained but it is possible to calculate the local doping $N_d(x)$ from the local slope of C. In this case the expression becomes:

$$N_d(x) = -\frac{2}{q\varepsilon_0\varepsilon_r A^2}\left[\frac{d\left(\frac{1}{C^2}\right)}{dV}\right]^{-1} \tag{3.19}$$

While the expression that describes C as a function of x_d is the same as previously mentioned since it doesn't depend on the charge distribution in the depletion layer. Thus it is possible to plot N^{+}_{d} (which at a R.T is equal to N_d, the net donor density) profile obtainable from the abovementioned expression (3.18)

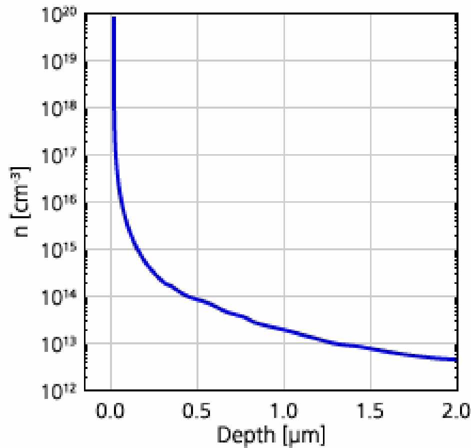

Fig.3.16: Net donor density profile in AlGaN/GaN HEMT Structure [3.17]

A particular C-V profiling technique is the ECV (Etching Capacitance Voltage) Profiler. In this case, a Schottky barrier between the semiconductor surface and an electrolyte solution is exploited, having the semiconductor-electrolyte contact analogy with the semiconductor-metal contact (though in the electrolyte a ionic current is present). The advantage in this case is that, together with a C-V

measurement, an etching at the surface can be induced through an electrochemical effect between the semiconductor and the solution used. It permits a direct doping profile measurement, not limited by the reverse breakdown voltage of a Schokty diode.

As illustrated in figure 3.17, for a p-type semiconductor, the dissolution is induced in case of direct bias voltage through the semiconductor/electrolyte junction. In the case of an n-type semiconductor the free holes (indispensable for the dissolution) must be induced by illumination with an opportune wavelength and the dissolution occurs at reverse bias conditions.

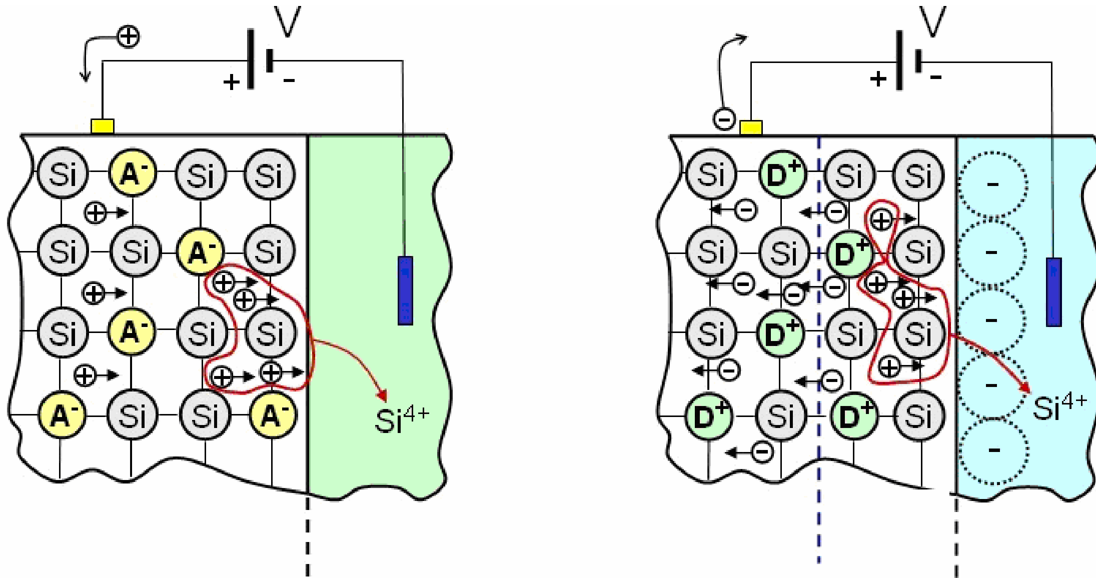

Fig.3.17: Dissolution process in an ECV for a p-type (right) and for an n-type (left) semiconductor.

The depth of the etching, in dependence of the process time, is given by the Faraday's law.

$$W_r = \frac{M}{zF\rho A}\int_o^t I dt \tag{3.20}$$

Where M is the molecular weight, F the Faraday constant, A the etched area, I the current, ρ the mass density of the etched material and z the atomic specie valence.

But one should consider that the measured region is beyond the depletion layer, in this way the profile depth is: $W_r + W_d$ where W_d is the depletion layer.

Using again the previous expression for C (3.19), it is possible to measure the doping densities as a function of the depth.

3.2.4 I-V measurements

The I-V measurements are useful to analyze the electrical properties of semi-insulating regions, for example caused by the electrical compensating effect produced from the deep acceptor centres introduced through ion implantation into a semiconductor of n-type conductivity.

An accurate analysis of the transport mechanism, controlling the electrical conductivity in such layers, lets to determine the concentration of the activated impurities, as well as the efficiency of the implantation and the ratio of activated traps. By following the Lambert and Mark theory [3.18] which describes the electrical conductivity of semi-insulating materials, the I-V curve can be divided in 4 regions, corresponding to different transport mechanisms (Fig 3.18).

- The first region, at low electric field in which J varies linearly with V (ohmic region): the electrically active traps are mainly empty and the transport is conditioned by thermal electrons, rather than from the injected ones. The transport is therefore ohmic-type, and J is proportional to V. In this condition the resistivity of the material is easily calculable by applying the Ohm's law.
- In the second region, J has a quadratic dependence from V, the density of injected electrons overcomes the thermal ones and the traps capture only a small quantity of these. In this way, the injected carriers dominate the transport and the conductivity is proportional to the square of the voltage.
- In the third region, as the bias voltage reaches the V_{TFL} value (Traps filled limited voltage), for which all the traps are filled by thermal and injected electrons, the carriers further injected increase drastically the current density. As it is shown in the 3.21 , the value of V_{TFL} is dependent from the donors concentration N_D and from the majority trap density N_T including the traps produced from the implantation process.

$$V_{TFL} = \frac{qL^2}{2\varepsilon}\left(N_T - N_D\right) \qquad (3.21)$$

- In the fourth region the injected electrons control the transport mechanism and the J/V characteristic follows a quadratic behaviour.

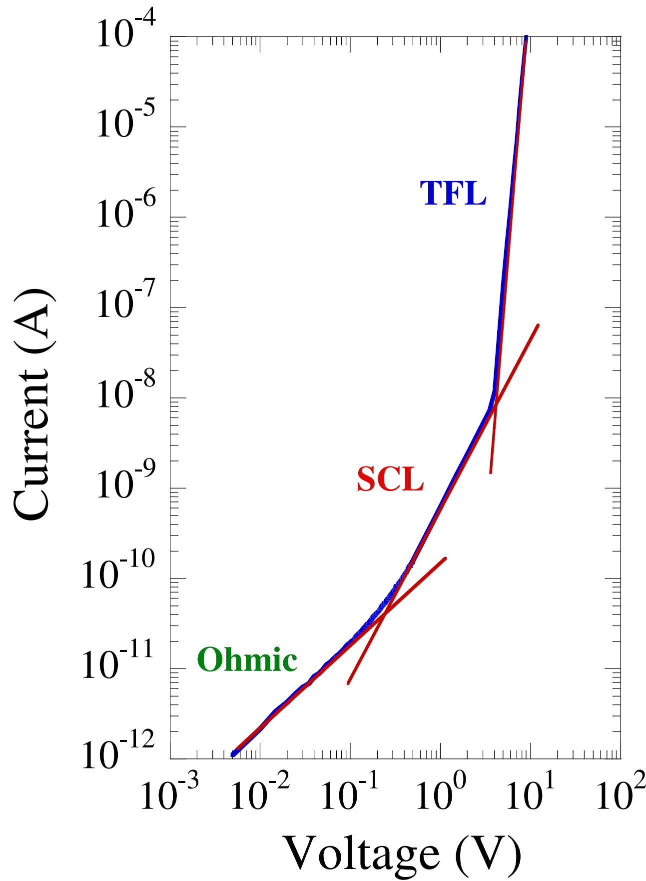

Fig.3.18: Ideal Current-Voltage characteristic [3.19]

3.3 Optical Analysis

3.3.1 PL (Photoluminescence)

The photoluminescence (PL) is a process in which a sample undergoes an exciting light beam with an energy suitable to generate an excess of free carriers. They recombine producing an emission spectra whose properties are strongly determined by the physical properties of the excited crystal. In the case of semiconductors a radiation with an energy higher than the band gap of the material is used, consequently the optical response can be detected. The exciting photons generate an excess of holes-electrons pairs and the different generation-recombination processes determine a stationary state or control the decay to the thermodynamic equilibrium. The recombination transitions can be radiative or not-radiative. If the radiative processes involve defects giving rise to levels, which are localized into the forbidden gap, the spectroscopic study of the emitted photons lets to investigate

some properties of the related impurities. In fact, the consequence of an interaction with visible or near U.V photons, in the case of semiconductors, originates different possible phenomena [3.20]. The most common radiative transition, in direct gap semiconductors, is between states in the conduction and valence bands, (interband transitions). If this latter process is clearly associable to a specific feature of the PL spectrum, it lets to estimate the band gap energy, which is particularly useful in case of ternary or quaternary alloys. If shallow impurities are involved in the recombination processes, the radiative recombination of free electrons or holes into the shallow impurity levels give rise to a light emission whose energy and line shape, detected as a function of the temperature, let to investigate their properties. Not radiative transitions are also possible, (phonons-assisted processes): they are typically related to intermediate centres, deeply localized into the forbidden gap and they control the trapping- emission rates (Schokley-Read-Hall regime). In presence of materials having high purity and excellent structural properties, the band to band recombination processes take place in the PL spectra at sufficient low temperatures, with an excitonic character (narrow and intense emission peak near to the fundamental band edge); so that they are a clear fingerprint of the crystalline quality of the grown epitaxial layers

At higher temperature the probability of radiative transitions lowers, the band to band emission peak decreases its intensity and broadens because of the competition with phonon-assisted processes and the thermal broadening effect respectively. On the contrary, at lower temperatures radiative recombination are favoured. Therefore, at temperatures of few Kelvin degrees, transitions connected to free excitons or bounded impurity excitons are observable.

The most straight information achievable by a PL measurement is, as already discussed , the valuation of the band gap, energy since the band-band transition, in the most cases, is connected to a main emission peak. Since the gap is a function of the alloy composition, from the energy of the main estimation peak, the molar fraction of the different elements can be estimated. From the study of the spectrum at different temperatures, the nature of different emission processes can be deduced, as well as the optical activation of donors or acceptors impurities.

References III

[3.1] M.Cardona, F.H.Pollak, K.L.Shaklee, J.Phys.Soc.Jap.21,89(1966)

[3.2] D.E. Aspens, J.P. Harbison, A.A. Studna and L.T. Florez, J.Vac.Sci.Technol.A 6 (1988) 1327

[3.3] M. Pristovsek "Fundamental growth processes on different Gallium Arsenide surfaces in Metal-Organic Vapour Phase Epitaxy. PhD Thesis at TU Berlin

[3.4] J.-T. Zettler, K. Haberland, M. Zorn, M. Pristovsek, W. Richter, P. Kurpas, M. WeyersJournal of Crystal growth 195 (1998) 151-162

[3.5] M.L. Swason, in Handbook of modern ion beam materials analysis, edited by J.R Tesmer and M.Nastasi (materials Research Group) Pittsburg, 1995

[3.6] Benninghoven A, Rudenauer FG, Werner HW, Secondary ion mass spectrometry, Basic concepts, instrumental aspects, applications, and trends, J. Wiley & Sons, New York 1987

[3.7] http://www.assing.it/

[3.8] Valley, J.W., Graham, Colin M., Harte, Ben, Eiler, John M., and Kinny, Peter D., 1998 Review in Econ. Geology, v-7, p- 73-97

[3.9] http://www.eeel.nist.gov/

[3.10] http://www.tf.uni-kiel.de/

[3.11] "Semiconductors physics and devices" Mc Graw Hill

[3.12] http://electron.mit.edu/~gsteele/vanderpauw/

[3.13] The Physics of Semiconductors" Marius Grundmann

[3.14] *"The Electrical Characterisation of Semiconductors: Majority Carriers and Electron States"* by P. Blood and J.W. Orton, Academic Press London (1992) (ISBN 0-12-528627-9)

[3.15] DLTS, D.V. Lang, J. Appl. Phys. 45, 3023 (1974)

[3.16] DLTS, A. Chantre et al., Phys. Rev. B 23, 5335 (1981)

[3.17] http://www.ntt-at.com/products_e/epitaxial/index.html

[3.18] Lambert M. and Mark P. Current injection in Solids, New York, Academic, 1970

[3.19] "High temperature Fe implantation in InP: investigation of structural, electrical and optical properties" A.Gasparotto and T.Cesca

[3.20] R.F.Pierret, Advanced Semiconductor Fundamentals: Volume VI, Series Editor

Part II: Study of Iron implantation on InP-based layers grown by MOVPE

Chapter 4

Ion Implantation

4.1 The problem of realizing insulating regions in III-V semiconductors

The research on methods to obtain electrically insulating regions in III-V semiconductors, indispensable to confine the charge flux within the active device region of integrated devices, represents an issue of great relevance in the micro and optoelectronic technology. The achievement of a good electrical insulation implies for example the decreasing of a laser threshold current, and the enhancing of its emission power or, in the case of solar cells, an increase of the conversion efficiency. The classical insulating methods, based on the oxide formation obtained by thermal processes (SiO_2 for Silicon) are not applicable in the case of compound semiconductors; the main reason resides in not stable oxides, which do not guarantee a perfect electrical insulation. Moreover, the use of Oxygen could cause the metallic alloy species oxidation.

On the other hand, the residual impurities concentration, for III-V compounds, is not controllable like in Silicon, therefore the presence of stoichiometric defects has to be considered, since it induces a really high residual concentration (for example higher than 10^{15} cm^{-3} for GaAs). A typical method for the carriers flux confinement is the realization of "mesa" structures, namely structures developed in height through selective chemical etching and photolithographic processes.

4.2 The compensation effect

The compensation effect is obtainable by introducing some impurities into a material, able to lower the residual free carrier concentration. Such impurities, transition metals or intentional stoichiometric defects, move the Fermi level to the gap centre, producing a semi-insulating material. We consider the example of a semiconductor with a residual acceptors density A and donor concentration D, where D>>A, both shallow type (hydrogenoid kind, with an energy level near to the top or the bottom of valence and conduction band respectively) [4.1]. In the case in which the occupied level is such that ε_D>kT at room temperature, the donors are only partially ionized, while the acceptors are completely ionized ($A=A^-$). We could control the Fermi energy variation with respect to the introduced acceptors, following the relation that comes from the conditions mentioned above and D>A>n:

$$E_F = E_C - \varepsilon_D + k_B T \log \frac{g_0 (D - A)}{A} \tag{4.1}$$

Where g_0 is the donor level degeneracy degree. It can be noticed how the Fermi Energy level position depends on the ionization energy of the introduced species and on the compensation ratio A/D. If the introduced acceptors are shallow, a compensation doesn't occur since a slight variation of the D/A ratio would have the effect to invert the conducibility, for example from n to p. Instead, in case the impurities introduce a deep level, E_D>>kT, near the middle of the Energy gap, even by varying the compensation ratio, the Fermi Energy remains unchanged, generating a semi-insulating material, in which the free carriers in the conduction and valence band turn to be low. The deep levels introduce a strong perturbation in the crystal, such that the effective mass approximation is no more valid.

For what concerns deep levels, the approach is much more complicated. The bound electron, whose wave function is highly localized, interacts strongly with the crystal, increasing the possibility of phonon emissions. The deep centre therefore acts like an electronic trap or non-radiative (4.2) recombination centre. An electron trap prevalently captures electrons while a holes trap captures holes. A recombination centre involves both holes and electrons, which recombine before going back to their bands. Summing up, the impurities connected to deep levels influence the Fermi Energy, forcing it to the middle of the gap and decreasing drastically the free carrier density. Moreover, the impurity scattering probability increases, reducing the mobility. Therefore, a strong increasing of the resistivity and the realization of a semi-insulating semiconductor occurs.

4.3 The Iron role in InP and InGaP

Iron, among transition metals, represents one of the most suitable elements acting as compensating defect in Indium Phosphide and InGaP. Due to its electronic configuration, (Ar)d6s2 in a InGaP lattice, it is electrically active, substituting cations, therefore replacing Indium or Gallium and providing two electrons in the s shell and one in the d ones. The other d shells are responsible of optical and electrical properties, defining two possible Fe oxidation states (Fe^{3+} neutral and Fe^{2+} negatively charged), the first acting like a free electrons trap, while the second appears when the neutral species are ionized by electrons. The energy level places at 0.74 eV (fig.4.1b) above the valence band, very close to the middle of the gap. The Iron levels, due to the crystal field interaction [4.2], split in two different energies separated by 0.37 eV (fig.4.1 a). This effect gives, in the case of InP, a photoluminescence signal, with possible applications in sensors operating in mid-IR field [4.3].

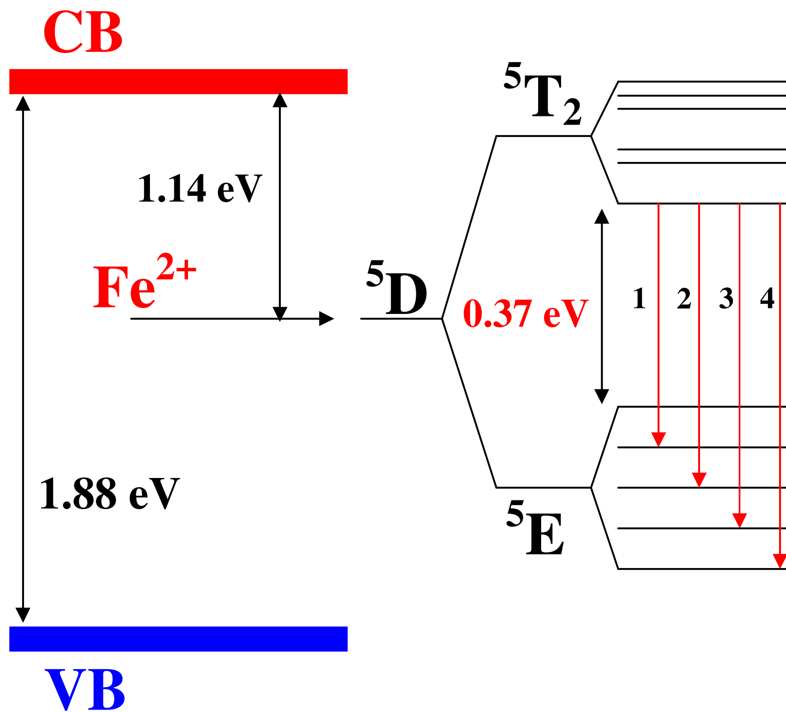

a)

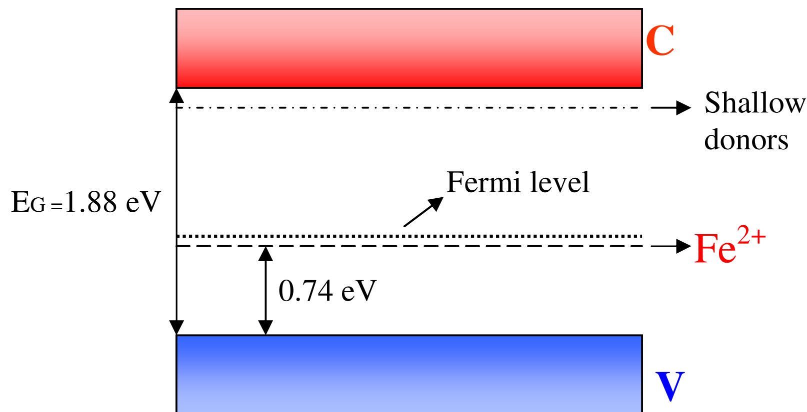

b)

Fig.4.1: a) Fe^{2+} energy split due to crystal field b) Fe^{2+} energy level in InGaP

Above a certain concentration, $10^{17}cm^{-3}$, that is the solubility limit of Iron in InP or InGaP, the activated Iron reaches the limit value and the excess introduced quantity tends to form precipitates like Fe-P [4.4]. The electrically active Iron is that in substitutional position, but it can be also placed in an interstitial position or form clusters. The precipitates on their own act like "gettering centres" for other Fe atoms, which, diffusing during the annealing treatments, pile on those regions impoverishing the others and limiting the semi-insulating properties of the material [4.5]. For this reason, it is easy to argue how, for the obtained compensation with Fe in these systems, the techniques operating in thermal equilibrium conditions (as diffusion after or during growth) are effective only in case of medium doping levels (between 10^{15} o 10^{16} cm^{-3}). When semi-insulating regions should be obtained from highly doped materials (10^{18} or 10^{19} cm^{-3}) not equilibrium techniques are more advantageous.
In these cases, the thermal equilibrium must be overcome, so that the Fe concentration could go beyond the thermal solubility. This is one of the most important advantages for using ion implantation in device compensation.

4.4 Ion Implantation system

The doping techniques that work at equilibrium are based on the possibility to dilute the compensating element into the matrix, in thermodynamic equilibrium conditions. Among these, the

most common is the thermal diffusion, in which the impurity is diffused in the hosting material by thermal activation through the wafer surface, at temperatures between 800 and 1200°C.
The implantation is instead a "non-equilibrium" technique in which ions are accelerated at high energies (from a few keV to some MeV) toward the material that has to be compensated (scheme shown in Fig.4.2). The impurity concentrations of atoms introduced by ion implantation generally overcome the solid solubility limit, up to metastable conditions that depend on the system kinetics and not on thermodynamics.

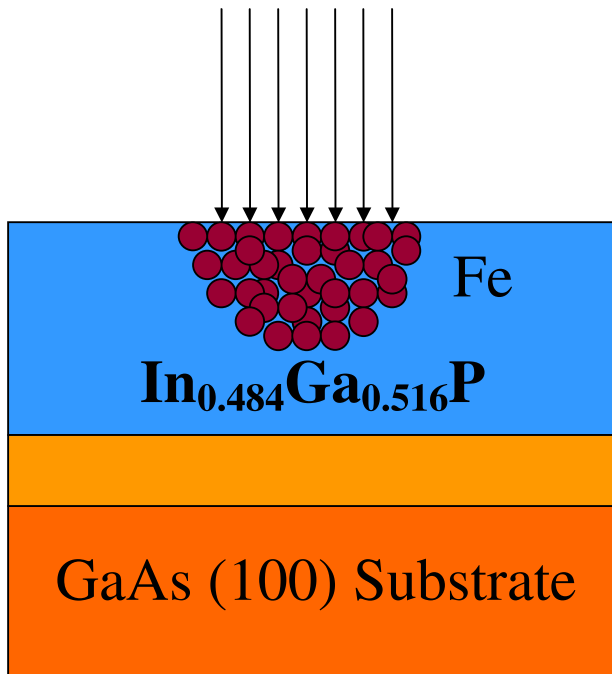

Fig.4.2: Sketch of ion implantation into an InGaP/GaAs layer.

4.4.1 Comparison between implantation and diffusion

As already said, using ion implantation for the impurities introduction into materials, can allow to overcome the solubility limit, impossible for diffusive techniques; this fact allows to reach impurity concentrations also higher than $10^{20}cm^{-3}$ and to compensate highly doped matrixes.
Other differences between implantation and diffusion are described in figure 4.3. In the diffusion case doping is isotropic, Fig.4.3(a), namely the introduced impurities do not follow a preferred direction and therefore they outboard much with respect to the surface mask limits, influencing also

undesired regions. In the case of implantation, the ion motion does not respond to diffusion mechanisms but it is connected to the acceleration energy used and to the stopping action of the matrix atoms. This leads, in the case of implanted materials, to lower outboards and to achieve concentration peaks in the bulk (with an energy dependent depth) and not at the surface.

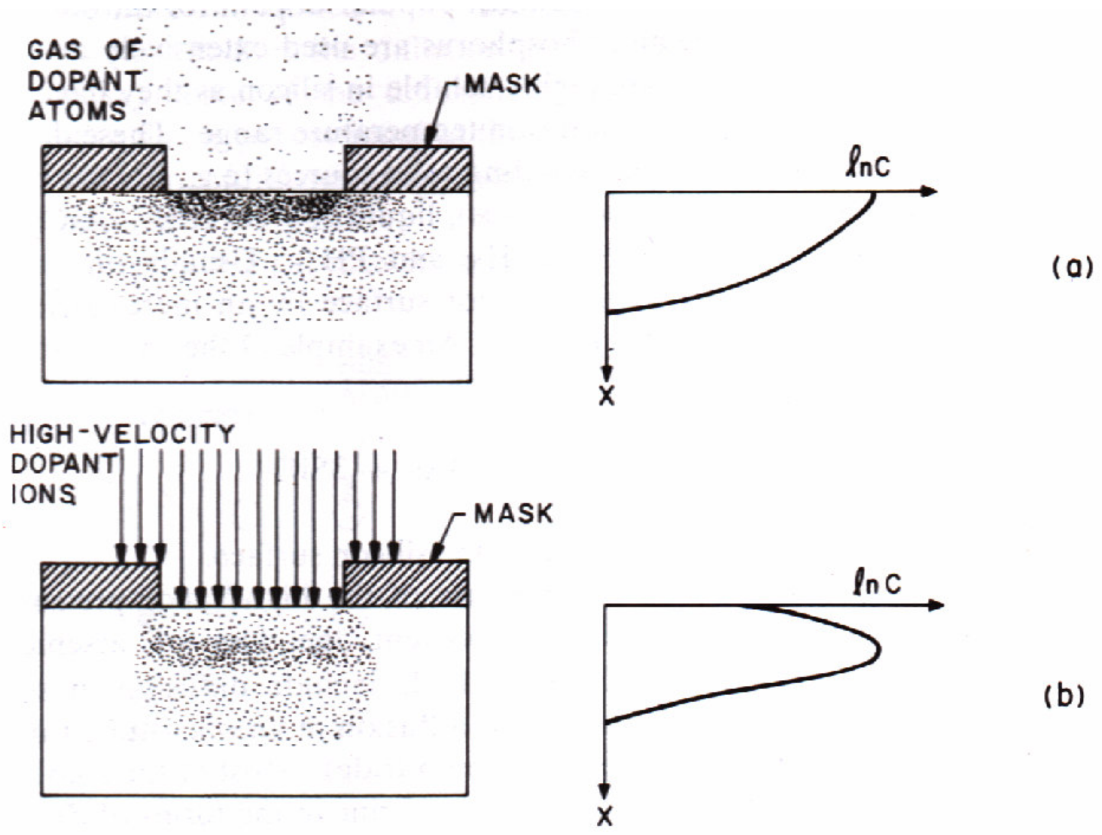

Fig.4.3: Comparison of diffusion and ion implantation technique [4.6].

It is possible therefore to regulate the layer depth by modulating the ion beam energy. In case a highly selective and defined doping is necessary, or for realizing buried structures, implantation appears unequivocally advantageous. One example is represented by buried structures like the planar ridge heterostructure lasers in fig.4.4. On the other hand, the process, in comparison with diffusion, results more complex and expansive, since the machineries are elaborated and the time process higher, leading to a lower productivity.
Moreover, the accelerated ion beam causes a structural damage, such as crystal distortions and defects formations, which should be taken into account.

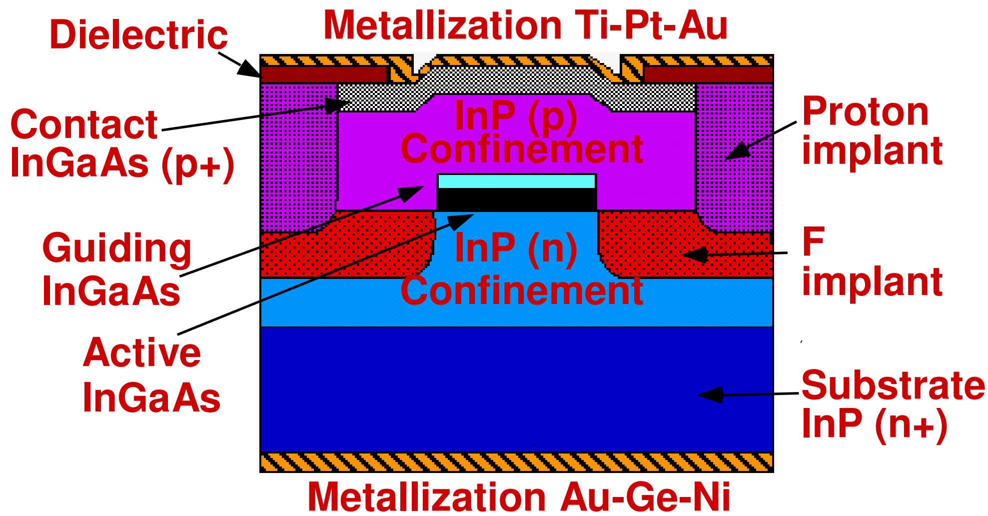

Fig.4.4: Scheme of a Planar Buried Ridge Structure [4.7]

4.4.2 Basic Physics of implantation

The accelerated ions, once implanted, lose their energy in consequence of interactions with the charged particles into the crystal (lattice ions, electrons). The penetration depth (R, range) can be calculated "a priori" considering the incident beam energy. The phenomenon has a statistical nature, therefore the description can be faced in term of distribution; the implanted ions distribute following a trend, as a first approximation of Gaussian type, centred in the averaged value, at a R_p depth (projected range) and with a full width at half maximum, or standard deviation, ΔR_p, both connected to the implantation conditions and the host matrix [4.6]. The profile is influenced (a part from the implantation energy) by the doses, expressed with Q and measured in atoms/cm^2. It is directly measurable (therefore calibrated) through an ion current estimation, measured on the sample.

$$Q = \frac{1}{q_i}\int J dt' = \frac{Jt}{q_i} = \frac{It}{q_i A} \qquad 4.3$$

Where Q is the doses, J the ion current density, A is the area (cm^2), impacted by ions per time unity. The ion stopping by matrix occurs because of three kinds of interactions:

- Collisions with nuclei shielded by electrons shells, by which the Fe ion is deflected and the matrix atoms, in case the energy is high enough, can be displaced producing crystal damages.
- Anelastic collisions with free or bound electrons, with consequently possible excitations or ionizations

- Charge exchange with lattice atoms (phenomenon with irrelevant energetic exchange in comparison with the first two).

The total stopping power, that is the energy lost by the implanted ion, is defined as:

$$S(E) = -\frac{1}{N}\left(\frac{dE}{dx}\right) \qquad 4.4$$

and it is formed by nuclear and electronic interactions contributions. From the separated calculation of the two elements, the R depth of the single ion during motion can be evaluated, using the expression:

$$R = \int_0^z dz = \frac{1}{N}\int_0^{E_0} \frac{dE}{\left|S_n(E) + S_e(E)\right|} \qquad 4.5$$

But it is easier and more useful to consider the beam collective motion in statistical terms, and not the single ion, therefore R becomes the already mentioned R_p, projected range. So that the statistical distribution can be estimated by an approximation, LSS (Lindhard, Scharff, Schlott). This model is based, substantially, on the hypothesis of a Gaussian distribution, where S_e and S_n (so the nuclear and electrons interactions) can be separately calculated. The nucleus interaction involves a scattering with a Coulombian screened potential, the energy exchanged depends on the ion and implanted matrix mass, and on the implantation energy, following the expression:

$$\Delta E_{Trans} = \left[\frac{4M_{Fe}M_T}{\left(M_{Fe} + M_T\right)^2}\right]E_0 \qquad 4.6$$

That acquires generality when a scattering angle is considered.

$$\Delta E_{Trans} = \left[1 - \frac{\sin^2 \Phi}{\sin(\Phi + \theta)}\right]E_0 \qquad 4.7$$

ΔE_{Trans} increases as the implantation energy increases, up to reach the maximum; after that it decreases because the interaction time becomes so small that it makes always less probable the momentum transfer.

ΔE_{Trans} is different if the electrons interactions are considered. In this case the given energy is simply proportional to the square root of the implant energy. Different trends are observable in Fig.4.5.

E_c increases by increasing the implanted ions mass

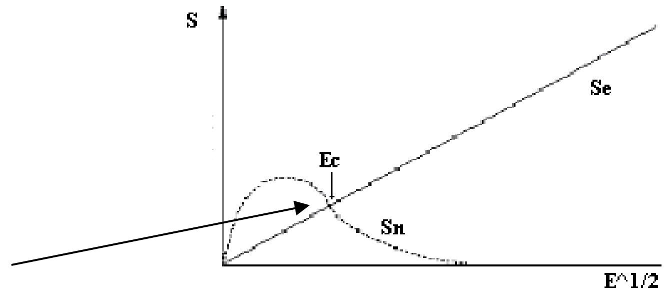

Fig 4.5: Different trends of S_n and S_e changing Energy [4.6].

The crossover after that the electronic contribution overcomes the nuclear one is very important. In fact, the cause of crystal damages are the nucleus interactions and the crossover, E_c, enhances with the mass of implanted ions increasing.

Once quantified the stopping power, it is possible to evaluate the ions distribution, which can be expressed with the following expression that has a Gaussian shaped function.

$$N(x) = \frac{Q}{\sqrt{2\pi}\Delta R_p} \exp\left[-\frac{(x - R_p)^2}{2\Delta R_p^2} \right] \quad 4.8$$

From which the peaks changing energy can be derived as shown in Fig.3.6.

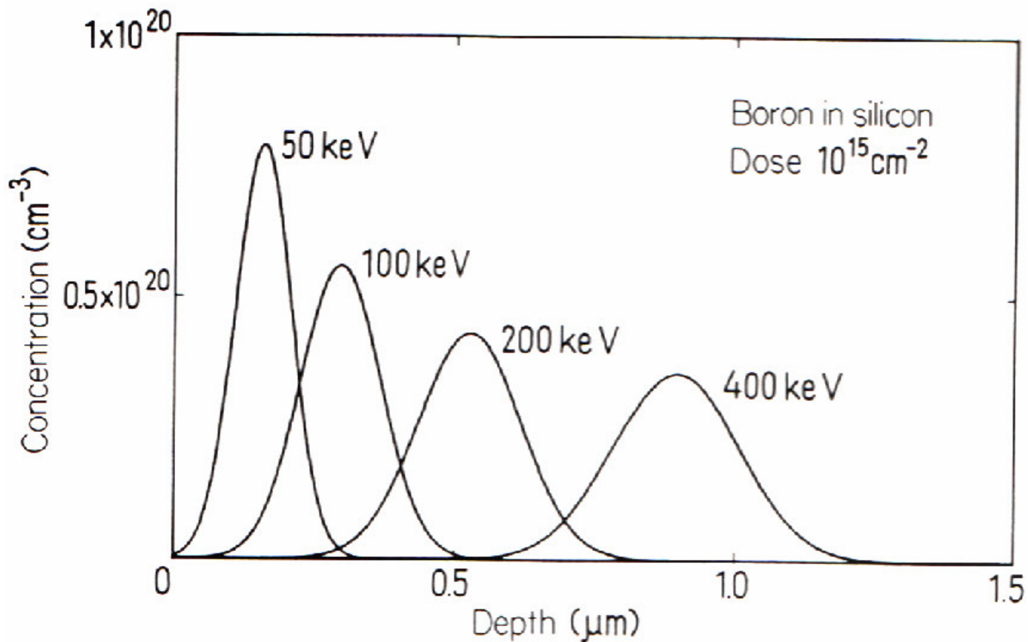

Fig. 4.6: Gaussian profiles at different implantation energies [3.6].

Obviously, the real profiles do not exactly follow the calculated ones. We did not consider in fact the sample structure, constituted by preferential crystal channels, defects or clusters, backscattering phenomena, for which ions can be rejected from the surface without being implanted. Further, we did not take into account the crystal damage consequence of the impact with first ions. All this effects would lead to different distribution profiles, as those in fig.4.7 and 4.8.

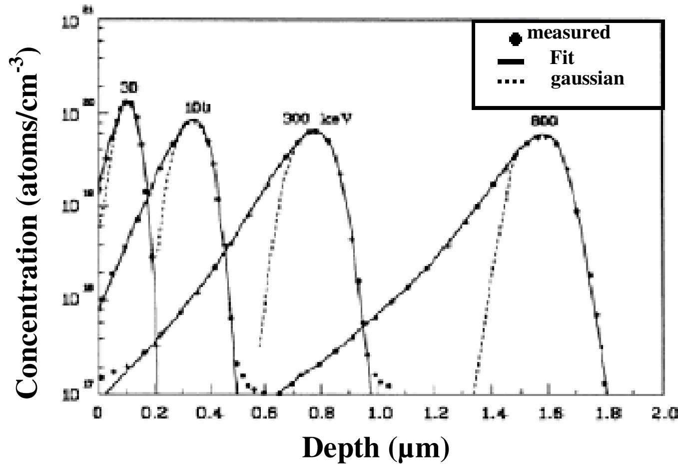

Fig.4.7: Real distribution profiles due to damage [4.6].

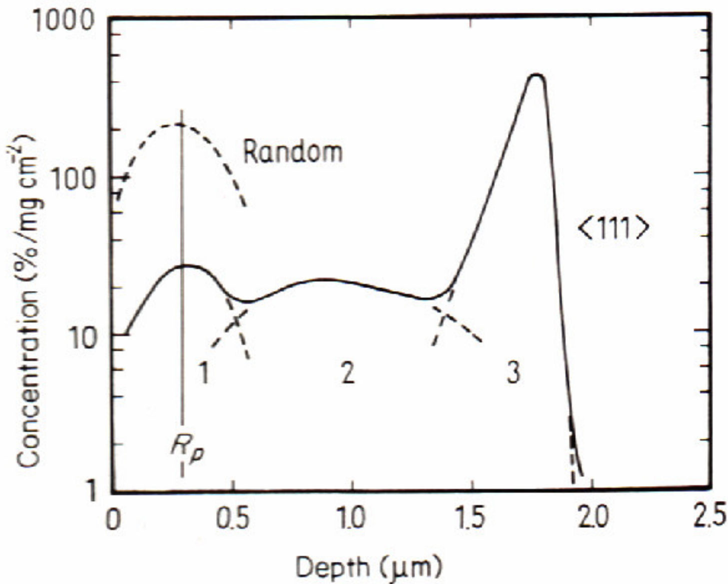

Fig. 4.8: Real profiles due to de-channelling [4.6].

4.5 Implantation damage and annealing processes

The damage after implantation occurs when some atoms are removed from the crystal sites because of the impact with accelerated ions. This impact provokes more or less complex defects. The difference between formed defects depends on the implanted ion weight, therefore on its atomic number. As described in the picture in fig.4.9, a light ion tends to form primary defects because the stopping effect is mainly caused by electrons. On the contrary, a heavy ion origins more complex defects, as amorphous clusters, defects that negatively influence the devices performances.

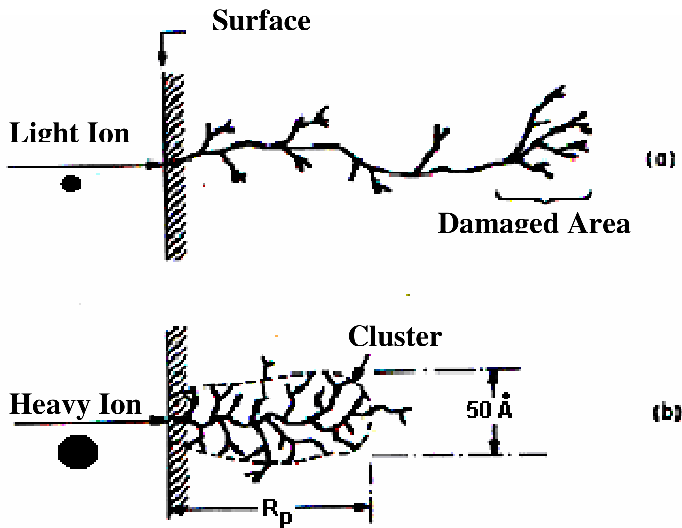

Fig. 4.9: Effect of light and heavy ions on the damage [3.6].

The primary impacts cause atom replacements from substitutional sites, generating a Frenkel pair, vacations and interstitials. A critical dose, anyway, exists, defined as Q_c, above which a further addition of ions provokes a cascade of defects, until a complete amorphization in the sample. This value depends on the energy exchanged from the lattice to the ions and on the implantation conditions: in particular, it increases as the temperature grows. This implies that a thermal process during implantation (so called dynamical annealing) would result very useful.
To remove the damage, a thermal process is necessary, that consists in submitting the just implanted sample to some thermal cycles, at temperatures between 400°C and 900°C for times around 30 and 90 minutes. The thermal energy created during the process supplies the required potential to activate those processes that bring back the system to the thermodynamic equilibrium. The recover of the damage through processes as point defects annihilations is favoured. In this way, the impurity moves from an interstitial position, electrically inactive, to a substitutional one. Such to come back in the situation:

Vacation + Interstitial = Substitutional

Moreover, high temperatures allow the clusters dissociations and the dislocation and stacking fault reorganization. For what concerns dislocations and stacking faults, that are complex defects, a post-implantation annealing is not able to promote a removal, as for primary defects, but only a reset, a sort of reorganization and migration toward a lower thermal energy system.

Anyway, there is the possibility to minimize the extended defects formations by using dynamic annealing. Operating implantation at high temperatures, around 200°C, in ion implanted InP samples, it is possible to avoid complex defects formation obtaining the total recover after post-implantation annealing. The unwanted effects after thermal processes have to be considered, especially the thermal diffusion, which enhances the outboard from implanted regions. A consequence of atoms migration is also the accumulation in highly defected regions, which causes undesired concentration peaks in some regions and poor concentrations in others, as observed in recent studies for InGaP [4.8]. The annealing substantially provokes a lowering of the implanted species solubility limit, forcing it to the thermodynamic value. Anyway it is more important trying to bring the material back to the crystal and electrical quality before implantation, and considering this requirement, the necessity of thermal processes is clear.

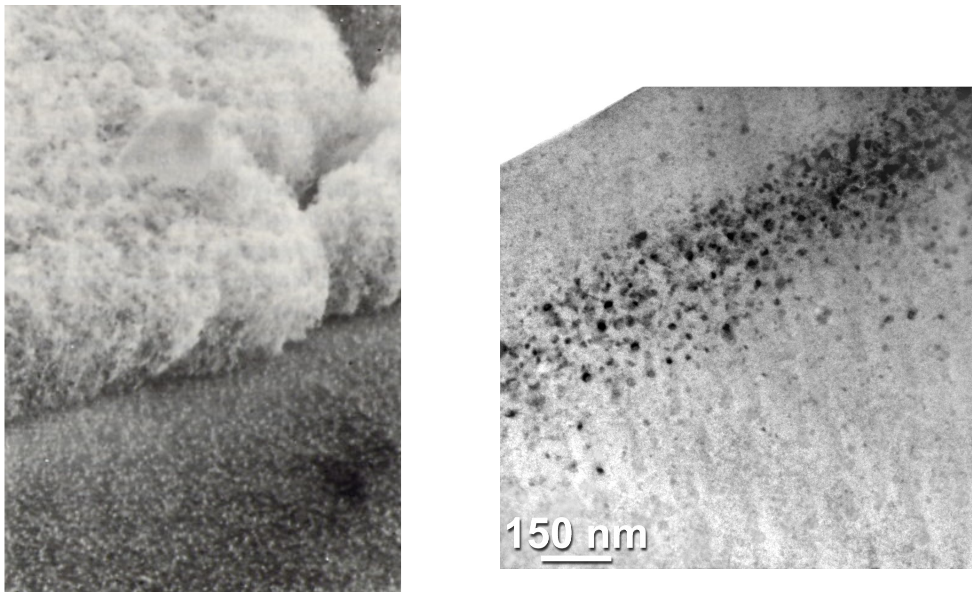

Fig. 4.10: Effect of implantation on the surface (a) and cluster formation after annealing (b).

References IV

[4.1] C.Ghezzi, A.Parisini, L.Tarricone, R.Mosca, E.Gombia, Fisica, Tecnologia ed applicazioni dei semiconduttori composti Vol.II MURST, 1995

[4.2] T.Takanohasi,11th intern.Confer. on Indium Phosphine and rel.mat. 16-20 Maggio 1999

[4.3] G. Scamarcio, F. Capasso, A.L. Hutchinson, T. Tanbun-Ek, D. Sivco and A.Y. Cho *Appl. Phys. Lett.* 68 (1996), p. 1347.

[4.4] A. Gasparotto, A. Carnera, A. Paccagnella, B. Fraboni, F. Priolo, E. Gombia and R. Mosca *Appl. Phys. Lett.* 75 (1999), p. 668

[4.5] A. Cesna, D. Söderström, S.Marcinkevićius, and S Lourdoudoss J.Appl.Phys. 85 1234 (1999)

[4.6] H.Ryssel, I.Ruge: "Ion Implantation", John Wiley & Sons: New York, 1986.

[4.7] "High temperature Fe implantation in InP: investigation of structural, electrical and optical properties" Andrea Gasparotto and Tiziana Cesca.

[4.8] T. Cesca, A. Verna, G. Mattei, A. Gasparotto, B. Fraboni, F.Boscherini, M.Longo, L.Tarricone Nucl. Instrum. Meth. B n. 257 p. 332 (2007)

Chapter 5

InGaP/GaAs

Iron doping is largely used on InP-based materials to realize semi-insulating bulk crystals (as wafer substrates) or epitaxial layers. In the past, the possibility to introduce iron in InP matrixes through implantation was deeply studied. It was observed that n-type doped layers can be compensated through iron implantation, producing a limited damage, well recovered also with proper annealing. The ternary materials, under this aspect, are less studied. But InGaP or InGaAs alloys, as already mentioned, present really interesting properties in terms of high mobility and optical properties.
In this section we will present experimental results regarding the effect of Iron implantation in InGaP. To this purpose, the first step is the optimization of the InGaP growth by MOVPE, starting from undoped layers up to an assessment of n-doping in the way to obtain samples suitable to be implanted. The optimization work is based on the methodical analysis of samples by structural, optical and electrical measurements such to correct, step by step, the growth parameters particularly concerning the achievement of the lattice match with the substrate, minimization of the background impurities and a good optical quality.

5.1 Deposition of undoped InGaP/GaAs layers

The first step for the project has been the optimization of the bulk-like InGaP ternary alloy grown by MOVPE, starting from undoped (or, better, unintentionally doped) layers. The goal was to obtain the ideal parameters conditions to realize an InGaP layer with thickness around 1 µm, lattice matched to the GaAs (100) substrate, with a Si doping giving a donor density variable in the range 10^{16}-$10^{19}cm^{-3}$, suitable for iron ion implantation studying. To this purpose, a systematic study on many samples, grown under different conditions, was carried out.
The grown heterostructures, in most of cases, were composed as sketched in picture 5.1: on a GaAs substrate, previously cleaned (as further described), a 300 nm GaAs buffer layer was deposited, and then, an InGaP layer was grown. At the end a thin GaAs cap layer, useful for electrical measurement contacts, was deposited on the surface.

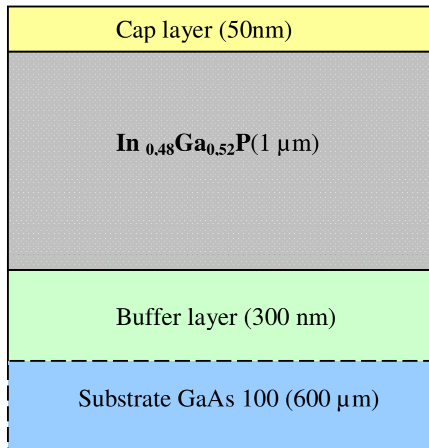

Fig.5.1: General scheme of a typical InGaP/GaAs growth

Focusing on the unintentional doped layer growth, beyond the achievement of the lattice match, the conditions to minimize the unintentional impurities were searched. Even a minimum deviation from the lattice match conditions, that in the case of $In_{1-x}Ga_xP$ are predicted for an Indium concentration of 48.84%, causes a strong increasing of the lattice strain, compressive or tensile. As a consequence, the critical thickness is notably reduced and when this thickness is overcome the formation of structural defects is induced. The grown material will present, in this way, a low structural quality, with the presence of many dislocations. The strong strain variation occurring when moving away from the right match conditions is caused by the rapid modulation of the lattice parameter in the InGaAsP alloys type.

However, given the strict condition to achieve a lattice match, it is currently impossible to grow a dislocation free InGaP/GaAs heterostructure, thicker than 1.5 µm. These aspects are described in the Matthews-Blakeslee model, elaborated for the InGaP/GaAs case, presented in chapter 1, Fig 1.4.

5.2 Substrate preparation

The substrates used for InGaP epilayers were GaAs semi-insulating wafer (the typical size used is a quarter of a 2 inches wafer), grown from the melt in <100> direction. Before the deposition process the substrates have to be treated, to remove residual organic and/or inorganic contaminants [5.1]. It

is previously cut along the <110> direction, removing particulates through ultrapure nitrogen flux. Then a cleaning begins: at first it must be immerged in isopropylic alcohol and rinsed in de-ionized water. In this way it is possible to remove hydrocarbons and general impurities on the surface. Subsequently the wafer is cleaned with heated Hydrochloric Acid, which is useful to remove the non stoichiometric oxides. Moreover, it allows to deposit a fresh and thin surface oxide layer. This latter is then thermally removed from the substrate surface in the deposition chamber, keeping the substrate at 600°C for 5 minutes before the growth, under Hydrogen atmosphere and TBAs, to prevent the incongruent As desorption.

5.3 InGaP/GaAs growth conditions

The features of the samples grown to perform the above mentioned systematic study are presented in the following table, tab.5.1.

The different deposited samples, named in sequence, are listed below, with their own growth details (precursor fluxes used with corresponding nominal Indium percentage and V/III ratios, and growth Temperature), and their properties observed after growth (their Indium concentration, measured by HRXRD, their electrical characteristics, in particular mobility and background doping concentrations).

Sample	TMGa Flow (sccm)	TMIn Flow (sccm)	TBP Flow (sccm)	V/III Rat.	Nom. In %	Meas. In %	T(°C)	Holes Density (cm^{-3})	Surface Aspect	μ (cm^2/Vs)
IGP1	10	70	60	14	55	49,6-51,7	600		Mirror Like	
IGP5	10	66	65	15,63	53,6	48,5	600		Mirror Like	
IGP13	8	80	70	21	53,8	43,5	600		Mirror Like	
IGP14	8	80	100	30	53,8	43,5	600		Mirror Like	
IGP15	10	66	100	24	53,6	45,8	600		Mirror Like	
IGP16	10	66	65	15,6	53,6	44	600		Cross Etched	
IGP19	10	66	150	36,1	53,6	44	600		Milky	
IGP26	10	70	60	14	55	49,7	600	$5X10^{16}$ (ECV)	Locally Milky	
IGP27	10	66	65	15,6	53,6	46	600	$1,1X10^{16}$ (Hall)	Cross Etched	164,27
IGP28	10	70	100	23,3	55	45	600		Mirror Like	
IGP29	10	70	40	9,37	55	44,8	600	$1,2X10^{16}$ (Hall)	ML + heavy cross etches	128,7
IGP30	10	70	60	14	55	52,2	550	$1,9X10^{16}$ (Hall)	Mirror Like	150,76
IGP 31	10	70	60	14	55	44,7	650		Light Milky	
IGP32	10	70	60	14	55	47,6	565	$2,8X10^{16}$ (Hall)	Mirror Like	136,22

Sample	TMGa Flow (sccm)	TMIn Flow (sccm)	TBP Flow (sccm)	V/III Rat.	Nom. In %	Meas. In %	T(°C)	Holes Density	Notes	µ
IGP33	10	70	60	14	55	46,3	580	$4,4X10^{15}$ (Hall)	Mirror Like	190,2
IGP34	10	70	80	18,6	55	46,7	600	$8,8X10^{15}$ (Hall)	Mirror Like	163,21
IGP35 (sub.not etched)	10	70	80	18,6	55	50,2	565	$3,0X10^{16}$ (Hall)	Milky	151,30
IGP36	10	70	60	14	55	48	565	$3,0X10^{16}$ (Hall)	Mirror Like	
IGP37	6	45	55	21	56,7	Povero in In	600	$3,2X10^{18}$ (Hall)	Satined	
IGP38	10	70	60	14	55	47,7	565	$7,6X10^{16}$ (Hall)	Locally Satined	
IGP39	10	70	60	14	55	48,2	565	$9X10^{16}$ (Hall)		
IGP41	10	70	60	14	55	47,5	565			
IGP42	10	70	60	14	55		565			
IGP43	10	70	60	14	55		565			
IGP44	10	70	60	14	55		580	$1,9X10^{16}$ (Hall)		
IGP45	10	70	60	14	55		580			

Tab.5.1: Parameters and characteristics of the different InGaP samples.

It can be observed how the achievement of conditions close to the lattice match is not easy. In spite of this, a certain number of InGaP samples, showed a lattice match, with an Indium concentration of 48.8%, or conditions really near to this target and that however guaranteed dislocation free layers. After the analysis and the improvement of some technical aspects, correlated to the MOVPE growth process, a study on the Indium percentage incorporated in the alloy and of the unintentional doping concentration, varying some parameters like temperature and V/III ratio (the ratio between V reagents and III reagents in vapour phase) was performed, as shown in Fig.5.2 and 5.3.

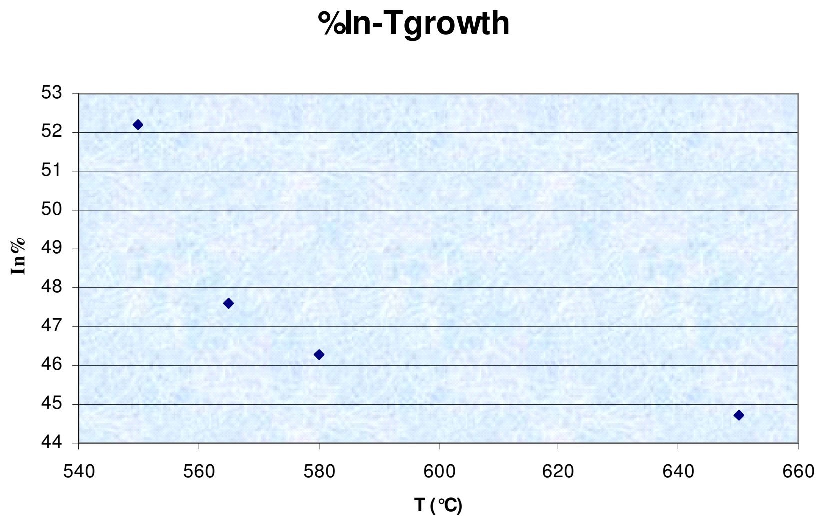

Fig.5.2: Indium percentage content in InGaP, measured by HRXRD versus growth temperature

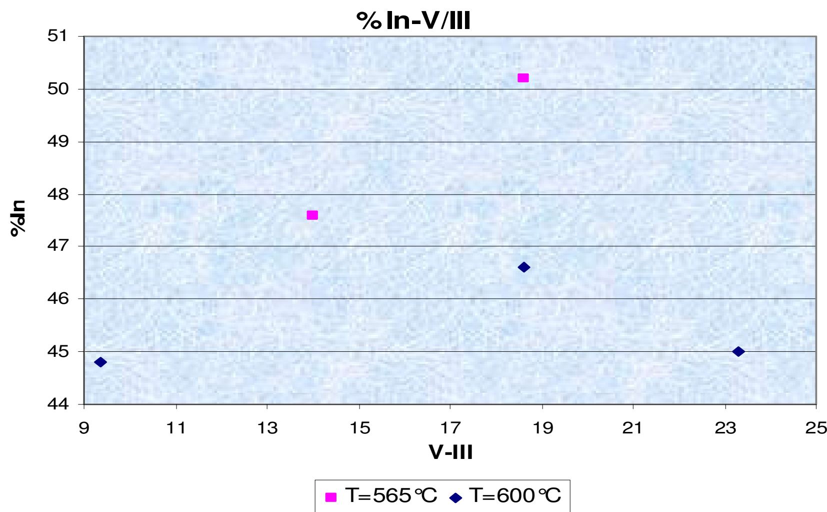

Fig.5.3: Indium percentage in InGaP, measured by HRXRD, versus V-III ratio.

It is clear that the Indium incorporation in InGaP is damped at higher temperatures, probably due to the higher pyrolysis temperature of TMIn in comparison with TMGa or to a desorption phenomenon of indium at high temperatures.

Instead, observing the picture, it can be noticed that the best conditions to reach a lattice match are V/III ratios around 20; lower values modify the stoichiometry, inhibiting Indium incorporation.

Another aspect amply studied and observable from the listed values in table 5.1 is the presence of a background doping in unintentional doped layers. The InGaP/GaAs system, more than in the GaAs case, is characterized by an intrinsic background doping, which, if not controlled, can deteriorate the devices quality. In our case there is an evidence of background impurities which origin acceptor energy levels, with concentrations around $10^{16}cm^{-3}$.

At a preliminary level, the available information suggests that these acceptor levels are introduced by Carbon, coming from thermal dissociation of the metal-organic precursors, during growth.

The InGaP/GaAs layers were studied also in their structural properties, using HRXRD (high resolution X-ray diffraction); the analysis was performed at the IMEM-CNR in Parma by Drs C.Bocchi and F.Germini. In general, a good structural quality of the grown layers was observed, when the match conditions were approached, with no secondary phases present and a narrow peak of few arcsec.

In picture 5.5, the case of an InGaP/GaAs sample with an Indium concentration of 46.6% is shown. The concentration profile results constant, while the secondary peaks oscillations can be attributed to the presence of the GaAs cap layer.

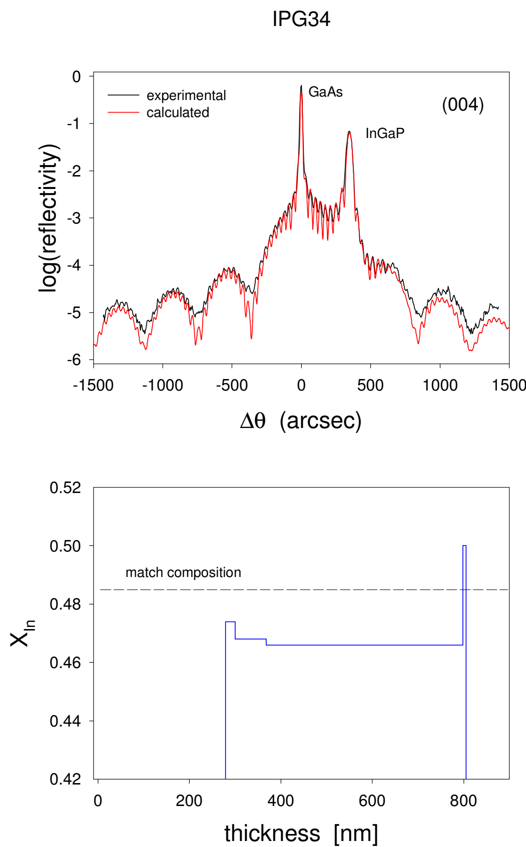

Fig.5.4: a) HRXRD spectrum of an InGaP with In:46.6% b) Derived concentration profile

Looking at the Photoluminescence (PL) spectra, in fig.5.5, obtained at 10 K from InGaP layers with different Indium concentrations, it is evident, in each of them, a mean peak probably linked to the band-band transition, namely to the Energy gap of the material.
Indeed, as expected, this peak moves toward lower energies, by increasing the Indium concentration. The full width at half maximum of the peak changes between 10 and 15 meV, when the Indium concentration is around the match value or a little lower, showing therefore a very good crystalline quality, comparable with the best InGaP materials in literature [5.2]. A different situation is instead present for Indium concentrations over 50%, for which the crystalline quality and the purity of the grown layers are lower, the peak full width at half maximum being around 25-30 meV. In some cases, like in samples A-D in the picture, the presence of further emissions at lower energies is observed. These latter peaks are probably due to impurities in the lattice. The spikes visible at 1.96 eV are an experimental artefact, introduced by the reference laser He-Ne used in the Transformed Fourier PL system.

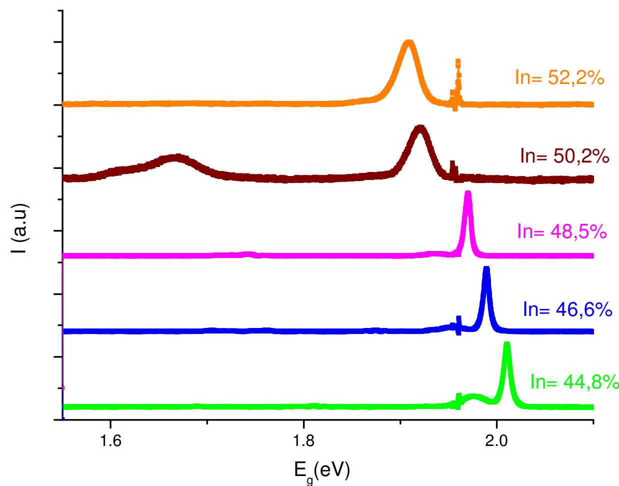

Fig.5.5: PL spectra at 10 K for InGaP with different Indium concentrations.

Beyond the possibility to give information about the Indium content in the material and its crystalline quality and purity, the PL spectra can be compared with electrical measurements, especially temperature dependent Hall effect mobility measurements.
Some of them are showed in Fig.5.6.
The curves (guides for the eye) of low temperature mobility, would evidence, in the B sample, a higher impurities concentration in comparison with the others A and C samples. This observation is also in agreement with the PL optical emission, that shows a higher peak width in the first case.

The doping resulting from Hall Effect measurements can be summarised as follows:

Sample A (In=50.2%; T=565°C,V/III=18,6): p=2.8X10^{16} cm^{-3}

Sample B (In=52.2%; T=550°C,V/III=14): p=1.9X10^{16} cm^{-3}

Sample C (In=47.6%; T=565°C,V/III=14): p=2.4X10^{16} cm^{-3}

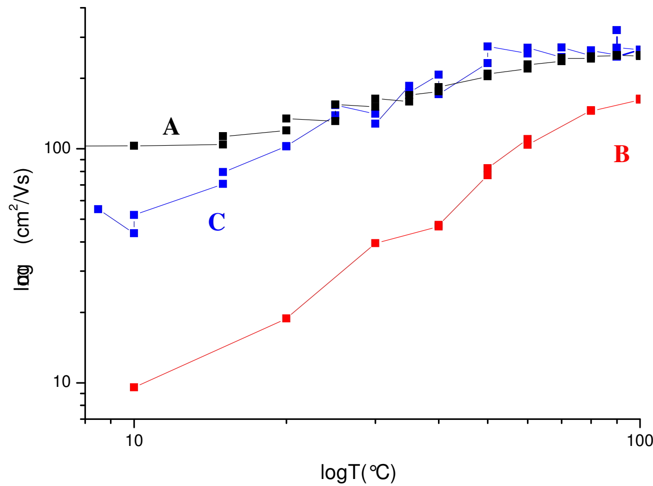

Fig.5.6: Mobility vs logT for 3 different InGaP samples.

5.4 Silicon doping

After the systematic study on unintentionally doped InGaP samples and the achievement of the best conditions for what concerns lattice match and background impurity minimization, we were able to face the growth of intentionally doped InGaP/GaAs samples, with different n type doping conditions. The n type doping was obtained from Silicon, supplied by the unique gas precursor in the equipment of the MOVPE-SEMLABS, Disilane, Si_2H_6. Our aim was to realize a series of InGaP samples, differently doped, to study the Iron ion incorporation and activation, subsequently introduced by ion implantation into the layers.

The grown samples were analyzed by Hall effect, CV or ECV (Etching Capacitance Voltage) measurements, to verify, in the first case, the effective doping with respect to the nominal values; in the second, also the doping profile changing the depth of the grown layer. As shown in the table below, layers with n doping concentrations between 5x10^{16} cm^{-3} and 10^{19} cm^{-3} were obtained.

Moreover, the linear dependence between supplied Disilan fluxes and free electron concentrations measured by Hall Effect analysis was verified.

Sample	X_{Si}/III Ratio in vapour phase	Conc. n (cm^{-3})	Mob. @RT (cm^2/Vs)	Res. (Ω*cm)	Thickness (μm)	Growth Temp.(°C)	V/III Ratio
IGPDOP1	$1.8*10^{-5}$	$5.9-6*10^{16}$	(1790)	($9.8*10^{-2}$)	1	600	15.6
IGPDOP3	$1.1*10^{-4}$	$7.8-9.3*10^{16}$ $8.2-9.7*10^{16}$	(1096)	($3.2*10^{-2}$)	1	600	15.6
IGPDOP4	$1.3*10^{-3}$	$7-5*10^{18}$	(483)	($3.1*10^{-3}$)	0.5	600	15.6
IGPDOP8	$2.1*10^{-3}$	$1*10^{19}$ (nom.)	-	-	1.2	600	15.6
IGPDOP9	$3.8*10^{-3}$	$3.5*10^{19}$ (nom.)	-	-	1.2	600	15.6
IGPDOP10	$4.97*10^{-5}$	$2.2*10^{16}$ (ECV)	-	-	1.0	600	14
IGPDOP12	$1.7*10^{-3}$	$5*10^{18}$ (ECV)	-	-	1.0	600	14
IGPDOP13	$3.6*10^{-4}$	$5.3*10^{17}$ (nom.)	-	-	1.0	600	14

Tab.5.2: Growth Parameters and properties of n-doped InGaP layers

In the development of this PhD activity, we considered useful to activate an ECV-Polaron system, with the purpose to investigate the doping profile and check the depth homogeneity of the InGaP layers (a work in collaboration with Dr. N.Del Monte, Ingegneria dell'Informazione and Dr R.Mosca, IMEM-CNR Parma). This technique provides information not easily available in the case of conventional Hall Effect or CV techniques and the results can be put in comparison to what obtained with these other methods. The system was tested for GaAs and InGaP layers. In fig.5.7 we show an example: the doping profile along the depth of an InGaP layer, 1 μm thick, and with an n doping level measured with Hall effect around $10^{18}cm^{-3}$.

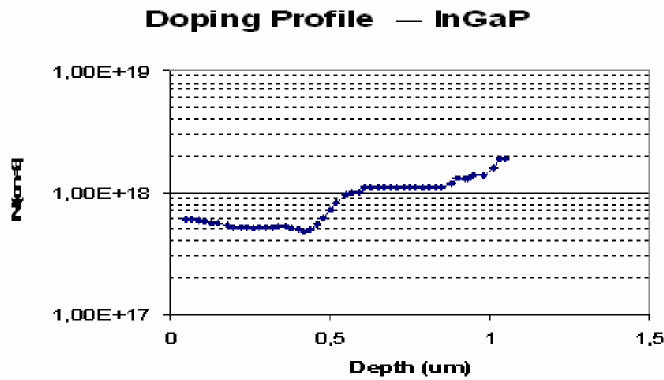

Fig.5.7: ECV Doping profile on InGaP.

As observable in Fig. 5.7, the doping concentration profile of Silicon in the samples turns to be non homogeneous along the depth and we obtained lower values (5-6x$10^{17}$$cm^{-3}$) than expected (10^{18} cm^{-3}) in the first 500 nm. Only beyond this threshold, the doping reaches concentrations around the values measured by Hall effect. The coupling of these two techniques could allow us to improve the Silicon incorporation control in InGaP and to realize undoped and doped samples with the features requested by the project.

5.5 Study of InP and InGaP layers Implanted with Iron

The activity that we will describe in the next chapters sets its basis on a previous study, about the implantation and damage recover in iron implanted InP and InGaP. The comparison between these two material classes concerning in particular RBS spectra in channelling conditions (minimum signal), is useful to study the effectiveness of damage recovering and the concentration profiles of implanted Iron (SIMS analysis). The previously studied InP was a bulk material obtained by Czochralski, while InGaP was a MOVPE deposited layer on GaAs.

Here we report a RBS spectrum to compare InP and InGaP behaviours after implantation [5.3-5.4], that can be described as follows.

In the InGaP RBS spectrum (shown in fig. 5.8), around 1600 keV, a peak due to the presence of Gallium on the surface is evident. Around 1250 keV, instead, the P-related signal, observable in InP, is obscured by the Indium presence, that exhausting forms a minimum under 1200 keV, in correspondence to the substrate, where an As peak at 1025 keV appears.

Observing the different behaviour of the two materials, after dynamic annealing (annealing at 220°C performed during implantation) we can note that for InGaP the RBS background signal is higher, as expected for a more damaged material. This effect can be due to the Gallium displacement, being Gallium lighter than Indium and Phosphorous. If we then analyze the right side of the spectrum, we can note two anomalous peaks, related to defects created after implantation. This last affirmation is deduced from backscattered ion energy, impact section of the matrix elements and the matrix density. It is indeed possible to derive the defective zones depth: the first is placed at 71 nm, the second at 126 nm from the surface, both around the expected depth for implanted iron. Therefore, while in previous studies on InP a complete recovering after implantation was observed, in InGaP they persist.

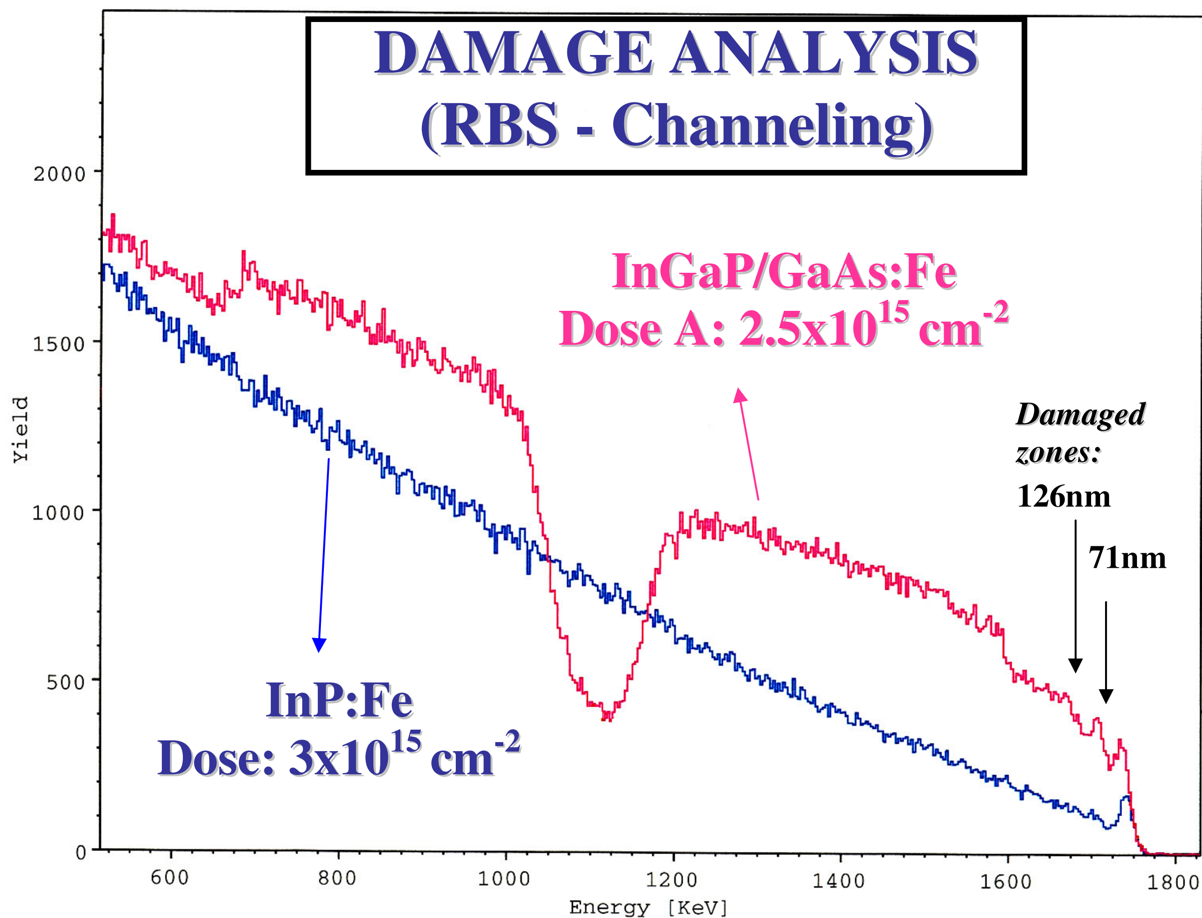

Fig.5.8: RBS spectra of InGaP and InP implanted with dynamic annealing.

In the InGaP case it is indispensable to perform thermal treatments, in order to recover as much as possible the damage caused by implantation.

In picture 5.9, the RBS spectra of thermally treated samples after implantation are shown.
The samples, annealed using different conditions, are compared with the "as-implanted" ones (namely implanted samples for which no thermal processes was performed after implantation, but only submitted to dynamic annealing).
The samples that have undergone thermal treatments at 600°C (for 60 minutes and with a P overpressure, necessary to avoid evaporation of the more volatile V element, that occurs at 400°C) show an optimum damage recover, as it was observed on InP. The samples implanted with different doses ($2.5X10^{15}cm^{-3}$ and $5X10^{14}$ cm^{-3}) present a damage recover even better than InP samples. The sample IGP1Aa, implanted with the highest dose, recovers its primary damage at 71 nm, but the extended defects connected peak, located at 125 nm from the surface, persists also if damped. In samples with the lowest doses, instead also after the first thermal treatment, in "as-implanted" conditions, both the primary and extended defects peaks are not present and the RBS background signal is sensitivity inferior to that of more elevated doses.
This means that dynamic annealing, performed at 220°C at these doses, is already capable of avoiding complex defect formations. A further annealing reduces even more the background RBS signal, leading to even lower values than in the case of not implanted samples.

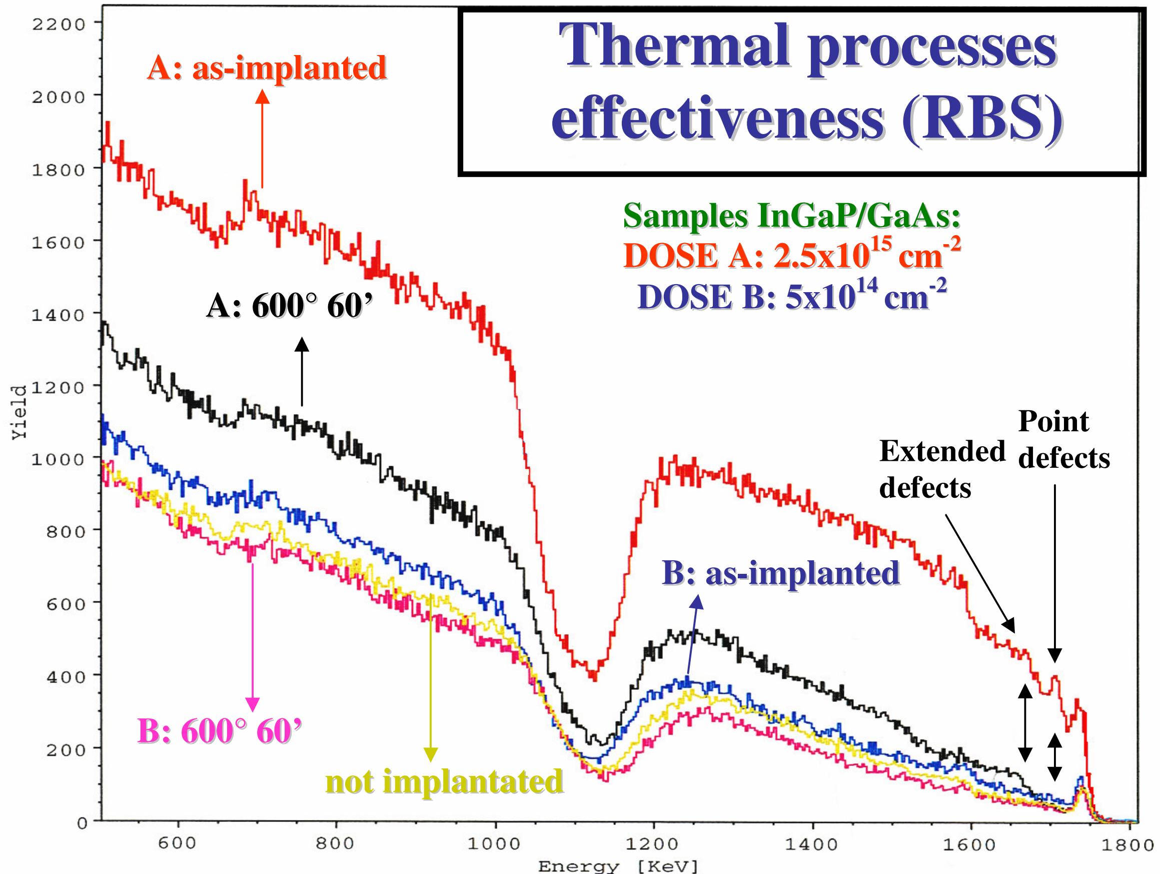

Fig.5.9: RBS spectra of InGaP after annealing

Further analysis on thermal treated samples was performed by SIMS, in the way to study the implanted Iron profiles.

In as-implanted InGaP samples the Iron distribution is very similar to the ideal case, for which a Gaussian curve is expected, where the maximum concentration reaches, in the best cases, also $10^{20}cm^{-3}$, neatly overcoming the solid solubility limit.

After thermal processes, the Iron concentration profile undergoes important modifications. Some effects like Iron diffusion out from the implanted regions can be observed. A migration regards the entire implantation profile and an accumulation is evident in the most defective zones. As it can be observed in the following pictures, in comparison with as-implanted samples, a peak decreasing occurs. Anyway, the concentration peak overcomes $10^{19}cm^{-3}$, and two accumulation regions are present, where the RBS spectra previously exhibited most defective zones.

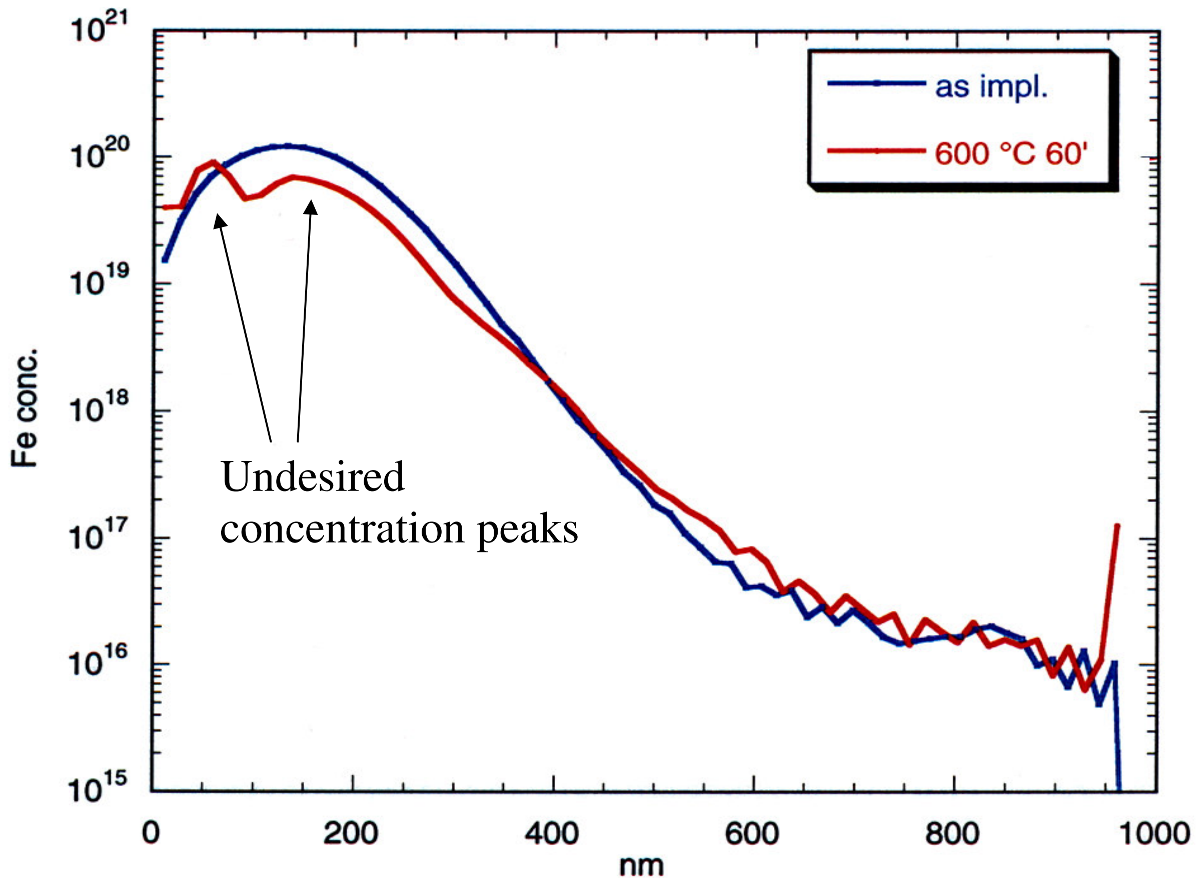

Fig.5.10: SIMS profiles of InGaP before and after annealing.

5.5.1 Electrical measurements

Thanks to the progressive improvement of the InGaP layer deposition, as previously mentioned, we obtained several samples grown under different conditions, suitable for further implantation studies. In this way, we were able to carry out some other works about Iron implantation in n-doped InGaP, especially investigating the effective role of Iron in realizing semi-insulating regions.

The materials underwent dynamic annealing and subsequently thermal processes, in the way to recover damage. Heavily silicon doped, n-type InGaP layers were grown matched with a GaAs n+ (100) substrate by MOVPE. In particular, InGaP/GaAs structures, composed by a 1 μm thick layer, with a free electron concentration of $6X10^{18}cm^{-3}$ and a mobility of 483 cm^2/Vs, were analyzed.

The samples were implanted using iron ions, in a process performed at 220°C, 190 keV and with an ion dose of $1.5X10^{15}$ Fe/cm^2 (at the laboratories of Legnaro Pd, by the workgroup of Prof. Gasparotto). Different thermal processes were performed at 450°C and 600°C, in Nitrogen atmosphere and Phosphorous overpressure, for 60 minutes.

Some electrical measurements, particularly current-voltage, were carried on (at the University of Bologna by Dr. Beatrice Fraboni) in order to analyze the change in electrical properties provided by ion implantation. In this way, it was possible to check the effective electrical compensation and to localize the introduced energy levels [5.5].

Therefore, measurements were performed at different temperatures, from room temperature to 200°C, using vertical injection in mesa structures. The samples were pre-treated by depositing an AuGe layer, 50 μm thick, on circular mesa structures (diameter of 100 μm) to realize ohmic contacts. On the substrate side of the sample, large area contacts were realized.

The J-V curves measured at room temperature demonstrate the reliability of implantation in realizing semi-insulating zones, since, as shown in graph 5.11, while the not implanted sample presents an ohmic trend and a low resistivity under any bias voltage, the implanted ones are characterized by a linear behaviour only at low bias while the conductivity lowers up to 9 order in magnitude. Consequently the J/V curves take place a more complex curve, typical of a semi-insulating material.

In particular, the two InGaP implanted curves are composed by two regions: an ohmic region, linear, and a quadratic region, related to the SCLC (space carriers limited current). These features are attributed to a semi-insulating material, where the presence of deep levels leads to the capture of free electrons introduced by silicon n-doping. Moreover, we can see how, in the case of annealing at 600°C, the compensation effect is stronger than for an annealing at 450°C indicating that the first

solution is the most effective in providing the necessary energy to allocate Fe atoms in substitutional positions.

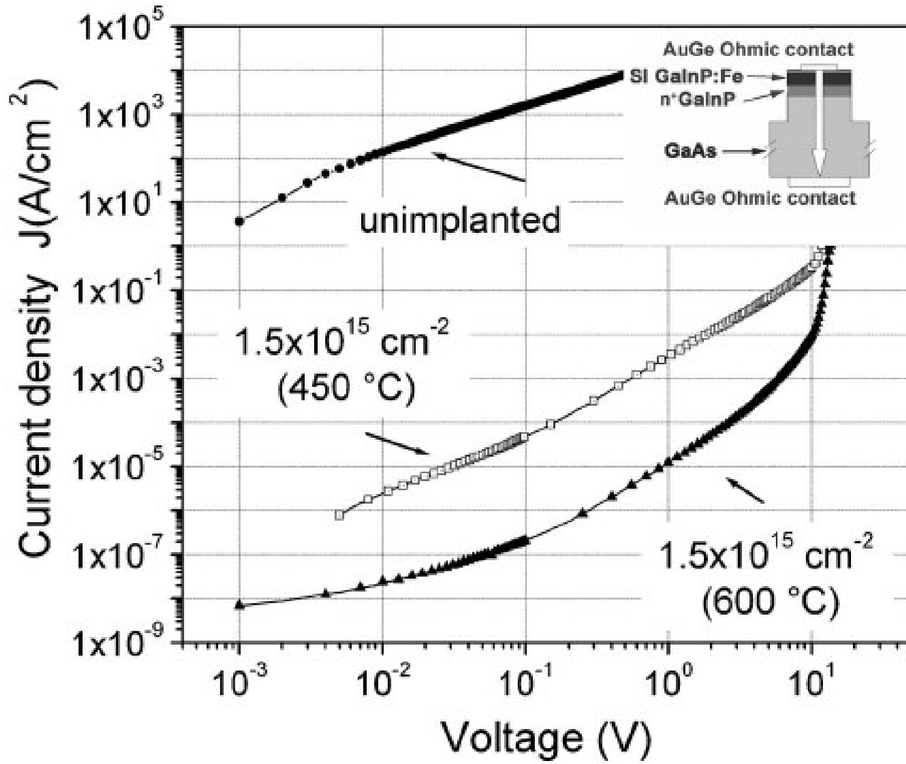

Fig.5.11: Current density vs. Voltage characteristics of the unimplanted InGaP sample in comparison with implanted ones, after a 450°C annealing and after a 600°C annealing

To better study the compensation effect and the different introduced energy levels, J/V at different T were carried out. An Arrhenius plot on the same samples (J/T^2 vs 1/T) was obtained. As it can be noticed (fig.5.12) in the case of a treatment at 450°C in ohmic regime and SCLC, the same activation energy is measured, therefore we conclude that the sample is extrinsic, because the transport is dominated only by one type of carriers, namely the majority ones, donors in this case.

This argument is consistent with the Schmidlin-Roberts model [5.6-5.7], according to which in the ohmic regime, for a not extrinsic semiconductor, the activation energy should be:

$$E_{\Omega} = (E_C - E_D) + \frac{1}{2}\left[(E_C - E_A) - (E_C - E_D)\right] \tag{5.1}$$

So that both an acceptor and a donor contribution would appear.

In this case, the increasing in resistivity is not due to a deep acceptor level activation, but probably induced by electronic traps formed because of the damage caused by implantation process.

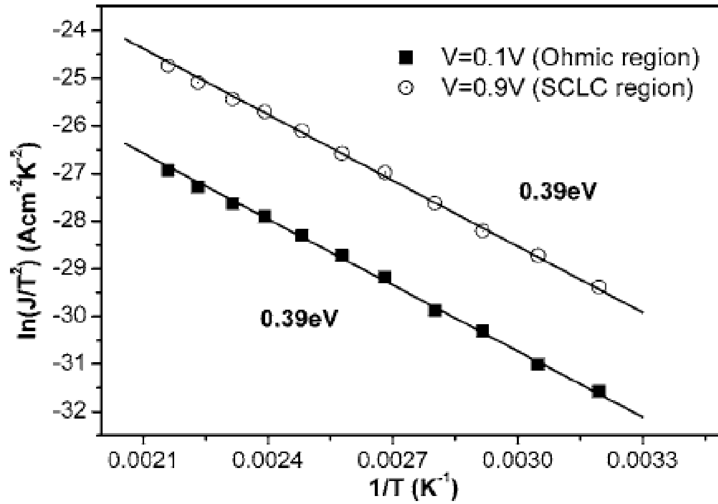

Fig.5.12: Arrhenius plot of an InGaP sample after annealing at 450°C.

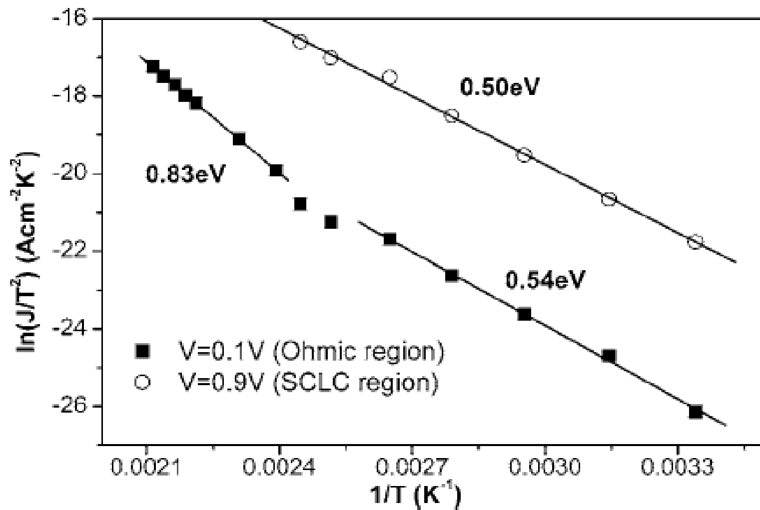

Fig.5.13: Arrhenius plot of an InGaP sample after annealing at 600°C

The situation is different when the sample is annealed at 600°C (Fig.5.13), in which case, as already seen, a complete recover occurs. This time, different activation energies are observed evidencing the compensation, due to combined effects of a deep donor and a deep acceptor.

In SCLC it was possible to localize a donor trap, which is placed at Ec-0.50 eV.

Instead, in ohmic regime two slopes can be observed, connected to different acceptors.

Inserting the energy activations obtained by the Schmidlin-Roberts model, we can derive two acceptor levels, at Ev+1.3eV and at Ev+0.72 eV.

These are active at different temperatures regime, as described in the following picture Fig.5.14 and they control, together with a deep donor, the material compensation.

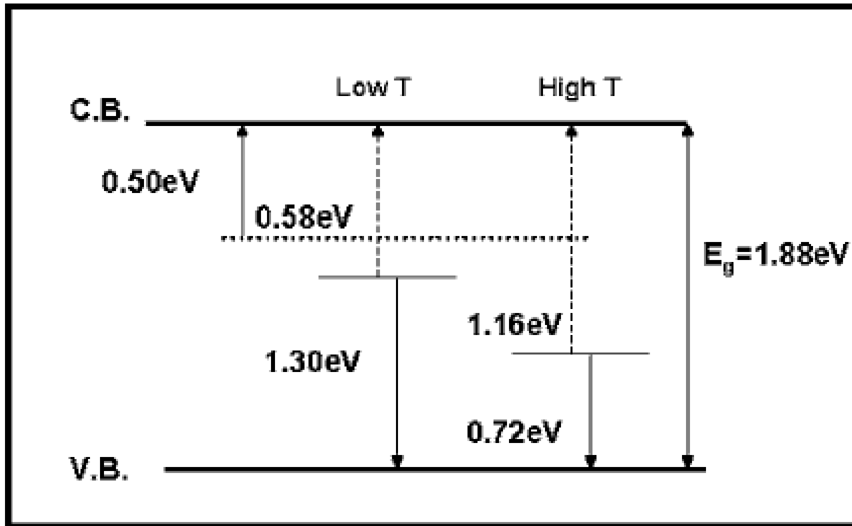

Fig.5.14: Different energy levels in the 600°C annealing case.

Putting these results in comparison with DLTS analysis (Fig.5.15) we can conclude that the Ev+0.72 eV level is related to acceptor centres introduced by Fe^{2+}, and it is the only one that can be correlated to the energy activation of implanted iron. As already seen, it can be detected only at higher temperatures, its level being very deep in the gap. The others levels can be ascribed to damages induced by implantation or already present defects in the as-grown InGaP n+ layers.

The Fe^{2+} level results anyway predominant with respect to the other Ev+1,30 eV. Therefore, the Iron role in conditioning InGaP implanted electrical properties, after thermal processes at 600°C, is confirmed.

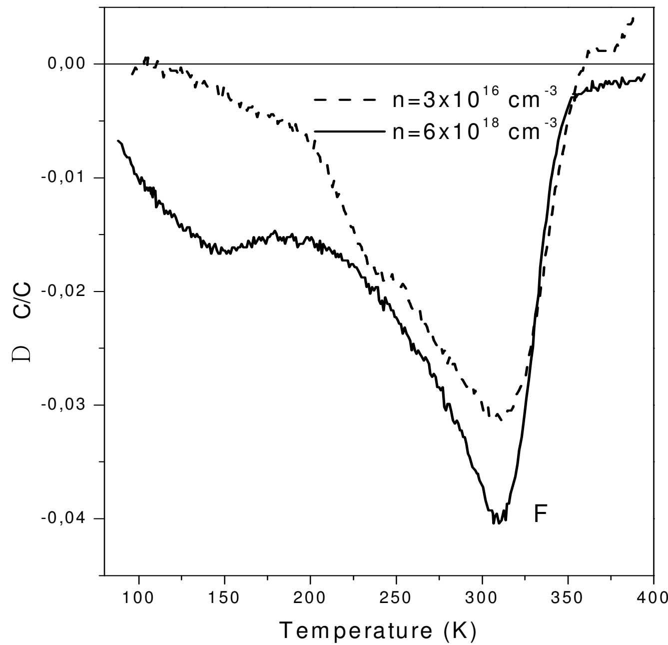

Fig.5.15: ODLTS spectra under illumination on InGaP:Fe implanted with different Si-doping.

The ODLTS spectra [5.8], measured under a λ=670 nm illumination, were obtained from differently doped InGaP samples (n=$3X10^{16}cm^{-3}$ and n=$6X10^{18}cm^{-3}$), but implanted at the same Fe dose ($2X10^{15}cm^{-2}$), the same implantation energy and both treated at 600°C with a post-implanted annealing.

As shown in the picture, a dominant peak with a 0.74 eV energy can be attributed to acceptors traps, provided in InGaP by the introduced $Fe^{2+/3+}$ species. Therefore, through this measurement, a direct confirmation of deep levels formation due to Iron implantation was obtained.

5.5.2 Structural analysis

Some SIMS profiles for implanted Iron concentrations were measured, at the University of Padova (at the workgroup of Prof. Andrea Gasparotto), to study the implanted species distribution after thermal processes. To this purpose, a Cs^+ primary beam was used, with an energy of 5.5 keV and $FeCs^+$ specie as secondary ions [5.8].

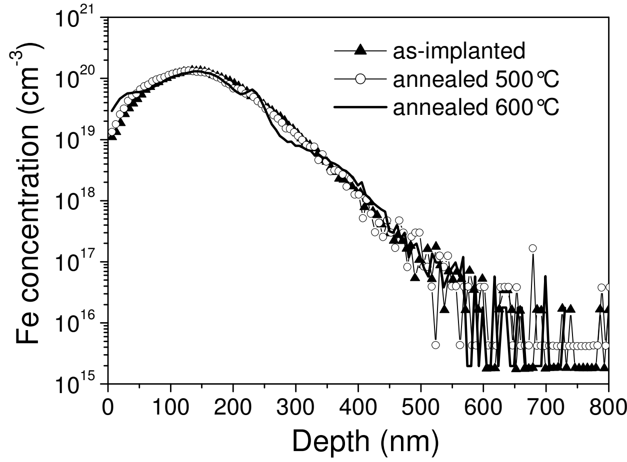

Fig.5.16: SIMS profile of implanted InGaP after different annealing treatments.

The concentration profiles, shown in figure 5.16, evidence an R_p (projected range) depth of maximum peak around 150 nm and a peak width around 300 nm. Differently from the previous cases, a particular redistribution of Iron does not occur after thermal treatments, neither at 500°C nor at 600°C. The annealed sample profiles are instead similar to the ones referred to the not implanted samples and the maximum ion concentration, over $10^{20}cm^{-3}$, remains practically unchanged. In this case there is no presence of secondary not recoverable damages, which after annealing would appear as "gettering" centres for new introduced ions. Probably this is due to a better structural quality of the layers grown by MOVPE, after the previously mentioned systematic study.

Moreover, comparing the RBS signal related to the matrix atoms (Indium in this case) and PIXE signal, related to the k_α of Fe, measured in channelling conditions toward different crystallographic directions, it is possible to quantify the Iron atoms fraction in substitutional position (therefore electrically active) [5.9].

In particular: the RBS yield is the RBS signal of the matrix along a crystallographic axis, I_{matrix}, normalized to the random rotating configuration signal $I_{R.R}$.

$$\chi_{RBS} = \frac{I_{matrix}}{I_{R.R}} \qquad (5.2)$$

In the same way, the PIXE yield is

$$\chi_{PIXE} = \frac{I_{Solute}}{I_{R.R}} \qquad (5.3)$$

Where I_{solute} is the PIXE signal related to the introduced specie and $I_{R.R}$ the PIXE signal obtained in random rotating configuration.

And the A fraction of impurities along the channel is given by:

$$A = \frac{(1-\chi_{PIXE}^{\min})}{1-\chi_{RBS}^{\min}} \qquad (5.4)$$

If we analyze the results obtained performing PIXE spectra, we observe the Fe atom fraction along <100> as a function of temperature and for different doping levels but the same implantation conditions. They are shown in picture 5.17. A high-aligned Fe fraction is detected in both cases (from 0.9±0.2 for higher doping levels to 0.7±0.1 for lower ones), and a slight decreasing at higher temperatures, starting from 500°C.

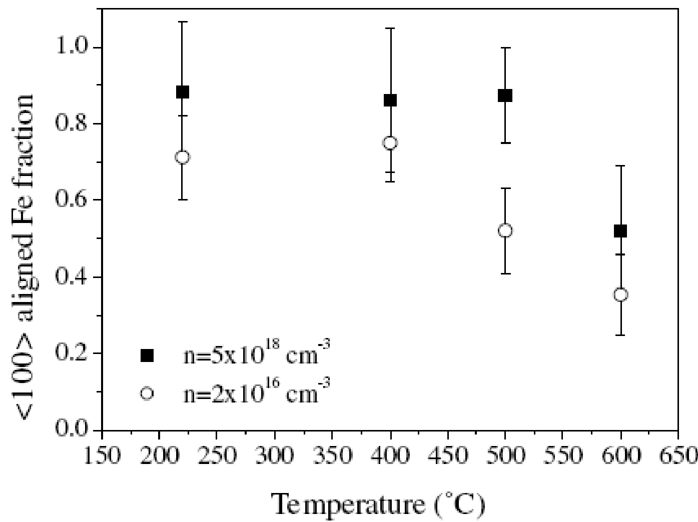

Fig.5.17: Substitutional Fe fraction measured by PIXE with different annealing temperatures

However, in the case of Zinc blend structures, these data are not enough to determine the atom substitutional fraction. The signal along the <100> direction does not discern indeed between substitutional Iron contribution and interstitial one.

To distinguish substitutional atoms from interstitial ones it is also necessary to operate an angular scansion along <110> (a direction in which it is possible to detect the tetrahedral sites that

otherwise would be aligned to substitutional ones) and to subtract this contribution to the <100> yield.

The two RBS and PIXE contributions, obtained in the channelling <110> direction, are shown in Fig. 5.18 . An as-implanted sample and another that underwent a thermal annealing are shown.

As it can be noticed, the PIXE signal follows more or less the RBS trend, referred to the matrix atoms, indicating the absence of tetrahedral interstitial sites. The Iron atomic fraction, previously calculated by a PIXE spectrum along the <100> direction, is therefore only due to substitutional atoms.

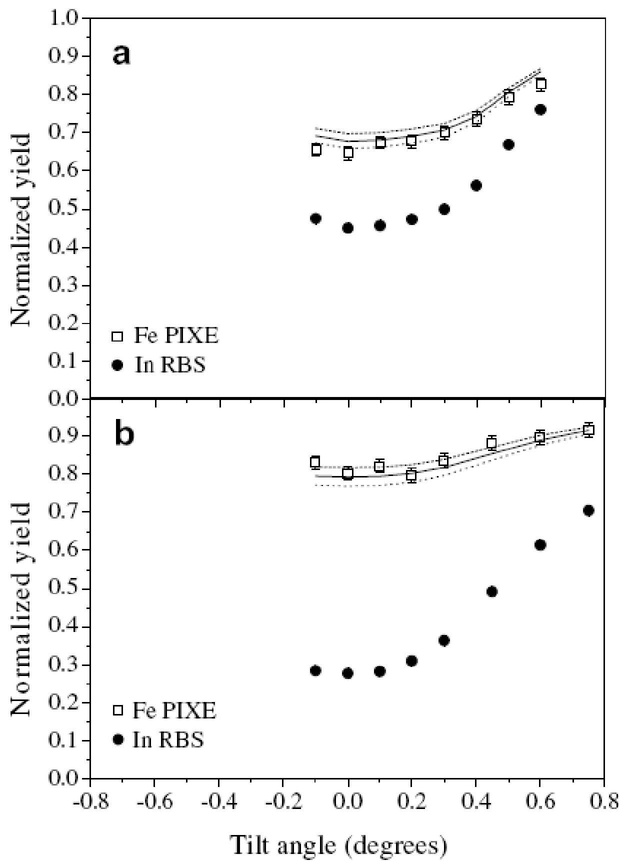

Fig.5.18: PIXE and RBS spectra in rotating random set to discern interstitial sites.

Comparing the obtained results with previous studies, performed on Iron implantation into InP matrixes, a high Fe substitutional fraction is observed in InGaP, as well as a higher thermal stability.

In the case of InP, in fact, after an annealing at 600°C, the Iron fraction was only 10%, [5.10-5.11-3.4] while in the present case it can reach 50%.

This can be interpreted arguing that the energetic substitutional Fe configuration is more stable in InGaP than in InP, or that it is related to the presence of defects with lower mobility.

Moreover, observing the picture in Fig.5.17, we see that for the previously high n-doped sample, at $n=5X10^{18}cm^{-3}$, substitutional Fe is more stable than in the lower n-doping case, at $n=2X10^{16}cm^{-3}$. Some other experimental analysis is now on progress to determine which of the hypothesis is more consistent.

5.6 Conclusions

By performing Iron implantation on differently doped InGaP samples and studying them through electrical and structural analysis, we argued that:

- InGaP grown by MOVPE is exposed to a higher structural damage from implantation than InP grown by melt;
- An annealing at 600°C on implanted InGaP can entirely remove the damage, so that annealing is the most suitable treatment for this kind of structures;
- By annealing at 600°C it is possible to activate Iron, in the way to realize semi-insulating regions through the introduction of deep energy levels;
- Substitutional Fe is more stable in InGaP (50% at 600°C) than in InP (10% at 600°C);
- The Iron substitutional fraction in InGaP is higher for highly n-doped samples.

References V

[5.1] Ingrey S., J.Vac.Technol., 4,(A10), pag.829,1992

[5.2] X.Z. Shang Solid State Communications, Vol. 138, Issue 3, pp.114-117 (2006)

[5.3] S.Rampino "Crescita epitassiale (MOVPE) di materiali a base di InP e studio degli effetti dell'impiantazione ionica di Fe" Tesi in Scienza e Tecnologia dei Materiali, Università degli Studi di Parma (2004)

[5.4] T.Cesca, A. Gasparotto, A.Verna, B.Fraboni, G.Impellizzeri, F.Priolo, L.Tarricone, M.Longo, "Incorporation of active Fe impurities in GaInP by high temperature ion implantation" Nucl. Instrum. Meth. B 242 653 (2006)

[5.5] "Deep levels controlling the electrical properties of Fe-implanted GaInP/GaAs" B. Fraboni, E. Piana, T. Cesca, A. Gasparotto, M. Longo ,R. Jakomin, L. Tarricone Appl. Phys. Lett. 90, 182106 (2007)

[5.6] F.WSchmidlin and G.G.Roberts, Phys.Rev.Lett.20,1173 (1968)

[5.7] G.G.Roberts F.W. Schmidlin, Physical Review Vol.180, Num.3 (1969)

[5.8] "Electrical and structural characterization of Fe implanted GaInP" B. Fraboni, T. Cesca, A. Gasparotto, G. Mattei, F. Boscherini, G.Impellizzeri, F.Priolo, R.Jakomin, M. Longo, L. Tarricone. Phisica B 401-402 (2007) 278-281.

[5.9] T. Cesca, A. Verna, G. Mattei, A. Gasparotto, B. Fraboni, F.Boscherini, M.Longo, L.Tarricone "Local structure of Fe incorporated in GaInP layers by high temperature ion implantation" Nucl. Instrum. Meth. B n. 257 p. 332 (2007)

[5.10] Cesca, A. Verna, G. Mattei, A. Gasparotto, B. Fraboni, G. Impellizzeri, and F. Priolo, Ion Beam Analyses and electrical characterization of substitutional Fe properties in Fe implanted InP Nucl. Instrum. Meth. B 249 894 (2006)

[5.11] T. Cesca, A. Verna, G. Mattei, A. Gasparotto, B.Fraboni, G. Impellizzeri, F. Priolo, Mechanisms for the activation of implanted Fe in InP J. Appl. Phys.100, 023539-023545 (2006)

Chapter 6

InP growth optimization and InP:Zn re-growth on Iron implanted InP

An important issue to set the implantation as a technological process step is to observe the interactions among the implanted species and other doping elements. The next activity derived from these motivations is centred on the study of Zinc doped InP, re-grown by MOVPE on iron implanted InP substrates (n-doped type). Iron in InP materials acts like deep electron trap, located at Ec-0.66eV [6.1-6.2-6.3]

As in the previous case, before the implantation study, the InP growth was optimized by a systematic study, starting from undoped layers and considering all the analysis techniques needed to control the deposition quality. In this case, after the Zn-doping optimization, the Zinc diffusion was studied, being an important effect that must be considered especially for applications in electronic devices. Then, the re-growth was finally performed and some preliminary evidences of Zinc-Iron inter-diffusion were obtained.

6.1 Homoepitaxial growth of InP/InP(001)

A systematic study on InP homoepitaxial growth by MOVPE was developed, to obtain Zn doped samples (p-doping) of good crystal quality and controlled doping. The aim was the study of Zn doped InP re-growth on InP previously implanted with Iron, with the chance to evaluate the diffusion of Zn and Fe, from the layer toward the substrate or from substrate to the layer respectively. The implanted InP substrates were S-doped (n-type), while the Iron implantation, as previously said, is expected to induce semi-insulating regions into heavily n- doped materials. We started from undoped InP layers, with the purpose to optimize the growth parameters, minimizing the background doping and achieving the best crystal properties. In table 6.1 we summarize the used deposition parameters, both for undoped- and Zn-doped InP.

Sample	Growth time (min)	Temp. (°C)	V/III Ratio	Doping Concentration	X_{Zn}/III ratio in vapour phase
IP1	30	600	21	U.D.	0
IP2	45	600	21	U.D.	0
IP3	75	600	21	U.D.	0
IP4	75	550	21	U.D.	0
IP5	75	550	21	U.D.	0
IP6	45	550	21	U.D.	0
IP7	45	600	21	U.D.	0
IP8	45	600	30	U.D.	0
IP9	45	550	30	U.D.	0
IP10	45	600	21 Half growth rate	U.D.	0
IP11	360	600	21	U.D. n= 8x10^{14} cm^{-3} (Hall)	0
IPDOP1	60	600	21	Zn	0.008
IPDOP2	60	600	21	Zn	0.186
IPDOP5	60	600	21	Zn	0.856
IPDOP6	60	600	21	Zn	1.457
IPDO7	60	550	21	Zn	1.457
IPDOP8	60	600	21	Zn	0.0025
IPDOP9	60	600	21	Zn	0.006
IPDOP11	60	600	21	Zn	0.003
IPDOP12	120	600	42.3	Zn	1.7

Tab.6.1: parameters and characteristics of undoped InP layers

With the goal to analyze the electrical properties of the grown InP, very thick layers were realized, (around 6 microns), in the way to obtain a not empty layer region, suitable for Hall effects measurements (the low background doping makes a really width depletion layer).

The electrical analysis performed by Hall measurements on such epitaxial layers, evidenced n-type conduction; in the picture 6.1 the behaviour of the electron concentration versus the reciprocal temperature is shown. Figures 6.2-6.3 show the mobility and the electrical resistivity as a function of temperature. The electron concentration at room temperature is around 8×10^{14} cm^{-3} and the mobility is around 3280 cm^2/Vsec. The mobility peak, at a temperature around 80-90 K, is about 12000 cm^2/Vsec. The measurement shows, for temperatures lower than RT, that the electrical transport properties are dominated by a relatively deep donor, E_d~40 meV, while at low temperatures a weak dependence of the n density on the temperature, could be attributed to a second hydrogenoid donor type level.

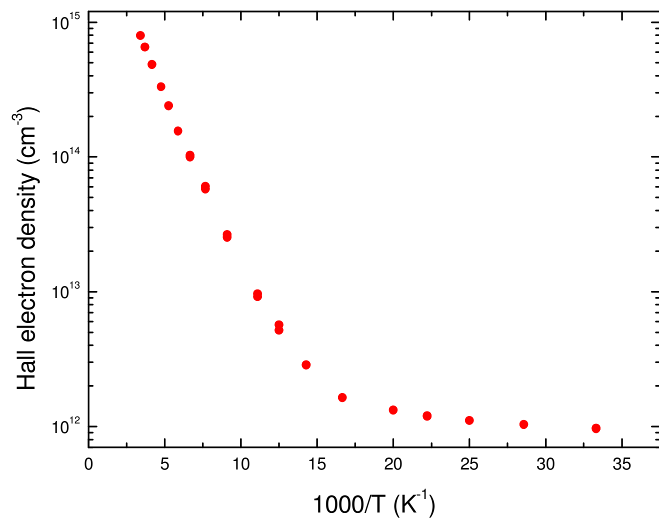

Fig 6.1: electron concentration versus 1000/T in an InP undoped layer

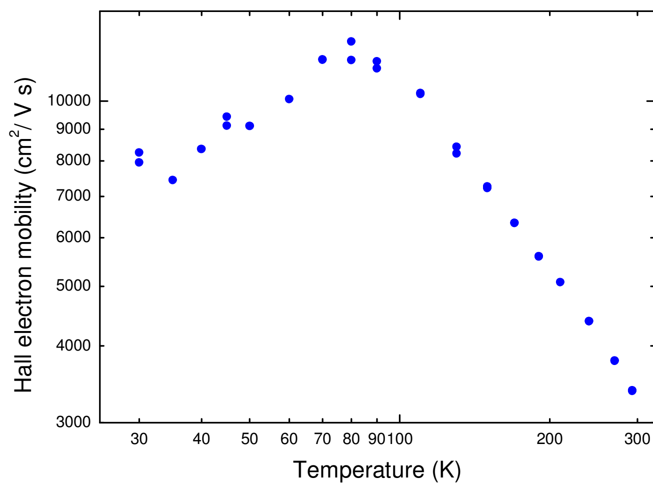

Fig 6.2: Hall mobility versus T in an InP undoped layer

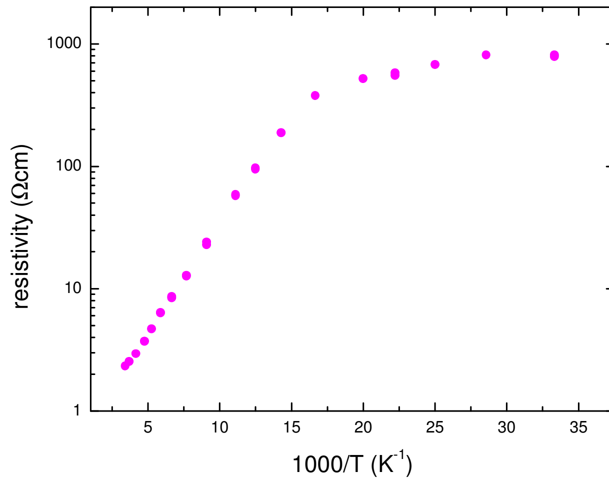

Fig 6.3: Resistivity versus 1000/T in an InP undoped layer.

6.2 Optimization of the Zn doping

Considering the case of InP:Zn layers, grown with different Zn quantities and thickness around 1-2 μm, through Hall effect measurements, we measured a hole density variable between 10^{15} and ~$5X10^{17}$ cm^{-3}. In the same samples, the SIMS profiles reveal a higher Zn atom density: lower is the layer doping more pronounced is this discrepancy. This feature can be attributed to a non uniform distribution of Zn in the layer depth and to the presence of non active Zn atoms (for example in interstitial sites). The emerged difficulty to achieve high concentrations doping has to be underlined, also providing high nominal doses during growth. Responsible of this aspect is the high mobility of Zn, which, beyond a certain concentration, tends to migrate, overflowing the layer and diffusing toward the substrate. This phenomenon will be better analyzed in the following paragraph. The values obtained through Hall Effect measurements are summarized in the following table, 6.2. The measurements were performed by using the Van der Pauw method.

Sample	Type	p concentration (cm^{-3})	Mobility (cm^2/V s)	Resistivity (Ohm cm)	Nominal thickness (nm)	X_{Zn}/III ratio in vapour phase
IPDOP1	p	$4,7 \times 10^{14}$	60	220	1500	0,008
IPDOP2	p	4.7×10^{16}	119	1,1	1000	0,187
IPDOP5	p	$2,2 \times 10^{17}$	140	0,2	1000	0,856
IPDOP6	p	$4,6 \times 10^{17}$	43	0,31	1000	1,457
IPDOP7	P	$1,350 \times 10^{17}$	150	0,33	1200	1,457
IPDOP9	p	$1,1 \times 10^{15}$	70	75	1000	0,006
IPDOP11	p	$4,5 \times 10^{14}$	26	542	1000	0,0003
IPDOP12	p	$2,1 \times 10^{16}$	56	5,2	1000	1,7
IP11/InP	n	$7,9 \times 10^{14}$	3280	2,3	6000	0
IP11/GaAs	n	$7,8 \times 10^{14}$	2215	3,6	6000	0

Tab. 6.2: Parameters and characteristics of Zn-doped InP

Some PL analysis was also carried out on the InP samples. In fig.6.4 we present, as an example, the FFT Photoluminescence spectrum of the IPDOP12 sample, performed at low temperature. This layer had a hole concentration of $p=2.1 \times 10^{16} cm^{-3}$.

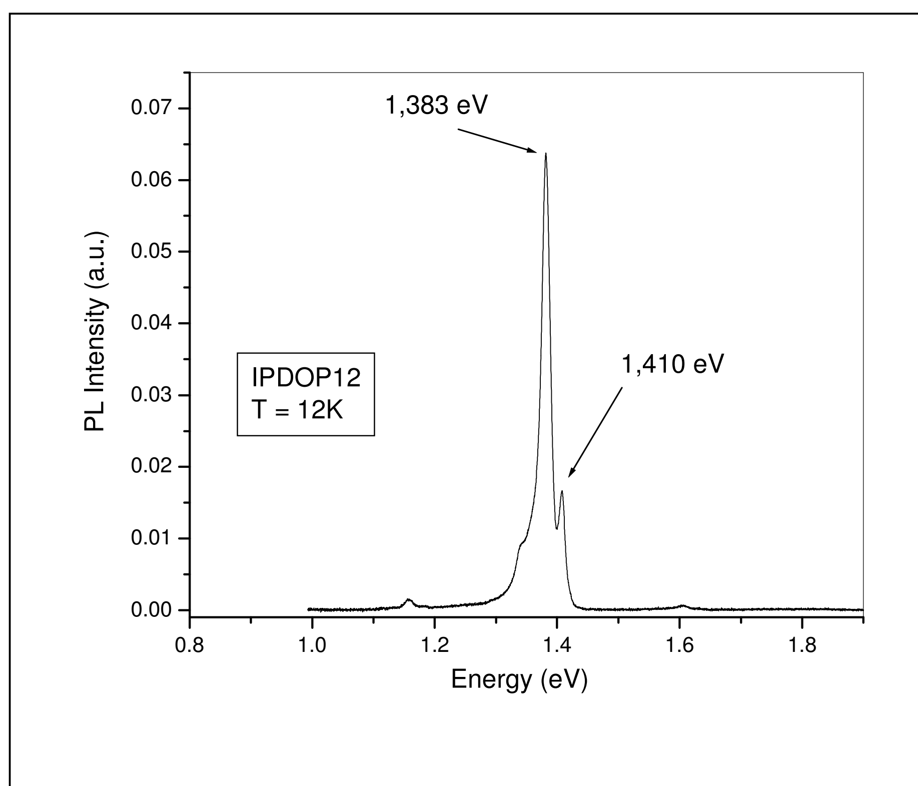

Fig.6.4: PL spectrum at 12 K of InP:Zn

Comparing the emissions spectrum with literature [6.4], the following attributions could be hypothesized:

- The 1.410 eV emission peak is related to a Zn acceptor bound exciton;
- The 1.383 eV emission peak is related to a band (or from shallow donor level) to an acceptor level;

It has to be considered the presence of excitons transitions that are a fingerprint of a good quality of the grown layers.

6.3 Study of the Zn diffusion

During a MOVPE growth of InP-based semiconductor materials, the unintentional Zn diffusion is certainly a relevant topic for technological applications. Indeed Zn, in this kind of materials, diffuses faster than n type dopants, tending to overflow in not desired regions, beyond a limited incorporation in the doped zones, thus inducing an efficiency reduction in junction devices.
The diffusion effect, as already reported [6.5-6.6-6.7-6.8-6.9], is triggered for Zn concentrations above $2X10^{17}$ cm^{-3}. We arrived to the same conclusion through SIMS analysis (Secondary Ion Mass Spectroscopy) on the IPDOP9 layer (Fig.6.5), deposited by using low Zn fluxes and showing a Zn concentration around $2\text{-}3X10^{17}$ cm^{-3} (the expected InP layer thickness is around 1 μm).

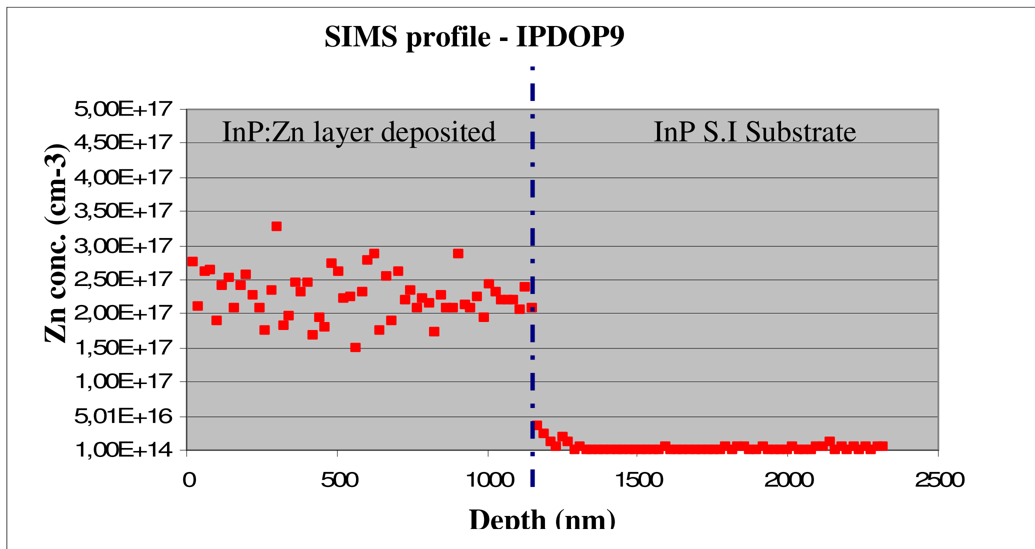

Fig.6.5: SIMS profile of a Zn doped layer, with Zn: $4X10^{17}$ cm^{-3}

In this case, a strongly limited diffusion is observed and Zn tends to stay into the layer instead of moving toward the substrate.

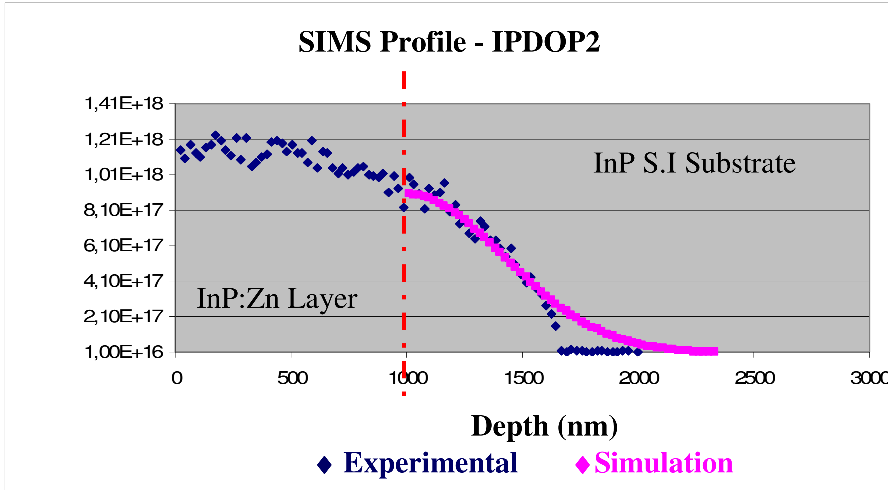

Fig. 6.6: SIMS profile of Zn doped InP, Zn:$1.2X10^{18}cm^{-3}$

The effect is different when the Zn concentration supplied during the growth goes above $10^{18}cm^{-3}$. In IPDOP2 (Fig.6.6), where the Zn concentration is measured to be around $2X10^{18}cm^{-3}$ and the expected thickness is again around 1 µm, the SIMS profile shows a strong diffusion and a Zn spreading beyond the layer border. A simulation was therefore performed (pink curve), calculated following a simplified model based on the second Fick's law. As it can be observed, it fits quite well the experimental result (blue curve).

The calculated concentration profile is based on:

$$N(x,t) = N_0 e^{\left[\frac{-(x^2}{4Dt})\right]} \quad (6.1)$$

Where the used parameters are: N_0, which is the front concentration from which the simulated profile begins, and D, which is the diffusion coefficient. In case of IPDOP9 sample they resulted:

$N_0 = 0,9*10^{18}\ cm^{-3}$

$D = 2,5*10^{-13}\ cm^2/s$

A confirmation of the good approximation of the used model is given by the fact that the calculated diffusion coefficient is comparable with the values present in literature [6.5]. Moreover, also

following the proposed model and in agreement with what observed in the mentioned paper, the diffusion coefficient increases by increasing the incorporated Zn concentration.

Another interesting aspect is that, so as in the illustrated case, also in the abovementioned work at a certain value of the flux of DMZn, a Zn saturation was observed. In particular, the authors [6.5] found a saturation concentration that corresponds to $2X10^{18}$ cm^{-3} for TMI fluxes of $1.88X10^{-5}$mol/min and $2.4X10^{18}$ cm^{-3} for $3.76X10^{-5}$ mol/min. These values are comparable with the results here obtained, for example a maximum concentration equal to $1.21X10^{18}$ cm^{-3}. In IPDOP5 (Fig.6.7), though the Zn flux was increased, the measured concentration did not increase, but the diffusion in the substrate is higher, giving a diffusion coefficient of $6X10^{-13}$ cm^2/s.

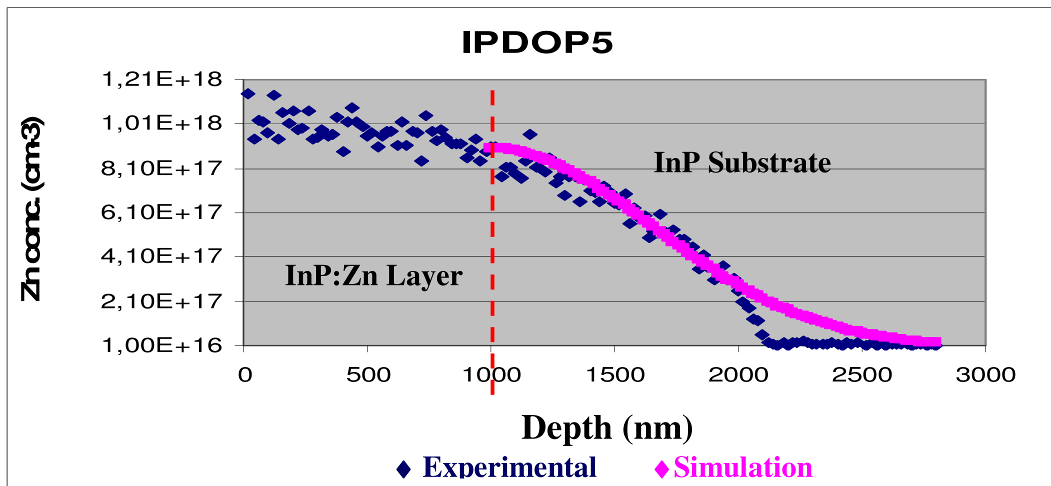

Fig. 6.7: SIMS profile of Zn doped InP

6.4 InP:Zn regrowth on InP substrates implanted with Iron

Over the last years, several works have been reported, regarding Iron implantation and its properties into InP materials [6.10-6.11]. The present work therefore leans its basis on this extended experience, but exploring in particular the diffusion effects between Zn and Fe, after MOVPE re-growth of InP:Zn on InP Fe implanted.

The different structures realized were:

InP:Zn/substrate InP:S

InP:Zn/substrate InP:S and Fe implanted

In Tab.6.3 the different kinds of used substrates and the Zn concentrations are reported.

Sample	**Substrate**	**Zn Conc.(cm^{-3}), meas. by SIMS**
IPDOP13/B	23HA0	$1x10^{17}$
IPDOP13/A	23HB0	$1x10^{17}$
IPDOP13/D	InP:S	$1x10^{17}$
IPDOP14/B	23HA0	$1x10^{18}$
IPDOP14/A	23HB0	$1x10^{18}$
IPDOP14/C	InP:S	$1x10^{18}$
IPDOP14/E	23HAa	$1x10^{18}$
IPDOP14/F	23HBa	$1x10^{18}$

Substrates:

InP substrate	**Fe implant (cm^{-2})**	**S doping (cm^{-3})**	**Annealing**
23HA0	$5x10^{14}$	$1x10^{17}$	-
23HB0	$5x10^{14}$	$1x10^{19}$	-
InP:S	No	$1x10^{19}$	-
23HAa	$5x10^{14}$	$1x10^{17}$	600°C, 60 min
23HBa	$5x10^{14}$	$1x10^{19}$	600°C, 60 min

Tab.6. 3: Different substrates used and Zn doping performed as re-growth

The first preliminary results to examine the influence between Zn and Fe, in the Zn diffusion and the Fe implanted distribution are obtained by SIMS measurement and presented in fig.6.8 and 6.9.

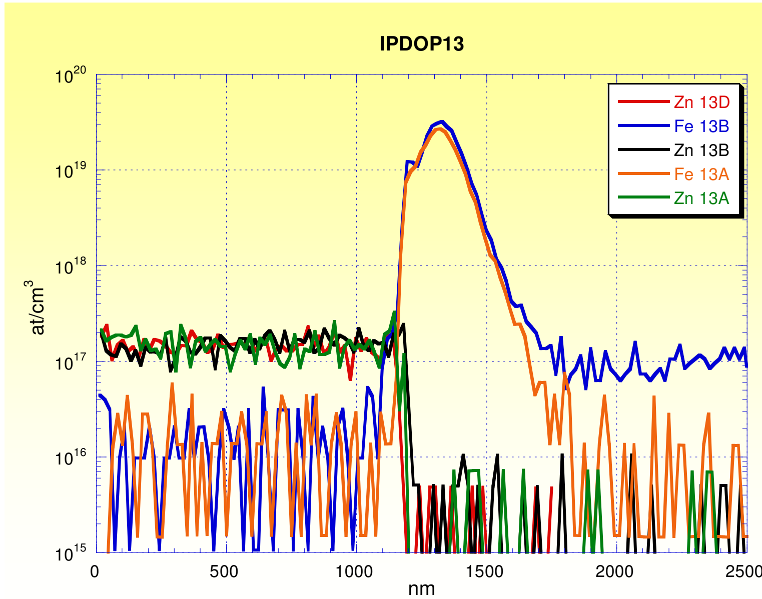

Fig.6.8: SIMS profile of InP:Zn (Zn:4X10^{17}cm^{-3}) regrown on Fe implanted InP

When the Zn concentration of the re-grown layer is low (Zn:4X10^{17}cm^{-3}), as in Fig 6.8, Zinc does not diffuse toward the substrate. Consequently, the Iron implanted peak keeps approximately unchanged.

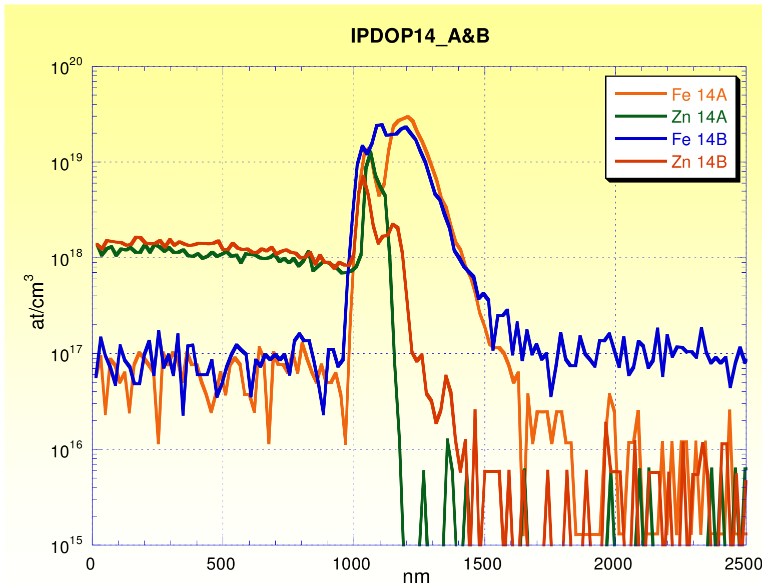

Fig.6.9: SIMS profile of InP:Zn (Zn~10^{18}cm^{-3}) regrown on Fe implanted InP

When the Zn concentration of the InP re-grown is higher (Zn~10^{18}cm^{-3}), as in fig.6.9, Zn diffuses into the substrate, as previously shown, and the Fe implanted peak shows a modification: it turns to be attenuated where Zinc is present.

On the other hand, the Zinc diffusion toward the substrate is blocked by the Iron implanted regions and Zinc remains confined in the area at 100-200 nm from the substrate surface, piling on this region (differently from the case in absence of Fe, where it diffuses for over 1000 nm as shown in Fig.6.7).

This is certainly a remarkable result since Iron could have a double effect in InP-based devices: first of all as a compensation element, by forming semi-insulating regions, but also by acting like a barrier for further Zn diffusion into the substrate, thus avoiding undesired effects for device fabrication.

References VI

[6.1] B.Fraboni, A.Gasparotto, T.Cesca, A.Verna, G.Impellizzeri, F.Priolo, Appl.Phys.Lett.87, 252113 (2005)

[6.2] S.J. Pearton, Mater. Sci. Rep. 4(1990) 313

[6.3] S.G.Bishop: S.Pantelides (Ed.), Deep centres in Semiconductors, Gordon and Breach, New York, 1986, p541

[6.4] Y. Moon, S. Si, E. Yoon and S. J. Kim, J. Appl. Phys. 83 (1998) 2261

[6.5] N. Otsuka et al., J. Appl. Phys., 84, 8 (1998)

[6.6] S. N. G Chu, R. A. Logan, M. Geva, and N. T. Ha J. Appl. Phys. 78, 3001 (1995)

[6.7] B.Tuck, Journal of Crystal Growth 208 (2000) 123-129

[6.8] Cheng-Yu Tai and M.Geva, 11th International Conference on InP and related materials, 16-20 May 1999, Davos, Schwitzerland

[6.9] C.Blaaw, J.Appl.Phys.66(2), 1989

[6.10] Gasparotto A., Carnera A., Scordilli A., Priolo F., Frigeri C., Rossetto G. Nucl.Inst.and Meth. In Phys.Res.B 96 (1995)307-310

[6.11] A. Gasparotto, A. Carnera, C. Frigeri, F. Priolo, B. Fraboni, A. Camporese and G. Rossetto J. Appl. Phys. 85 (1999), p. 753.

Chapter 7

InGaAs: Preliminary results

The aim to investigate iron implantation effects was extended also to InGaAs/InP, in the way to compare the previous studies on InGaP and InP, to this kind of material system. Though InGaAs/InP is a well-known structure, diffusely examined and used in several technological applications, this aspect has been less studied [7.1-7.2]. As for the previously illustrated cases, in this PhD work a systematic study of the growth was carried out. In this section, we present only preliminary results, concerning the properties of some grown layers.

7.1 Substrate treatment

InP (001) substrates (the typical size is a quarter of a 2 inches wafer) were cleaned before growth, following the sequent procedure: they were etched in a 5:1:1 H_2SO_4:H_2O_2:H_2O solution at room temperature and then rinsed in de-ionized water [7.3].
After that, they were dried through a pure nitrogen flux. The immediately formed fresh oxide layer was thermally removed in the MOVPE chamber, before deposition, in a few minutes at 600°C, under an overpressure of TBP must be used to prevent incongruent evaporation of the group V element.

7.2 Deposition of undoped InGaAs/InP layers

Once again, the study of Iron implantation in doped InGaAs layers requires an extensive growth analysis of undoped and doped InGaAs layers. For these reasons, several InGaAs layers on InP were deposited with different growth parameters. In order to achieve the lattice-match with the

Indium Phosphide substrate, the Indium content in the alloy must be of 53%, therefore $In_{0.53}Ga_{0.47}As$ has to be grown. Even in this case, the unintentional background doping has to be minimized.

The InGaAs epytaxial layers, nominally undoped, were 500 nm thick and were grown using different V/III ratios and growth temperatures, as illustrated in table 7.1.

Sample	**V/III**	**Growth Temp. (°C)**	**%In nom.**	**%In (from XRD)**
IGA1	21	600	53	46
IGA2	20	600	49	44.5
IGA3	21.2	600	45.6	43
IGA4	20.6	600	54.3	46.5
IGA5	34.3	600	54.3	< 48%
IGA6	6.9	600	54.3	< 48%
IGA7	20.6	550	54.3	< 48%
IGA8	20.6	650	54.3	N.D.
IGA9	21.9	600	63.6	N.D.
IGA10	21.9	600	63.6	80
IGA11	21.9	550	63.6	80
IGA12	21.9	500	63.6	63.5 – 65
IGA13	21.9	650	63.6	75
IGA14	22.2	500	56.7	67
IGA15	22.2	550	56.7	
IGA16	22.2	600	56.7	
IGA17	22.2	600	56.7	
IGA18 (different interface sequenze used InGaAs/InP)	22.2	600	56.7	

Tab. 7.1: Parameters and characteristics of the grown InGaAs layers

During this preliminary work some difficulties were found. They were related to the Indium incorporation control in the InGaAs alloy. It was hard to obtain the exact percentage needed for the complete lattice match and a large range of concentrations, between 47% and 73%, were obtained, as derived by HRXRD analysis (in Fig.7.1 and 7.2). In addition, higher growth temperatures turned out to influence the alloy composition; therefore a more detailed study of this aspect was carried out, through the deposition of layers grown at different temperatures.

Moreover, thanks to the choice of proper reagent sequences at the interfaces between InGaAs and InP, it was anyway possible to improve the conditions to achieve mirror like surfaces for the grown layers. In the following pictures we can see different XRD spectra, referred to different growth conditions. In the first cases, fig.7.1, an Indium concentration always lower than the required one

(53%) is evident, while in the case in fig.7.2, the excess of Indium, incorporated up to 75%, is shown.

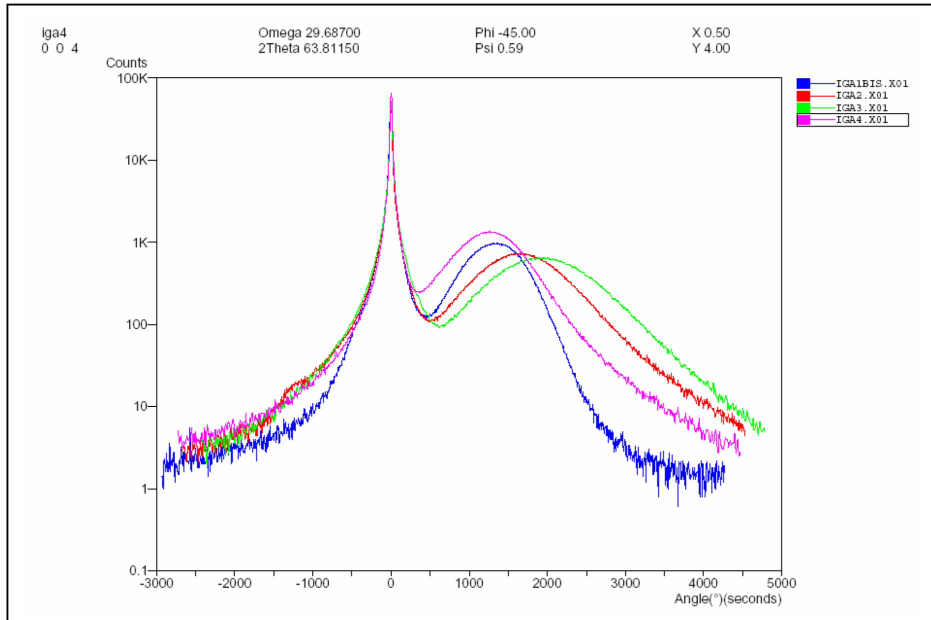

Fig.7.1: HXRD spectra for InGaAs/InP samples with In < 53%.

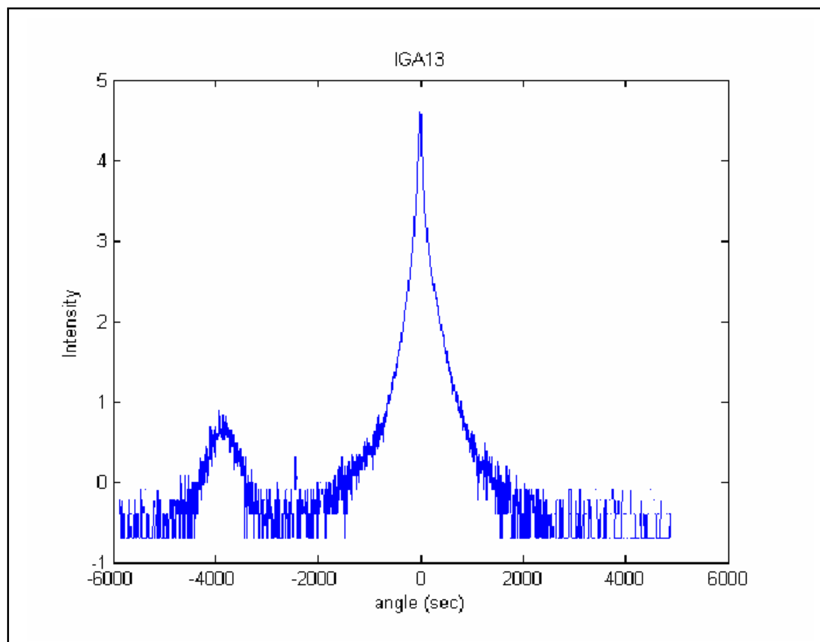

Fig. 7.2 HR-XRD spectrum for indium around 75%.

The PL spectrum in fig. 7.3, referred to a InGaAs/InP heterostructure with an Indium content lower than that required for lattice matching, points out however a fair optical quality, compared with

what observed in literature [7.4]. Though it represents a case of a pseudomorphic grown heterostructure, the FHWM is quite narrow, around 58 meV.

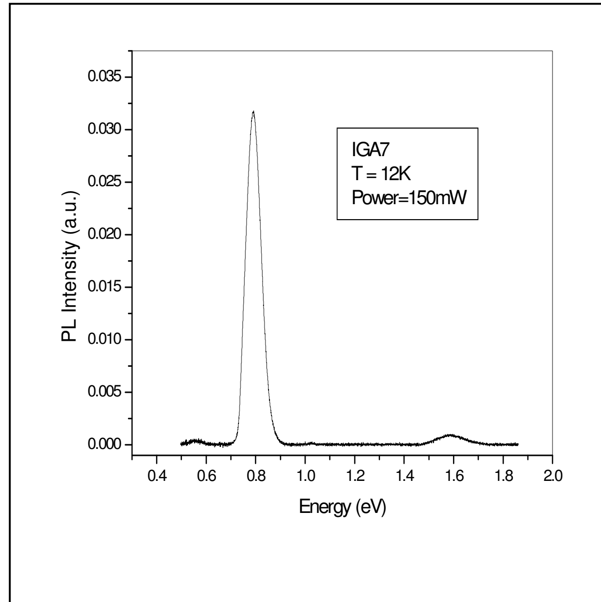

Fig. 7.3 PL spectrum at 12 K of a InGaAs layer; mean emission peak is at 0.792 eV (FWHM = 58 meV).

Then we focused on the electrical properties of the grown InGaAs layers, through Hall Effect measurements. The electrical conductivity of the unintentionally doped InGaAs layers resulted to be n type, with an electron density estimated (without depletion layer correction) of about 10^{16} cm^{-3} at room temperature. This background doping can be probably ascribed to Carbon, which in some conditions acts like donors in InGaAs layers [7.5-7.6].

In this case, the density values, measured at RT, vary in the range 0.6-4X10^{16} cm^{-3} (Fig.7.4a), with the mobility equal 800-1000 cm^2/Vs at RT (Fig 7.4b). In the best literature cases, we find higher mobilities (over 7000 cm^2/Vs) and lower background doping levels (around $10^{15}cm^{-3}$) [7.7]. Our values are probably connected with the lattice mismatch, since the optimization work is still in progress.

The temperature dependence of the electrical transport parameters (shown in Fig.7.4a) is very weak, typical of a quasi metallic behaviour, and consistent with a critical density for the metal-insulator transition of about 10^{15} cm^{-3} (the effective mass is $m^*=0.04m_0$). If the layer growth results to be non pseudomorphic, a strain relaxation at the InGaAs-substrate interface occurs: a high dislocation

density, thus lattice disorder, is expectable. This can be certainly responsible for the observed low mobility values.

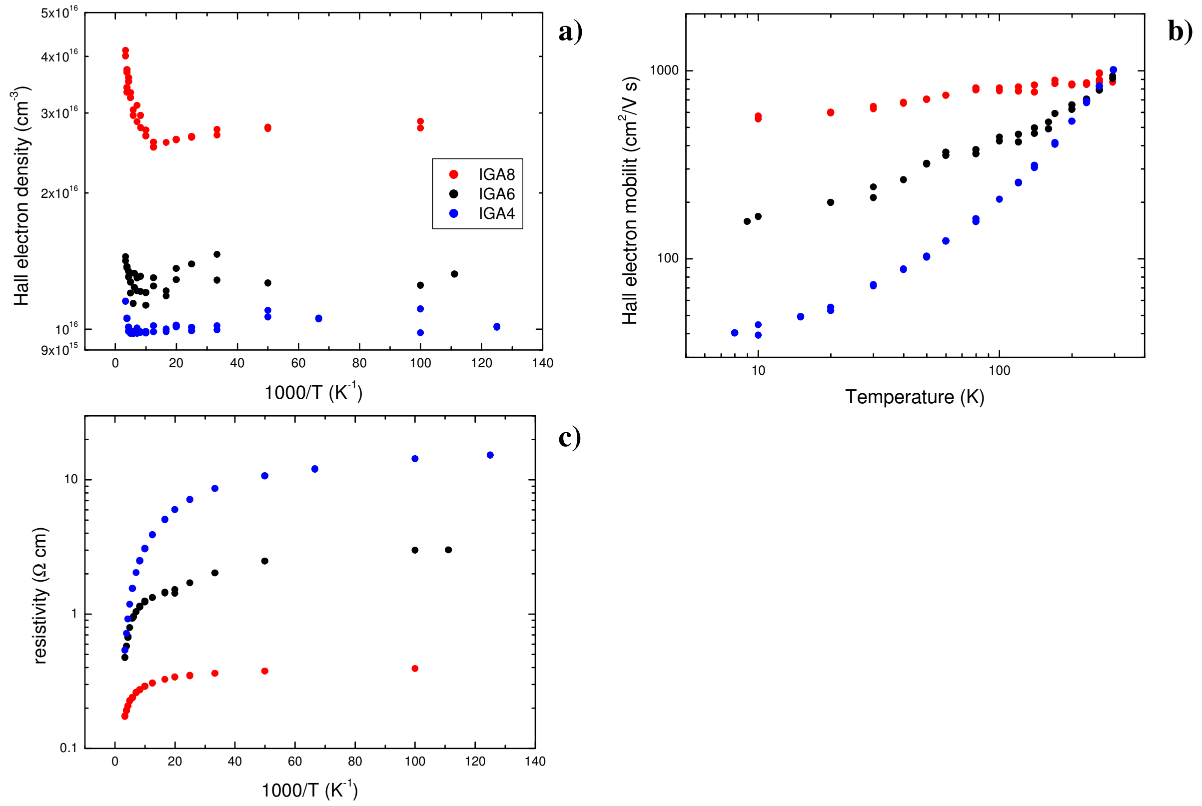

Fig.7.4: Hall effect measurements on an undoped InGaAs layer: carriers density versus 1000/T (a) mobility versus T (b) resistivity versus 1000/T (c)

Sample	Type	Carriers Concentration (cm^{-3})	Mobility (cm^2/V s)	Resistivity (Ohm cm)	V/III Ratio	T_G (°C)
IGA4	N	1.172×10^{16}	1003.87	0.531	20.6	600
IGA5	N	5.834×10^{15}	752.46	1.424	34.3	600
IGA6	N	1.444×10^{16}	918.57	0.471	6.9	600
IGA7		No	trustworthy	measures	20.6	550
IGA8	N	4.006×10^{16}	901.61	0.173	20.6	650

Tab. 7.2: Electrical measurements on InGaAs layers

Table 7.2 summarizes the results obtained from electrical transport measurements, performed on InGaAs/InP samples.

Another systematic study was carried out to analyze the relation between Indium incorporation and V/III ratios in the vapour phase.

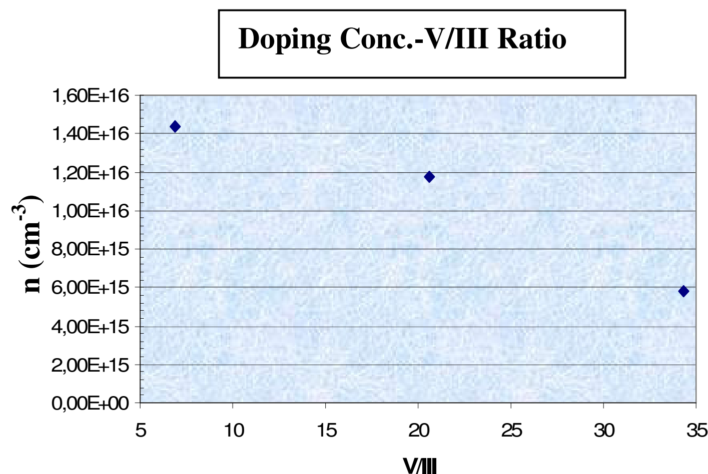

Fig.7.5: Doping measured by Hall effect as a function of the V/III ratio.

As we can see in the graph of fig.7.5, the donor background impurity density decreases with the increasing of the V/III ratio. In spite of the low number of samples, grown at the same temperature, we can recognize a trend; further investigations are obviously required to confirm such behaviour.

7.3 Growth of n-doped InGaAs

The InGaAs based heterostructures, grown by MOVPE with the purpose to study the subsequent ion implantation of Fe, were formed by the following layer sequence, described in fig.7.6.

An n-doping optimization, by Silicon, was performed, on the basis of previous works [7.8].

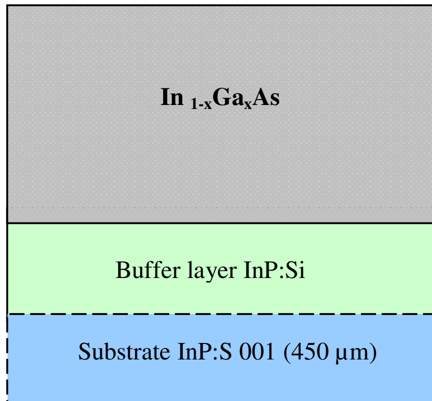

A part from the Silicon doping, the InGaAs layers chosen for implantation were grown in the same conditions of sample IGA18 (see table 7.2) which exhibited the best structural properties.

Fig.7.6: Scheme of a typical InGaAs/InP grown heterostructure

Sample	Thickness (nm, meas. by SIMS)	Nominal doping (cm^{-3})	X_{Si}/III ratio in vapour phase
IGADOP1	1400	$1x10^{17}$	$0.4x10^{-4}$
IGADOP2	1100	$1x10^{18}$	$5.4x10^{-4}$
IGADOP3	1400	Undoped	0

Tab. 7.3: Properties of the doped InGaAs layers;

The investigations on implantation are still in progress.

References VII

[7.1] M.Suzuki and M.Tonopuchi, Appl.Phys.Lett. 86,163504 (2205)

[7.2] Sadanand M. Gulwadi, Mulpuri V. Rao, Alok K. Berry, David S. Simons, Peter H. Chi, and Harry B. Dietrich J. Appl. Phys. 69, 4222 (1991)

[7.3] H. Roehle, H. Schroeter-Janssen[1], P. Harde[1] and D. Franke[1], Journal of Electronic Materials, Volume 24, Number 11 / November, 1995

[7.4] H. Dumont, L. Auvray and Y. Monteil, Optical Materials 24 (2003) 309-314

[7.5] *Ito H.; Kurishima K.; Watanabe N.* Journal of Crystal Growth, 158 (1996) 430-436

[7.6] Cui, D.; Pavlidis, D.; Eisenbach, A., Characterization of carbon induced lattice contraction of highly carbon doped InGaAs
Indium Phosphide and Related Materials, 2000. Conference Proceedings. 2000 International Conference on14-18 May 2000 Page(s):526 - 529

[7.7] M. Ogasawara, K. Sato and Y. Kondo, Appl. Phys. Lett., 60(10), 217 (1992).

[7.8] Xg Xu, C. Giesen, J. Xu, M. Heuken, K Heime, Journal of Crystal Growth 181:1-21-2, 26-32,(1997)

Part III: MOVPE growth of InAsP/InP layers doped with a magnetic impurity (Mn)

Chapter 8

An introduction to Magnetic Semiconductors

The research on magnetic materials is a huge and interesting field in the landscape of materials science, especially thinking about the possible applications for the realization of memory devices, indispensable for informatics technology, the data storing in hard disks, magnetic tapes, and magneto-optical disks. Those all exploit the electronic spins of ferromagnetic materials. Recently ferromagnetic semiconductor research gained again interest. These are materials able to exploit at the same time magnetic spins and electronic charges, to unify the two most important branches of condensed matter physics: semiconductors and magnetic materials. The spin manipulation in semiconductor devices is certainly complex but a fascinating goal; it would open the field of the so called spintronic (semiconductor spin transfer electronic) for developing devices acted to read and write no volatiles information through magnetism [8.1].
Injection control, transport and detection of charged carriers with polarized spin could be used in new generation devices, like electronic-magnetic-photonic chips, lasers and magnetic sensors. Considering that the semiconductor magnetic properties are dependent on charge concentrations in the material, through the effect field in transistor structures, it would be possible to obtain a magnetism control, electronic or optical based. Moreover, since the spin state can be univocally “up” or “down”, giving a natural binary code, the obvious consequence is thinking about digital applications, with the realization of “qubits”, basic elements for quantum computer. An approach to fabricate this kind of devices was the injection of charges from a ferromagnetic metal to a semiconductor. But the initial results were not satisfactory, since only 1% efficiencies were obtained. Only recently, through fabrication of tunnel barriers or Schottky, exploiting ballistic transport, efficiency overcame 90% [8.2].

However while spin transport over 100 μm was demonstrated [8.3], injection represents still a weak point. Another solution would be a ferromagnetic semiconductor. In this case the fundamental problem is that raw materials for higher efficiency devices, like GaAs and Silicon, are not magnetic. Vice versa the crystal structure of typical magnetic materials are completely different from those applied in electronic. There are materials, like Europium Chalcogenides and semiconductors spinels, that show simultaneously semiconductor and magnetic properties, but they cannot easily integrated with classic semiconductors, having a different structure. They present also a very complex crystal growth (high growth times, up to a week for a limited dimension crystal) that limit their applications in process technology and overall they cannot be doped.
Consequently , new magnetic semiconductors through doping were thought. This can be done introducing a strong dose of magnetic elements, like Mn, for example into a GaAs matrix, to obtain magnetic behaviour.
It would be very advantageous because the magnetic materials production would be included in an already developed technology. Another essential goal would be ferromagnetic behaviour at room temperature, realizing materials with a Curie Temperature (the temperature above which the material loses its ferromagnetic characteristic and acts similarly to a paramagnetic) over 300K.

8.1 Diluted Magnetic Semiconductors

"making nonmagnetic semiconductors ferromagnetic" with this formula Ohno thought in the nineties and then effectively developed the process of the so called DSM (diluted magnetic semiconductors) [8.4-8.5]. It is based on a process in which magnetic ions, transition elements or rare earths in particular, are introduced into a semiconductor material's matrix. They substitute a certain fraction of atoms in the originally not magnetic structure. Considering the "mean field" model (valid in the case of random distribution of Mn atoms in the matrix), an exchange interaction between Mn ions magnetic moments mediated by free holes changes the electrical and magnetic properties. Finally for very strong coupling a ferromagnetic phase transition occurs, as observed in PbSnMnTe [8.6].
DSM research started with II-VI semiconductors, in which a high concentration of introduced metals is possible. But because of their major role in electronic it is to be wished that this process is applied to III-V semiconductors. In fact high Mn doped GaAs or InAs introduced became recently of interest.

A strong limitation of this research is represented by the low equilibrium solubility of transition metals, like Mn, in III-V alloys; In contrast with ions concentration over 10^{18} cm^{-3} needed to obtain measurable magnetic effects.
Unfortunately, beyond its solubility limit Mn causes segregation or even the formation of a secondary phase that limits a further ion incorporation into the crystal. It is evident that for these reasons, the realization of DMS III-V semiconductors should require a hard work.
However, techniques like MBE, for example, working far from the equilibrium conditions, allow for low temperatures growths and a potential incorporation of impurities beyond their equilibrium solubility.

8.2 The example of (Ga,Mn)As

In Mn doped GaAs, grown by MBE, at low temperatures magnetic properties were observed. Mn is the most suitable magnetic element for this purpose, considering that it is a source of magnetic dipoles with its half filled d shell and at the same time because it provides holes for exchange. It occupies the sites previously occupied by Ga and it is the most "shallow" acceptor among transition elements. This feature is fundamental because ferromagnetic interaction between magnetic moments was shown to be holes mediated. Particular attention deserves the location that Mn assumes after being introduced into the material. Indeed, while the substitutional Mn is an acceptor and contributes to the total material magnetic state, interstitial Mn, as observed too [8.7]
acts like a donor, tending to have a negative effect for magnetization, compensating the holes and lowering the Curie temperature.
It is important trying to avoid some defects, for example As like antisites commonly present in GaAs grown by MBE at low temperatures. In this case, in fact, the Arsenic antisites provide deep donors rendering ineffective the holes Mn doping. The total magnetization is indeed followed by a sharp drop of the average magnetic moment at As_{Ga} concentration above 1%.
A Mn quantity over 8% in GaAs does not allow smooth homogeneous layers, while as experimentally observed, a concentration less than 4% does not produce any observable magnetic effects. The highest Curie temperature until now, obtained for GaAsMn systems, is 110K with a Mn concentration of 5%. Magnetization measurements, performed by SQUID, evidenced indeed hysteresis loops, in dependence of the magnetic field applied, sign of well ordered ferromagnetic structures [8.8]. Of relevance is also that the more accentuated hysteresis was detected for parallel fields to the surface's sample, showing that the easy axis is indeed parallel to the growth direction.

In structures like InMnAs instead (and the same case would be for InAsP:Mn), a perpendicular easy axis was found. This effect is probably caused by a magneto-elastic stress: biaxial strain in (In,Mn)As makes the lattice spacing perpendicular to the surface lower than one in the plane, on the contrary in (Ga,Mn)As on GaAs under compressive strain, the in-plane parameter is smaller than the perpendicular one. This conclusion is supported by the observation of a perpendicular easy axis when the GaMnAs is grown on InGaAs, when it submits a tensile stress.

Low temperatures magnetization measurements would evidence a 5/2 spin value, as expected for Mn^{2+} and 2 for Mn^{3+}.
Very interesting are the magneto-transport properties. The Hall coefficient R_{Hall}, in case of magnetic materials, is characterized by an anomalous component, proportional to the magnetization M.

$$R_{Hall} = \left(\frac{R_0}{d}\right) B + \left(\frac{R_S}{d}\right) M \tag{8.1}$$

Where R_0 is the normal Hall coefficient, R_s (=cρ) is the anoumalous Hall coefficient, B the magnetization field and M the magnetization of the sample.
The example in Fig.8.1 shows the R_{hall} development in function of T or B for a (Ga,Mn)As (Mn=0,053) material [8.4]. The anomalous Hall term (second term in 8.1) is the dominant term up to room temperature. At lower T, R_{Hall} follows an hysteresis like M (as shown in fig.8.1). In fact, because the anomalous Hall term proportional to M is dominant, RHall reflects the B and T dependence of M.

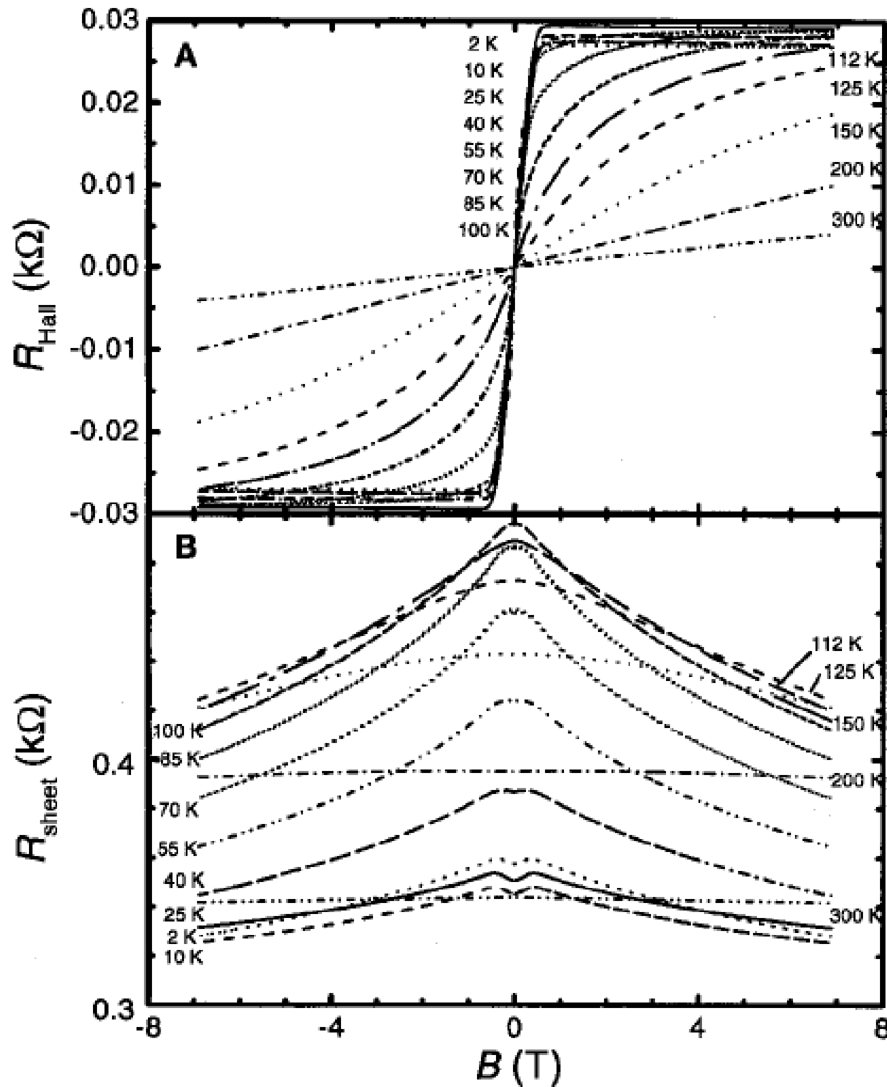

Fig.8.1: R_{sheet} and R_{Hall} in function of B(T) in a (Ga,Mn)As sample [8.4]

8.3 Calculation of the Curie Temperature in DMS

The nature of magnetism in these materials is still under investigation. What is verified is that it is holes induced, originated from a coupling between the wave functions of electric charges and the holes electronic spins. Indeed the samples with an n-doping show an anti-ferromagnetic behaviour. Many theoretical studies point out to the so called RKKY (Ruderman-Kittel-Kasuya-Yosida) [8.9-8.10-8.11] interaction as responsible for ferromagnetism. In the limit which the average separation between carriers is more than the spins one, the RKKY model is equivalent to the Zener model,

developed in 1950. In this case, the Friedel spin polarized quantistic oscillations can be not considered. [8.12].

The Zener model predicts how the Ginzburg Landau free energy depends on magnetization of the localized spins. The spin orbit coupling and the kp interaction (mixing of the angular momentum basis states associated with the delocalization of atomic orbitals) play an important role.
The Ginzburg Energy is also conditioned by carrier-carrier interactions that can be described by the Fermi-liquid parameter A_F. This model implies a temperature of Curie determined by ferromagnetic and antiferromagnetic contributions, according to the mean-field approximations and valid for long-range exchange interactions. And it can be calculated as follows:

$$T_C(x) = A_F\left(\frac{x_{eff}}{0.05}\right)\left(\beta N_0[eV]\right)^2\left[\frac{N_0(GaAs)}{N_0}\right]T_F^{nor} - T_{AF}(x) \quad (8.2)$$

[8.12]

Where T_{AF} is the antiferromagnetic temperature, A_F is the Fermi-liquid parameter, that describes the carrier-carrier interactions and is 1,2 in this case. β is the p-d exchange integral and N_0 the concentration of cation sites. T_F^{nor} is the normalized ferromagnetic temperature, not dependent from the Mn concentration (T_F/x_{eff} where T_F, ferromagnetic temperature is T_C+T_{AF} and x_{eff} the Mn concentration).
The mean field model offers estimates of different material critical temperatures. Considering a 5% Mn doped material and a holes density of $3{,}5 \times 10^{20}$ cm^{-3}, estimates in fig. 8.2 were obtained. Considering that βN_0 is proportional to a_0^{-3}, where a_0 is the lattice parameter, it is evident that for lighter materials, or smaller lattice constants, (where the p-d hybridization is higher and the spin-orbit coupling reduced) higher Curie temperatures are obtained. Extending the model to wurtzite structure based, like in the case of ZnO and GaN, Curie temperatures higher than room temperature were predicted [8.12].

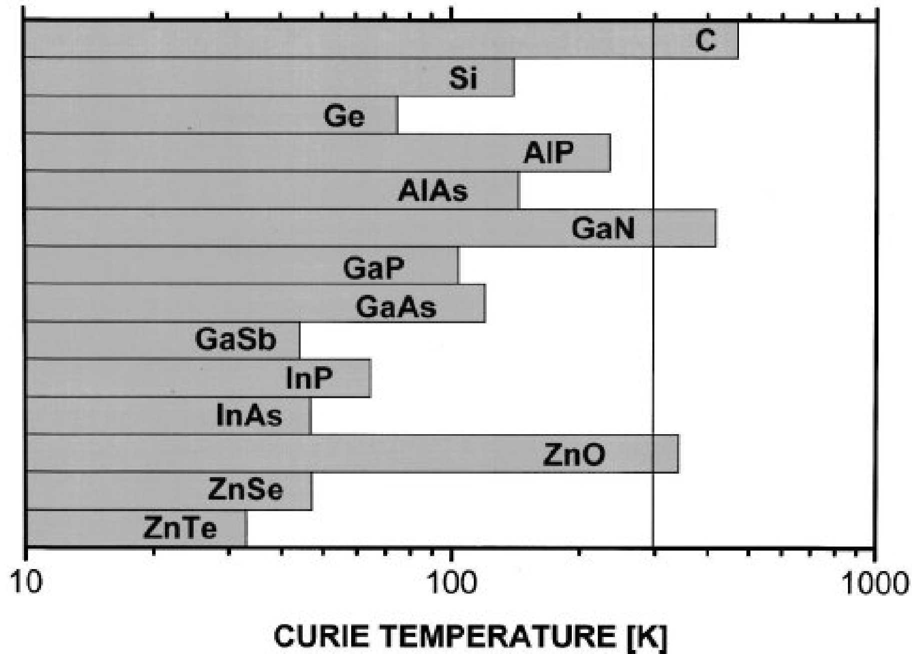

Fig.8.2: Different DMS's Curie Temperatures predicted by the model, considering a holes concentration of $3{,}5 \times 10^{20}$ cm^{-3}.

Naturally, this is only a theoretical approach; in reality, the nitrides show many complexities. While is possible to dope a material as GaAs, up to $10^{21} cm^{-3}$, with shallow acceptors like Carbon, GaN p-doping is strongly limited to much lower values. The classic doping in GaN is Mg, that presents a relatively deep level (E_V+0,17). Consequently, at room temperature, holes concentration is only $3 \times 10^{17} cm^{-3}$. In case of Mn the occupied level is very deep in the gap, 1.4 eV [8.14] making the doping ineffective.

Further difficulties arise because Mn can occupy 3 different sites, substitutional at the Ga place but also interstitial where it acts like a donor, or it precipitates in the MnN or GaMn alloy form. However alternative methods for reaching high holes concentrations provided by Mn in GaN are in a developing phase: co-doping of acceptors and donors to reduce the self compensation effect, or super lattices AlGaN/GaN selectively doped, in which holes transfer from Mg acceptors in the AlGaN barrier toward GaN quantum wells (in this way with the possibility to reach a 10^{18} doping). In general, a good crystal quality, therefore optimal growth conditions, such to avoid as possible extended defects as traps in the bulk, could allow for Curie temperatures up to 300K.

8.4 Doping by ion implantation

The important argument is that, though the difficulties described, many studies performed on Mn doped GaN realized in different ways, proved the effective presence of ferromagnetism near room temperature. The doping was achieved by diffusing Mn in solid state after deposition or performed by ion implantation.

However the observed magnetizations were usually very small. Newer studies indicate that sapphire substrates themselves have a small magnetization which strongly varies between different treatments.

One of the possible solutions such to obtain magnetic semiconductors could be the introduction of Mn through implantation. We discussed in the previous chapters how the implantation is extremely useful to compensate high doping levels, allow to work far from equilibrium conditions. In this way it would be possible to remedy the typical growth problems, as in MOVPE, during which, an excess of Mn segregates or forms secondary phases.

However to recover the lattice damages the samples must be thermally annealed after the implantation process. During annealing often a second phase forms. Moreover due to the different crystal structure the secondary MnAs or MnP phase are usually not visible by X-ray scans. Finally many of the implanted samples without co-doping did not show any increased p-type conductivity, which make the reported high T_c very doubtful. Especially when these T_c coincide with T_c(MnAs) $\approx$320K or T_c(MnP)$\approx$300K.

Examples of the using of implantation for Mn doping gave the results shown in the work of Theodoropoulou [8.15-8.16] In this case the GaP substrate highly doped with Carbon ($10^{20}cm^{-3}$), therefore p type, was implanted with Mn up to a 3% concentration, permitting a Curie temperature nearby 300K. After Mn implantation a secondary phase, like GaMn or MnP was not found by XRD (but to be counted are the precedent considerations).

Though implantation offers the opportunity to obtain room temperatures magnetic semiconductors in case of GaN:Mn, both for bulk or epitaxial layers, different secondary phases are expected.

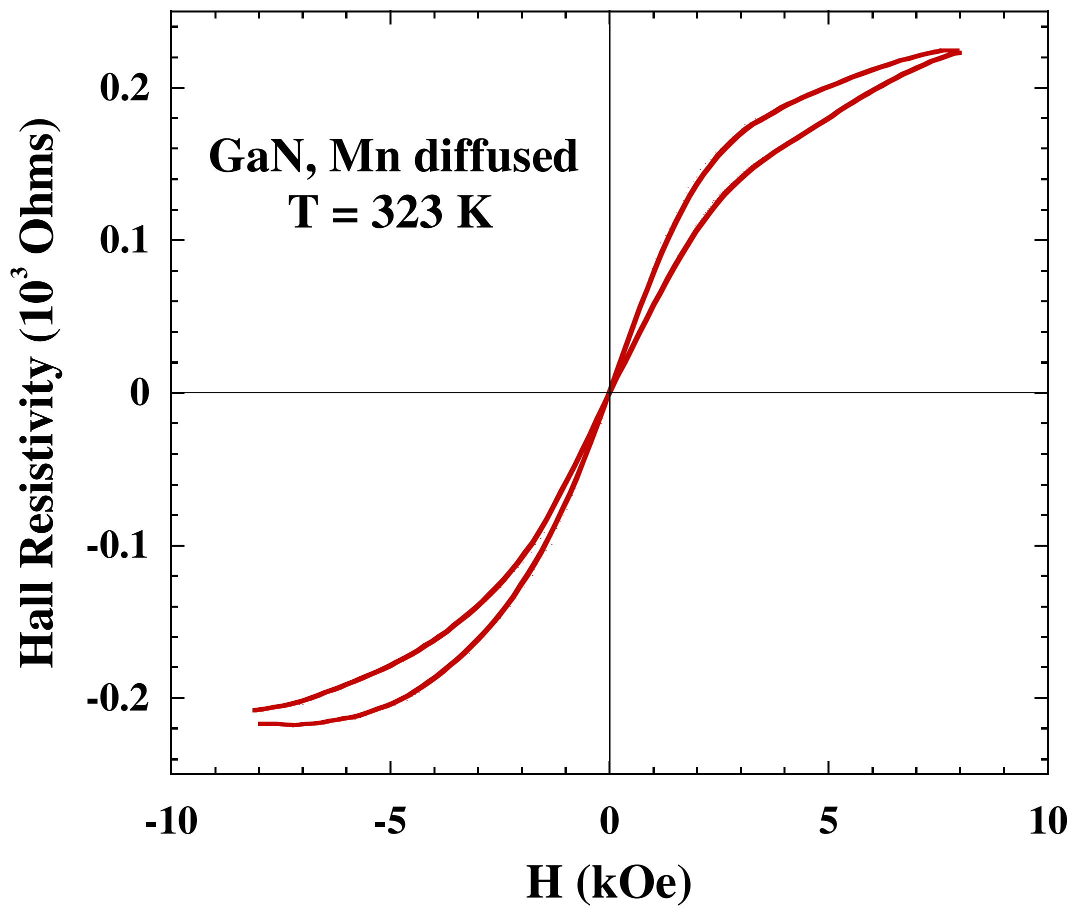

Fig.8.3: Hall resistivity hysteresis on a GaN:Mn implanted sample[8.17].

References VIII

[8.1] Y.Ohno D. K. Young, B. Beschoten, F. Matsukura, H. Ohno and D. D. Awschalom, Nature 402, 790-792 (1999)

[8.2] Georg Schmidt and Laurence W.Molekamp, Journal of Applied Physics, 89 ,11, (2001)

[8.3] J.M. Kikkawa and D.D. Awschalom, Nature 397, p.139-141 (1999)

[8.4] H.Ohno Science 281, p.951 (1998)

[8.5] Munekata, H.Ohno, S. von Molnar, Armin Segmueller, L.L.Chang and L.Esaki, Physical Review Letters, 63 (17), p.1849, (1989)

[8.6] T.Story, R.R. Galazka, R.B. Frankel, and P.A.. Wolff, Phys.Rev.Lett.56,777(1986)

[8.7] L.Berqwvist, P.A.Korzhavy, B.Sanyal,S.Mirbt, I.A.Abriskov, L.Nordstroem, E.A. Smirnova, P.Mohn, P. Svedlindh and O.Eriksson Physical Review B 67, 205201 (2003)

[8.8] H. Ohno, A.Shen, F.Makamura, A.Oiwa, A.Endo, S.Katsumoto and Y.Iye. Appl.Phys.Lett.69, 3 (1996)

[8.9] M.A.Ruderman and C.Kittel, Physical Review Vol.96, Num.1 (1954)

[8.10] T. Kasuya, Prog. Theor. Phys. 16, 45 (1956)

[8.11] K. Yosida, Phys. Rev. 106, 893 (1957)

[8.12] T.Dietl, H.Ohno, F.Matsukara, J.Cibert, D.Ferrand. Al. Science, 287, 1019 (2000)

[8.13] S. J. Pearton, Y. D. Park, C. R. Abernathy, M. E. Overberg, G. T. Thaler, Jihyun Kim and F. Ren, Journal of Electronics materials, 32, 5 (2003)

[8.14] Korortiev, R.Y., Gregie, J.M. and Wessels, B.W. Optical Properties of the Deep Mn Acceptor in GaN:Mn, Appl. Phys. Lett. 80, p.1731-1733 (2002).

[8.15] N.Theodoropoulou, A.F.Hebard, M.E. Overberg, C.R. Abernathy, S.J.Pearton, S.N.G. Chu, R.G. Wilson, Physical Review Letters 89, 10 (2002)

[8.16] Theodoropoulou, N.A., Hebard, A.F., Overberg, M.E., Abernathy, C.R., Pearton, S.J., Chu, S.N.G. and Wilson, R.G. Magnetic and Structural Properties of Mn-Implanted GaN,Appl. Phys. Lett. 78, 3475-3477 (2001).

[8.17] Reed, M.L., El-Masry, N.A., Stadelmaier, H.H., Ritums, M.E., Reed, N.J., Parker, C.A., Roberts, J.C. and Bedair, S.M. Room Temperature Ferromagnetic Properties of (Ga,Mn)N, Appl. Phys. Lett. 79, 3473-3475 (2001).

[8.18] H.Ohno J,Vac.Sc.Technol. B 18,4,(2000)

[8.19] Ohno, H. Ferromagnetic III-V Heterostructures, J. Vac. Sci. Technol. B18, 2039-2046 (2000).

[8.20] Tomasz Dietl J.Appl.Phys.Vol.89. no.11p.7437

Chapter 9

Tailoring of Mn-Acceptor depth in InAsP grown by MOVPE

The growth of diluted magnetic semiconductors by MOVPE for GaMnAs and InMnP was not successful. Manganese clusters (9.1) were the only magnetic structures. For InMnP the maximum Mn content, was found to be 1%, not enough for magnetic effects, because the free carrier concentration is too low. Even more they freeze out already at 120 K, thus there are no holes-spin coupling.

Other possibilities to enhance the free carrier concentration at lower temperature are the use of not equilibrium doping techniques like ion implantation or, still in the equilibrium regime, reducing the depth of manganese acceptors.

The tailoring of Mn Acceptor depth could be performed in a material like $InAs_{1-x}P_x$ where the acceptor localization energy reduces from 230 meV of InP to 0 for $InAs_{0.6}P_{0.4}$ up to resonance with the valence band for InAs.

Our aim was to approach this level close to the valence band to obtain a high doping and high free carrier concentrations also at lower temperatures, without Mn clusters formation. At the same time, the intention was to “stop” the Mn energy level before the crossover with the valence band, because in this conditions the coupling between acceptors would result shielded from the valence states.

9.1 Introduction to the InAsP/InP:Mn system

In III-V semiconductors Manganese acts as deep centre or shallow impurity [9.2]. In an $InAs_{1-x}P_x$ alloy, the transition energy connected to the Mn occupied level depends on the alloy composition. The location of the Mn energy level was studied by K.Huang and B.W.Wessels [9.3], in dependence of Arsenic concentration by photoluminescence measures.

In their work the ionization energy E_I of Manganese was derived from the following formula:

$$E_I=E_g-E_R \qquad (9.1)$$

Where E_R is the emission energy from the deep level, E_g is the energy gap, previously measured [9.4] . The resulted activation energies for different Arsenic concentrations are shown in fig.9.1.

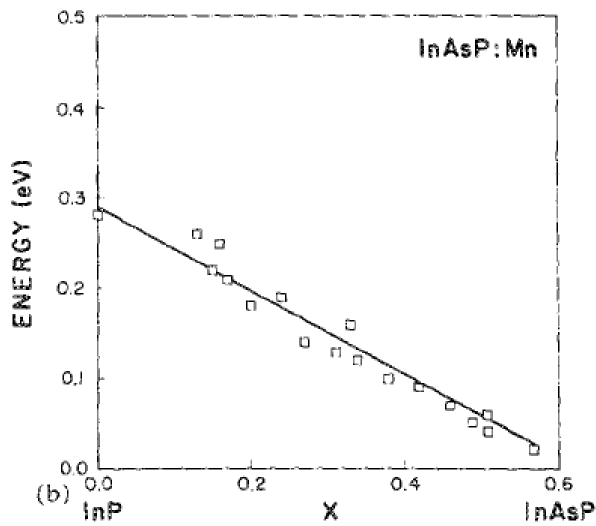

Fig.9.1: Mn level energy emission vs InAsP composition [9.3]

The emission energy of the Mn level varies with the As concentration, because the energy gap changes, while the Manganese level turns to be pinned at a fixed energy (5.41 ± 0.06 eV over the vacuum level). This behaviour is shown in the following picture, Fig.9.2.

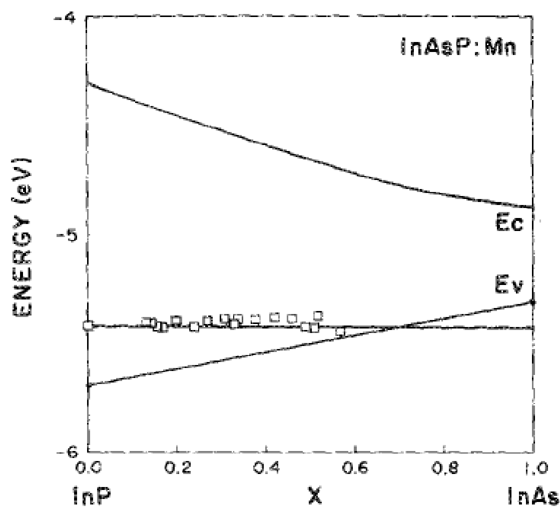

Fig.9.2: the pinned Mn level in the energy gap. [9.3]

For Arsenic concentrations below 65% Manganese acceptors are above the valence band, providing holes for p-type doping and also magnetic moments. The magnetic measurements request high hole concentration, over $10^{19}cm^{-3}$, a really difficult goal, considering the low solubility of the transition metals in III-V semiconductors layers and high activation energies. The only solution seems to be approaching as possible the manganese energy level to the valence band top, to obtain shallow acceptor, strongly activated and able to provide high free hole also at low temperatures.
Unfortunately an InAsP alloy is not lattice matched with an InP substrate. The mismatch increases toward higher Arsenic concentrations, that tends to raise the alloy lattice parameter in comparison with InP. However, in our case, the aim was not to perform pseudomorphic deposition to obtain thick unstrained layers.
Due to the big lattice differences the layers relaxed already after few nanometers. High dislocations density at the interface between layer and substrate is expected. Therefore we have been growing up to 5 micrometers thick layers, monitored with in situ analysis, to achieve an acceptable crystalline in absence of secondary phases.

9.2 Growth of InAsP/InP Mn doped

The InAsP:Mn layers were grown by MOVPE, at the Physics department of TU, Technische Universität of Berlin, in collaboration with prof. Kneissel's workgroup and the supervision of doct. Markus Pristovsek. We used an Aix200 type MOVPE and a 16-channels RAS system for in-situ control [9.5]. The typical growth conditions were the following. H_2 with a total pressure of 10 kPa was used, PH_3 of 200 Pa, TMIn of 1 Pa and TBAs changing between 0 and 3 Pa. The Mn precursor Bis (isopropylcyclopentadienyl) manganese (bcpMn), sketched in the picture below (Fig 9.3), at a vapour pressure from 10 to 40 mPa was used for Manganese doping. With this conditions the growth rate was calculated to be around 2,1 μm/h [9.6].

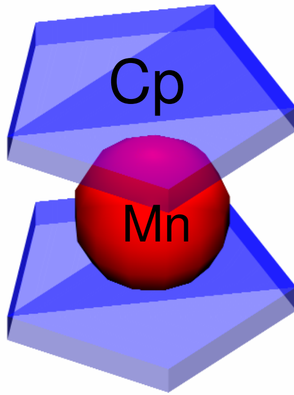

Fig 9.3: Bis (isopropylcyclopentadienyl) Manganese (bcpMn)

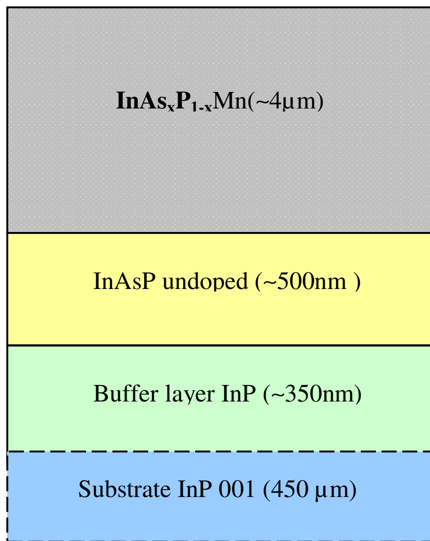

Considering that InAsP has no a lattice matched substrate on the market, as a first step, suitable growth conditions must be studied and the best substrate checked. Between GaAs and InP, we found that InP was the best choice, in fact the recovery of the reflectance signal on InP was very fast, about 5-15 minutes, in comparison with GaAs, 60-100 minutes (see section 9.4).
Most samples had the structure shown in fig.9.4.

Fig.9.4: Typical InAsP:Mn/InP layer grown

The growth sequence was as following. A thin buffer layer was deposited above the substrate. On this, first an undoped layer of InAsP was grown. The layer roughens very fast and then starts to recover. By in-situ control, we could find the moment in which the InAsP structure started to coalescence again (after defects relaxations at the interface), accompanying by decreasing surface roughness. Only at this point (in the most of cases after 15 minutes i.e. a thickness of around 500 nm) also the Manganese doping was supplied.
This procedure was performed to obtain a better crystallinity of the InAsP doped layer. Several thick layers, between 4 and 5 micrometers, were produced (using growth times between 2 and 3 hours) to make the Hall effect measurements feasible also in the case of low doping and minimize effects from the defective heterointerface.
Subsequently HRXRD (to analyze structural properties and Arsenic contents), PL measurements and the Hall Effect measures were performed.
The As concentration of the InAsP:Mn layers obtained are varying between 30% and 93%. The samples parameters are described in the table 9.1 at the end of this chapter.

According to fig. 9.1, the Mn energy level should correspond to a transition from less than 150 meV up to occupy a resonant level into the valence band.
Already as the Arsenic concentrations are higher than 60% in fact, a crossover between the Mn level and the valence band should occur, decreasing the coupling between acceptors because of the abovementioned shielding effect.

9.3 HRXRD analysis

By HRXRD measurements one can to estimate the As and P content percentage in $InAs_{1-x}P_x$ and the crystal quality of the samples.
In the best cases we obtained a single InAsP peak, though quite large as expected from a not pseudomorphic deposition, as shown in the following pictures. The full width at half maximum was found to be around 0,15° for 1523 (fig.9.5c) and 0,12° for 1521 (fig.9.5a) and 1522 (fig.9.5b). Probably the large FHWM and thus the worse crystal structure in the first case was due to the higher Mn flux (13 mPa versus 10 mPa). As shown in fig. 9.6 both a higher Mn supplied and higher As concentrations cause an increase of FWHM.

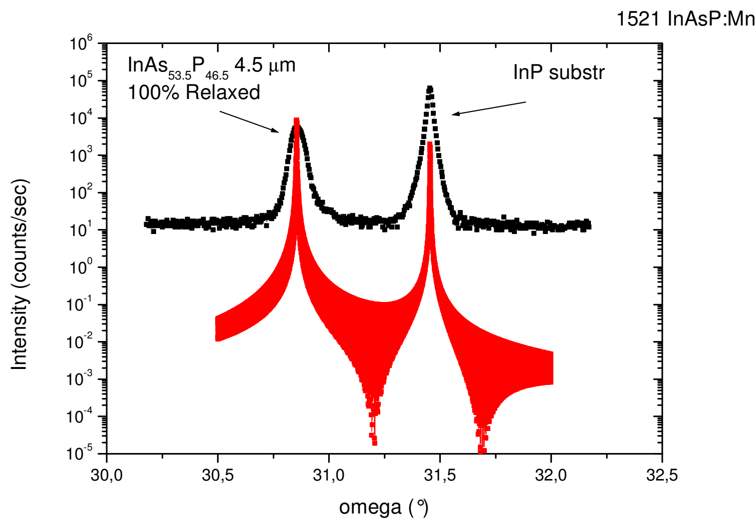

(a)

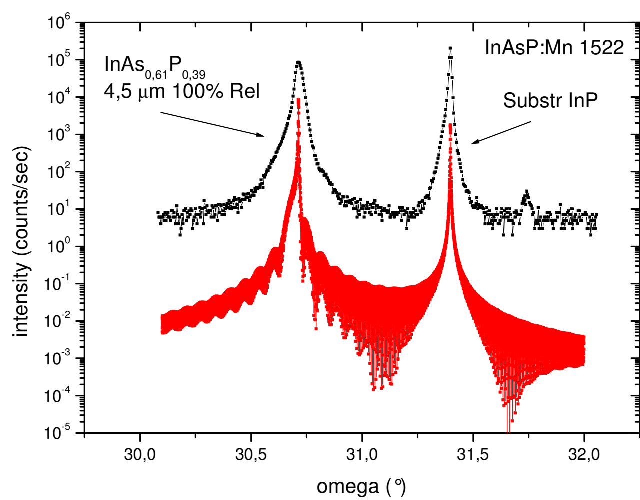

(b)

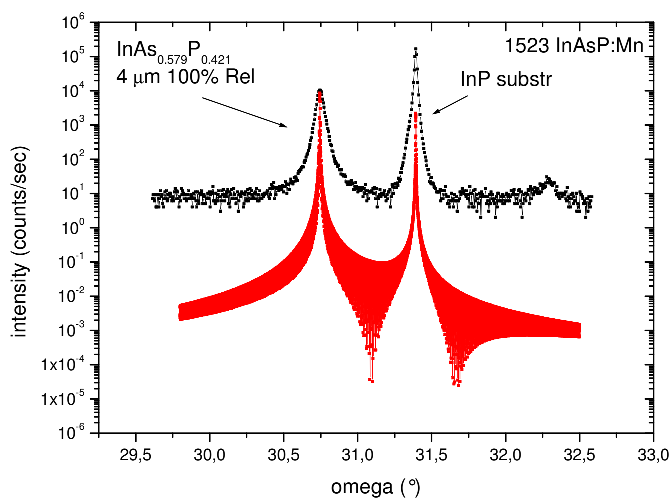

(c)

Fig 9.5: XRD spectra (black) and simulations (red) of 1521 (a) 1522 (b) and 1523(c)

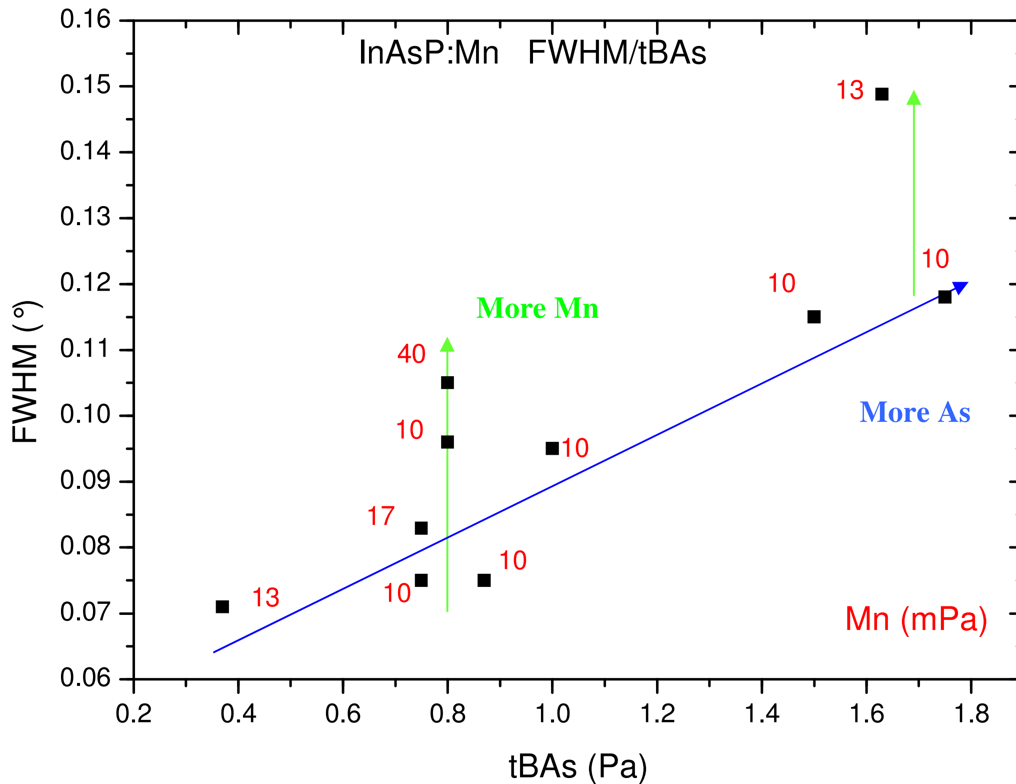

Fig.9.6: the FWHM of HRXRD spectra increases for higher Mn (more distortion) and for higher As (more dislocations)

9.4 RAS analysis

As previously mentioned, during the entire growth duration the RAS signal was detected at 16 wavelength. To each of the 16 channels the anisotropic (AC) and the isotropic (DC) signal intensity was monitored. The RAS signal results from the ratio AC/DC multiplied by a wavelength dependent Bessel factor.

9.4.1 Total reflectance analysis

The DC signal corresponds with the value <r>, i.e. the total reflectance of the surface. The reflectance itself is connected to the growing surface roughness. By a bigger roughness more light is scattered thus the directly reflected light and hence the DC signal decreases.

As already mentioned at the beginning it was useful to choose the most appropriate substrate. As can be observed in fig.9.7, the InAsP:Mn deposition on InP substrate shows much faster recovery of the reflectance signal than in the GaAs case.

Therefore, we decided to grow on InP for all former grow runs.

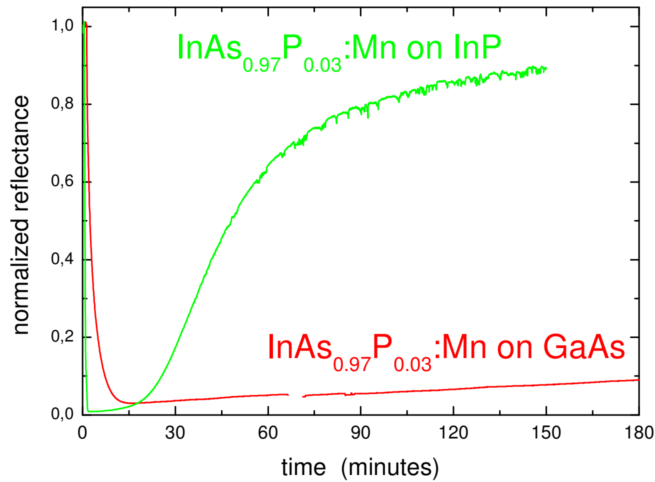

Fig.9.7: InAsP surface reconstruction on InP (green curve) and GaAs (red curve)

Fig.9.8, left top, shows typical DC (reflectance) transients for a good growth run. During deoxidation and buffer growth the reflectance signal is nearly constant. The initial small increase is just a change of the dielectric function due to the increasing sample temperature. When growth is started the signal increases due to the onset of a Fabry-Pèrot oscillation. However after a few nanometers the signal drops very strongly, because the critical thickness has been passed. Growth mode is now 3D and the surface very rough.

The layer needs its time to reconstruct. When the InAsP undoped layer starts to smoothen again, as observed when the DC signal grows, we started with Mn doping. In this way we were quite sure to start from a flatter surface grown over the more defective ones. Therefore in the most the cases we waited 15 minutes, growing InAsP undoped, before Mn doping.

If the bcpMn partial pressure was low enough, the surface further recovers until a stable level is reached. With too high bcpMn flux (typically >10mPa) the DC signal decrease again, dropping to very low values.

In this way, the total reflectance signal's observation can be used to manage and correct the fluxes during growth, decreasing them to obtain a smooth surface.

The observations drives to the conclusion described in this following simple scheme, fig.9.8: fluxes of Mn higher than 10mPa tend to make the growing surface rough, as clear from the drop of the reflectance signal in the doping step. In this case, we probably have a clusters formation.

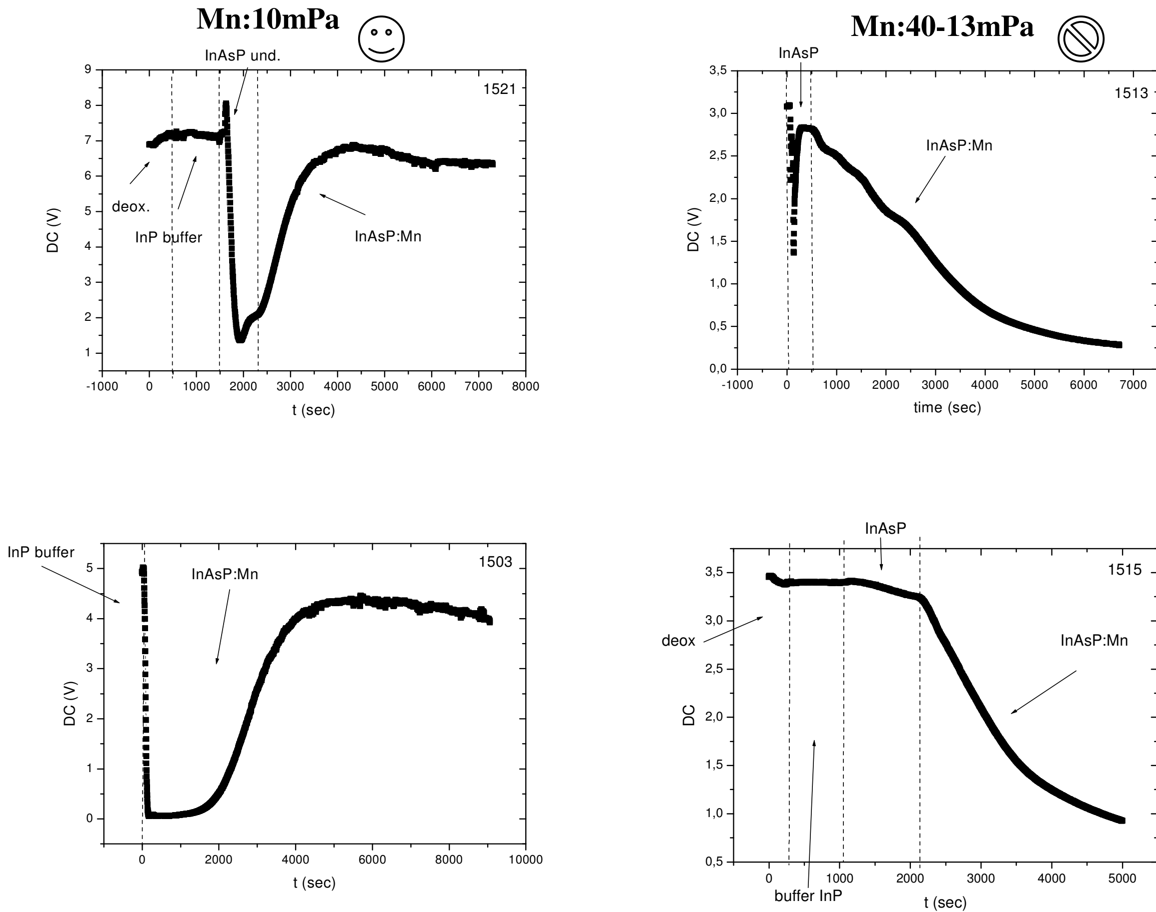

Fig.9.8: Comparison between BcpMn use of more or less than 10mPa: DC signal transient for InAsP:Mn samples supplying a Mn flux of 10mPa (left) and a Mn flux of 17 and 40 mPa (right)

This results naturally suggest the use of a 10mPa Mn flux to avoid clusters formations, indeed this was the approach followed in the most of the following cases.

9.4.2 Reflectance anisotropy

Many additional information on the state of the surface can be obtained by the Reflectance Anisotropy Spectrum. In literature, there are no typical InAsP spectra published so far. However,

features similar to an InP or an InAs reconstruction, depending from different conditions, can be expected. Therefore we present these two spectra in the next graphs, fig.9.9 and 9.10 for reference.

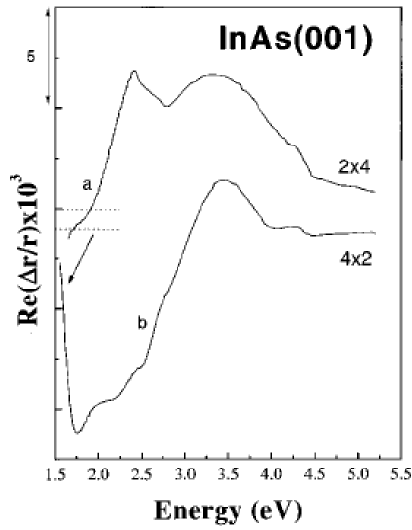

Fig.9.9: InAs reconstruction (2X4) (a) and (4X2) (b) [9.7];

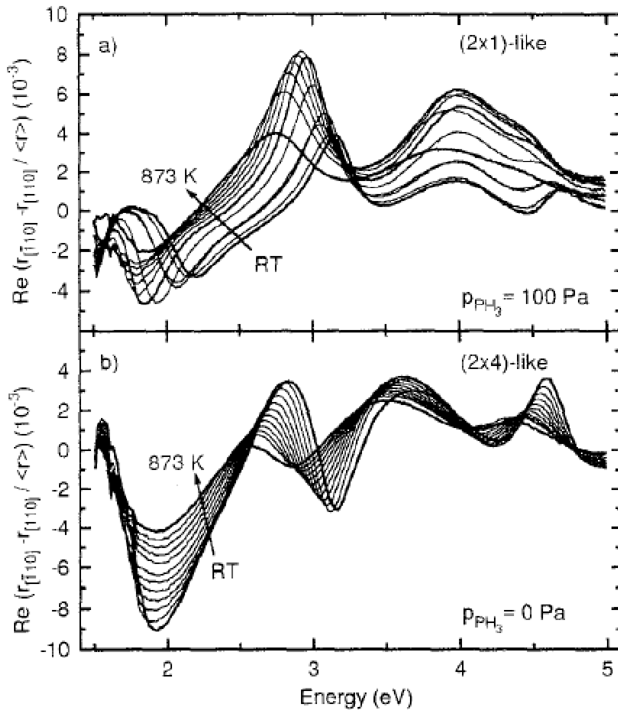

Fig.9.10 (a) reconstruction InP(2X1) [9.8] (b) reconstruction InP (2X4) at different temperatures and PH_3 pressures;

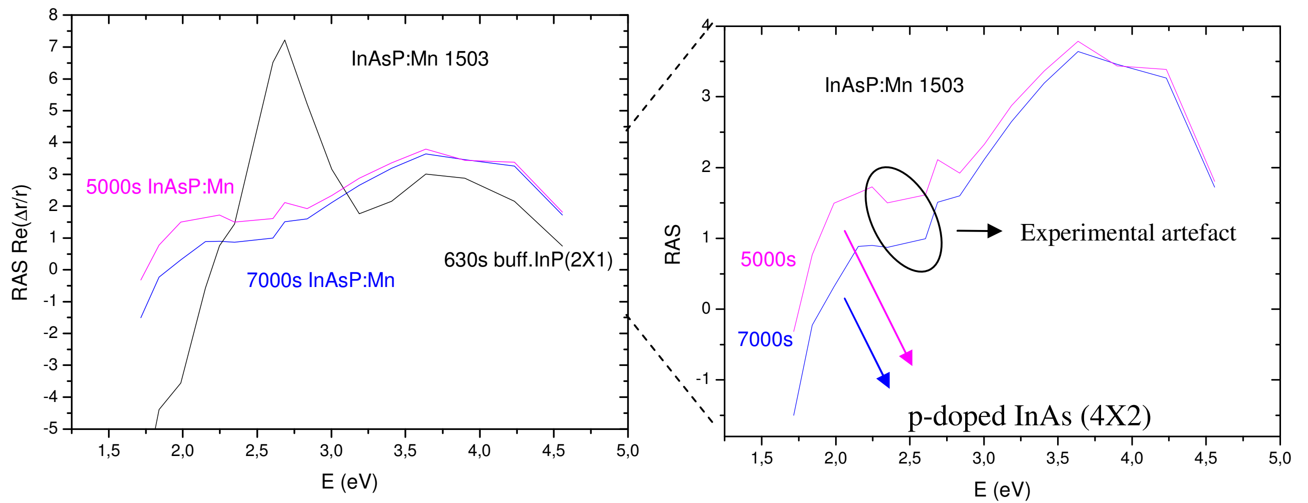

Fig.9.11: RAS spectra during growth of sample 1503 ($InAs_{0.8}P_{0.2}$) at different times

As can be observed in fig 9.11, in the case of 1503 sample (As more than 80%), the spectrum at 630 s, during the InP buffer layer growth, the reconstruction is clearly a InP(2X1), comparable to fig 9.10a. It has the typical main peak at 2,7 eV and another larger peak around 3,8 eV. The spectra at 500 seconds, related to the InAsP:Mn growth, present a different curve, more similar to a InAs (4X2), with a peak around 3,6 eV, not surprisingly since this case the As concentration is more than 80%). The low energy peak, however, decreases with the growth time, possibly due to an increasing amount of (4X2) reconstruction on the surface.

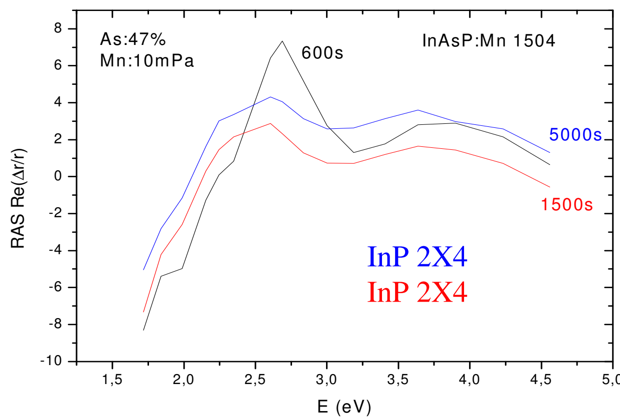

Fig.9.12: RAS spectra during growth of sample 1504 at different times

The 1504, 1505, 1506 and 1509 (fig.9.12-13-14-15) samples show very similar spectra, having similar As concentrations. These spectra resemble a linear combination between an InP (2X1) and InP (2X4). The shift of the maximum reflects the change of the band due to As concentration.

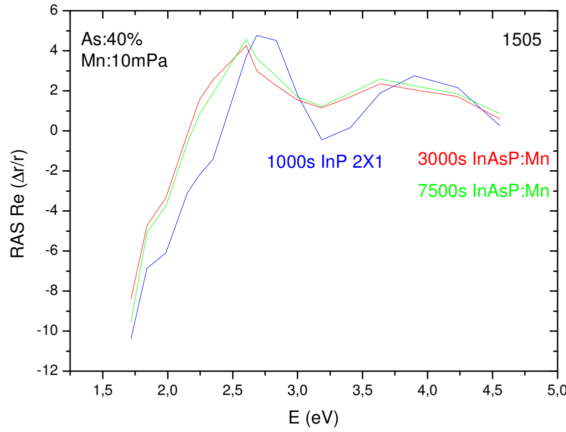

Fig.9.13: RAS spectra during growth of 1505 sample at different times

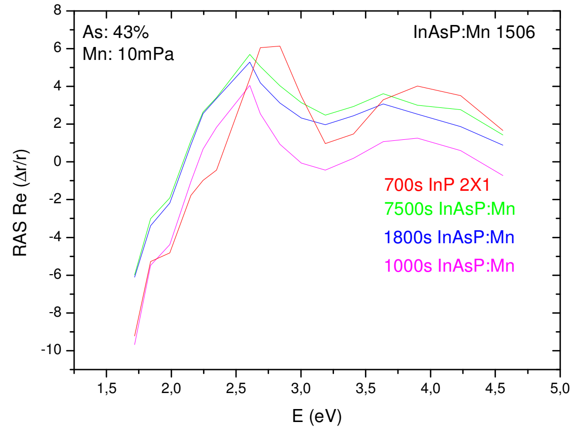

Fig.9.14: RAS spectra during growth of 1506 sample at different times

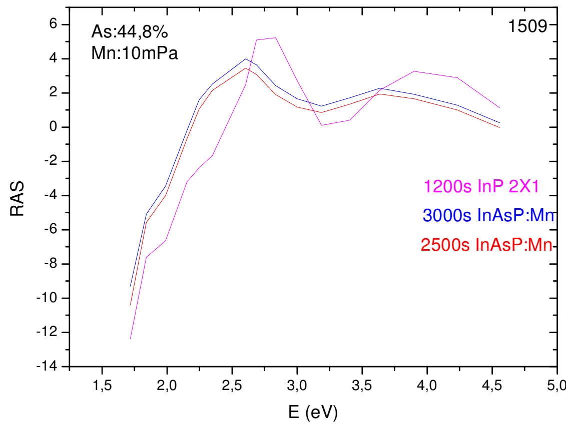

Fig.9.15: RAS spectra during growth of 1509 sample at different times

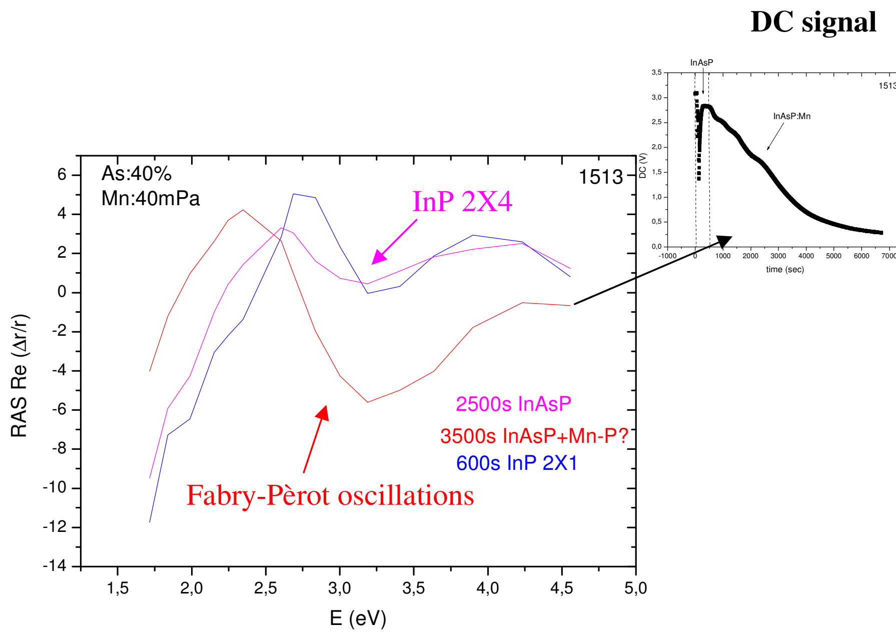

Fig.9.16: RAS spectra of 1513 at different times and connected DC signal (small graph)

In case of bcpMn fluxes exceeding the critical value an RAS spectrum like in fig.9.16 is found. This spectrum is dominated by some Fabry-Pèrot interferences. These occur, since the top rough layer is an effective mixture between InAsPMn and air. Thus refraction index is much lower and thickness interferences can occur.

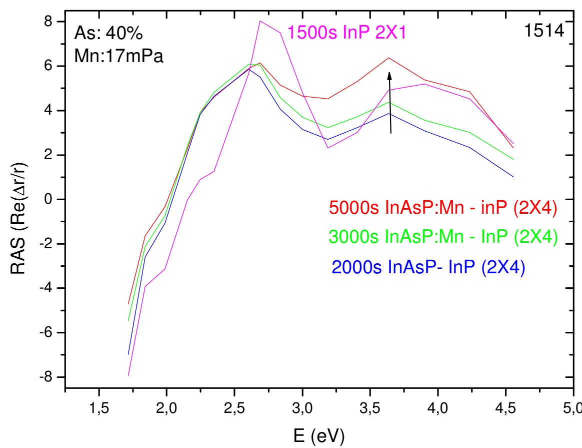

Fig.9.17:RAS spectra of 1514 at different times;

In comparison with the latter case, the reduction of the Mn flux to 17 mPa, as in the 1514 sample (Fig.9.17), leads to lower FWHM and so a better crystalline quality and avoids (or limits) the presence of clusters. In this case, the structure appears to be as in the previous cases, an InP (2X4) like surface.

Moreover, a very interesting feature is present: the RAS intensity increases in correspondence to the doping layer, especially at 3,7 eV (marked by the arrow in fig.9.17). As already mentioned (in section 4.9) the presence of different doped layers introduces an electric field at the layers interface that contributes to the reflectance anisotropy. The intensity increase due to p doping at this energy was already observed in the case of InP samples [9.9]; Thus it seems to be possible also in this material, as for InP and GaAs, from a qualitative estimation of the doping level from the RAS spectrum.

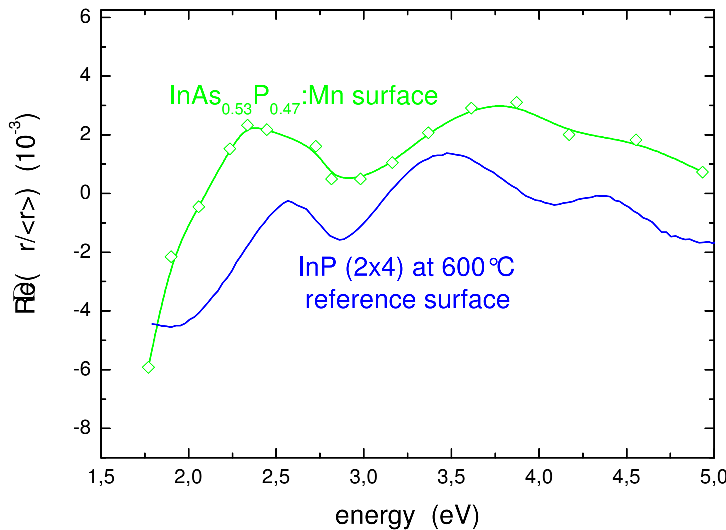

Fig.9.18: Spectrum of 1521 (green curve), connected to the InAsP:Mn reconstruction, compared to an InP (2X4) reference surface (blue curve)

Therefore we could conclude that there is an evidence of InP-type reconstruction up to 70% As and a transition to InAs-type reconstructions between 70% and 90%.

9.5 Determination of Mn-Acceptor depth by Hall measurements

Temperature Hall effect measurements on the InAsP:Mn samples were performed, to check the hole concentration and to calculate the Mn localization energy in the Energy gap, as a function of the As content in the alloy. As shown in fig.9.19, we obtained at maximum a room temperature p carriers density above $3X10^{18}cm^{-3}$ and mobilities at room temperatures between 20 and 80 cm^2/Vsec.
We used the Arrhenius plot based method, to derive the activation energy, as described previously (par.4.6), considering the carrier concentration trend (holes in the case) with the reciprocal temperature.
The samples curves show the passage from an exhaustion region to the freeze out state.
Every samples a part the one with 93% As, showed a freezing out of the carriers, the hole concentrations drop with decreasing temperature. In this situation, assuming a weak compensation ratio, the free carrier concentration has a trend described by the following formula:

$$p \cong \frac{N_P 2}{g}\left(\frac{m_p kT}{2\pi\hbar^2}\right)^{\frac{3}{2}} e^{\left(-\frac{E_A}{2kT}\right)} \quad (9.2)$$

That is very important to determine the activation energy of the deep centres, in fact extrapolating from it, we can obtain that the slope of the log(p) curve with the reciprocal temperature is

$$Slope = -\frac{E_{act}}{2K_B} \quad (9.3)$$

By a linear fit of the first part of these curves (fig.9.19 a), shown in fig.9.20 for sample 1515, we obtained the activation energy of the main acceptor level, presumably connected to the Mn impurity.

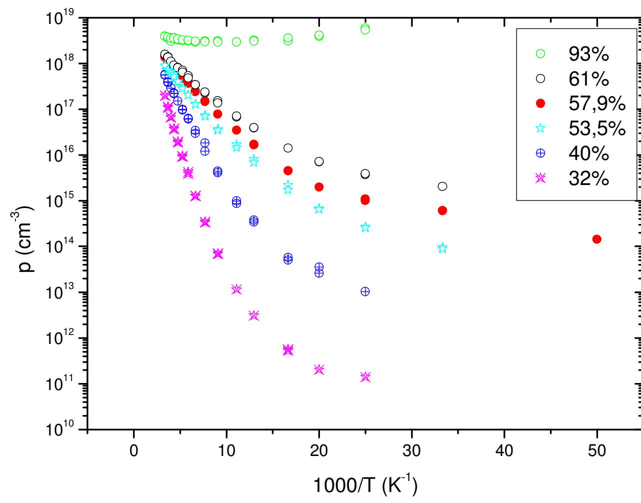

(a)

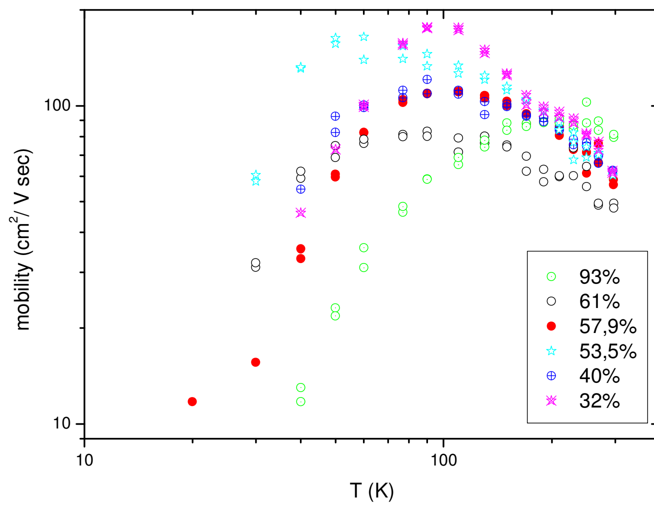

(b)

Fig.9.19: (a) p density vs 1000/T (K) for samples having different Arsenic concentrations (content shown in the inset table) (b) mobility vs T(K) for different As concentrations.

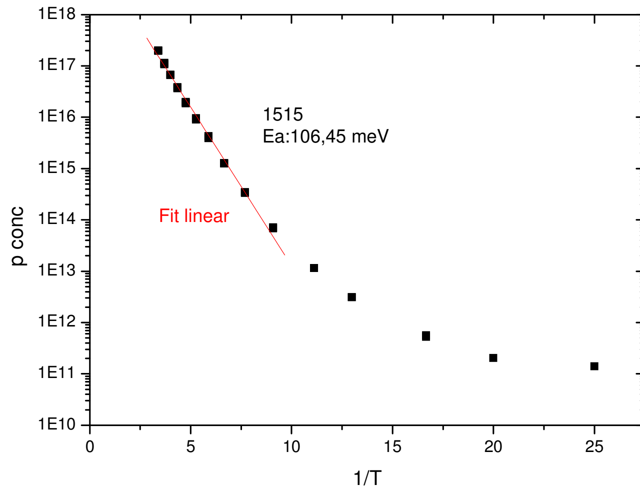

Fig.9.20: Linear Fit on sample 1515 (32% As).

Fig. 9.21 shows the activation energies for all samples. In accordance to ref. [9.3] the activation energy decreases with the increasing As concentration. The slope for As content around 93% was even zero.

In the latter case the level is resonant with the valence band states and the holes on acceptor levels behave like free carriers.

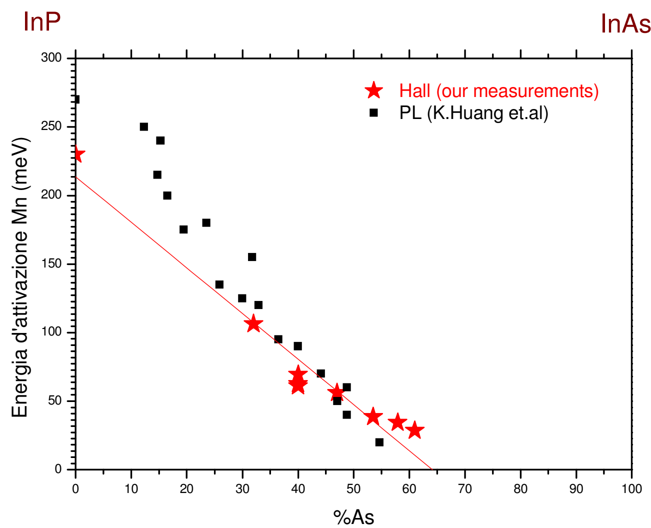

Fig. 9.21: Comparison between E_{Mn} (Mn energy level) obtained (this work) by Hall Effect (stars) and from PL measurements performed By K.Huang et. al [9.3] (rectangles)

A slight difference is certainly due to the different technique and mainly for the fact that in the abovementioned work, PL measurements performed at 10K, are confronted with E_{gap} measured at a different temperatures. Newer experimental literature studies confirm the Mn-relative in pure InP around 230 meV from the V.B top, as in our samples, which explains the difference to [9.3].
This is certainly an important results that shows the tailoring of the electrical activation of the Mn acceptor.

9.6 Photoluminescence measurements

The photoluminescence emission should originate either from Mn-acceptor and bound-exciton. However, increasing the As content in $InAs_{1-x}P_x$ the energy gap emission should decrease. The fig. 9.22 shows the PL spectra, performed at 10 K.

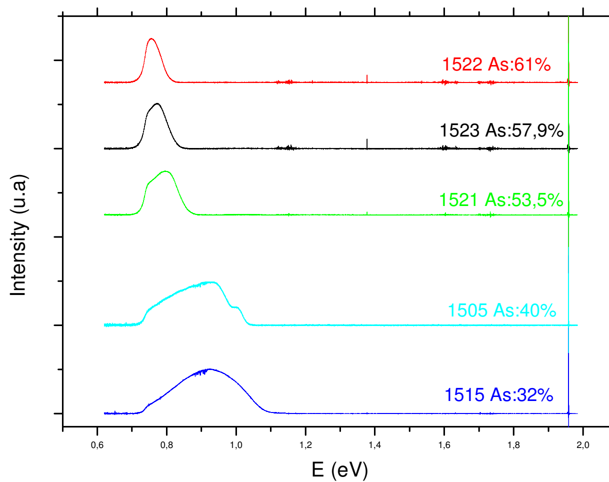

Fig.9.22: PL at 10 K for different As concentrations.

Also in the best cases the full width at half maximum (FWHM) of the emissions peak is quite large, from 40 to 70 meV, as expected for totally relaxed layers. Instead, 1505 and 1515 show really large and superimposed peaks, probably due to an inhomogeneous composition.

In all the cases, the emission spectrum contains multiple contributions, maybe also related to the manganese level. By observing the PL spectrum behaviour, we have the possibility to find a confirmation about the attribution of PL peaks to level due to the Mn acceptors.

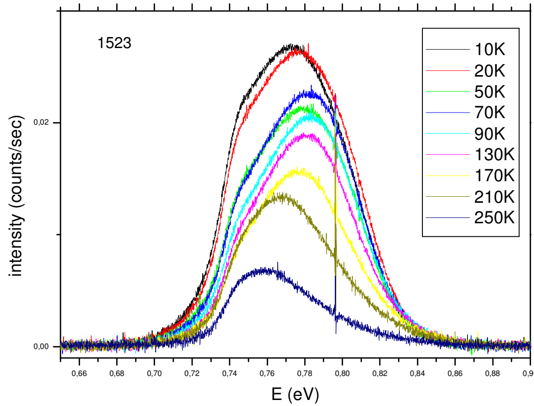

Fig.9.23: PL measurements at different temperatures for 1523;

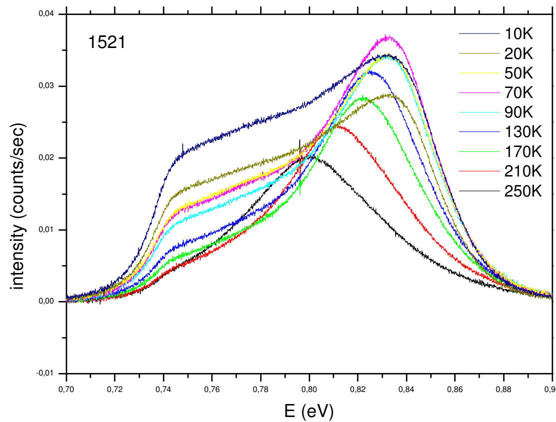

Fig.9.24: PL measurements at different temperatures for 1521

In fact it is observable in fig 9.23 and 9.24, the main peak enhances its energy, by lowering the temperature, as expected for a band to band recombination emission. Instead the peak at lower energy appears only at low temperatures where its intensity increases, while its energy does not change. Comparing the mean peak energy with literature it is likely to compare the band to band energy emission of InAsP with the literature data, as shown in fig. 9.25.

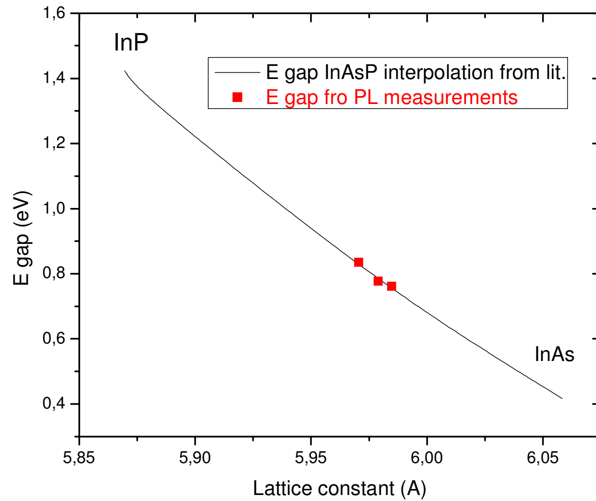

Fig.9.25: Comparison between Egap of InAsP obtained from our PL measurements at 20K (rectangles) and am Egap fit from literature data (black line)

On the other hand, the lower energy peak increases its intensity by lowering the temperature. This is expected from band to acceptor transitions, because the probability to have radiative recombinations of free electrons with the holes frozen at the acceptors levels increases (as sketched in fig. 9.26a). From the energy difference to the energy gap, we assign this emission to the Mn acceptors.
We performed a fit on the PL peaks obtained at 20K, to define the different emission energies. Considering the sample 1523, with an As content of 57,9% (Fig.9.27), we found two peaks: the higher at 0,777 eV (Ep_2), likely related to the band emission energy (at 0,77 eV compared to literature at the same 20K), and a lower one at 0,744 (Ep_1). The difference was calculated as 33 meV, which agrees very well to the 34,4 meV Mn activation energy measured by Hall effect measurements. Therefore, we could conclude that this peak is connected to the Mn acceptor Energy level.

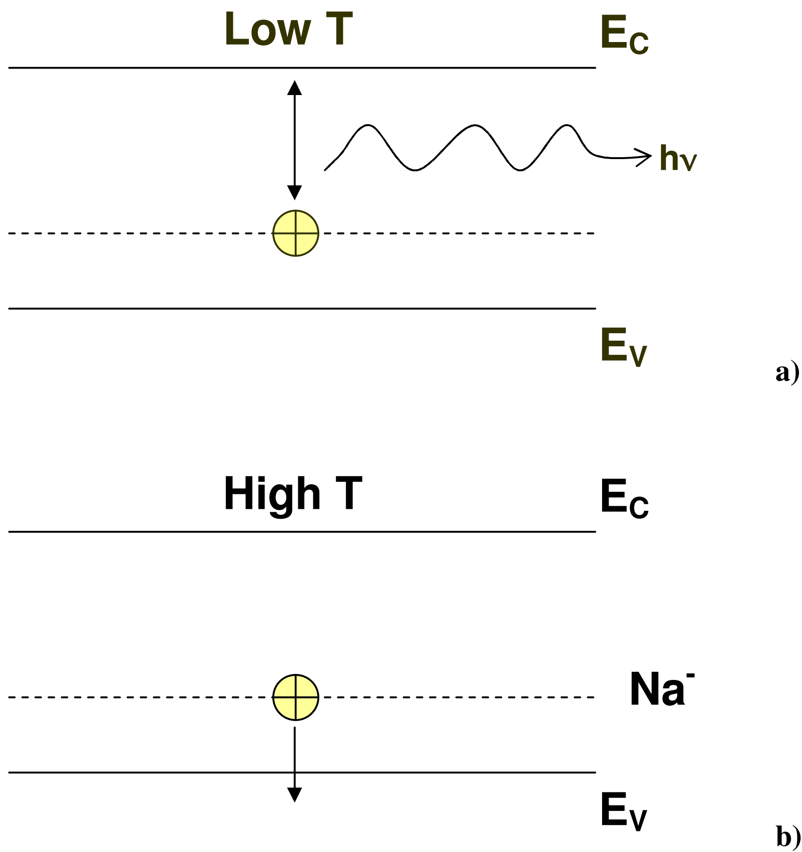

Fig.9.26: (a) At low temperatures the holes are frozen in the acceptor levels and radiative recombinations with the conduction band electrons are permitted; (b) At higher temperatures the holes are ionized and the emission related to radiative recombination conduction band to acceptor levels is damped.

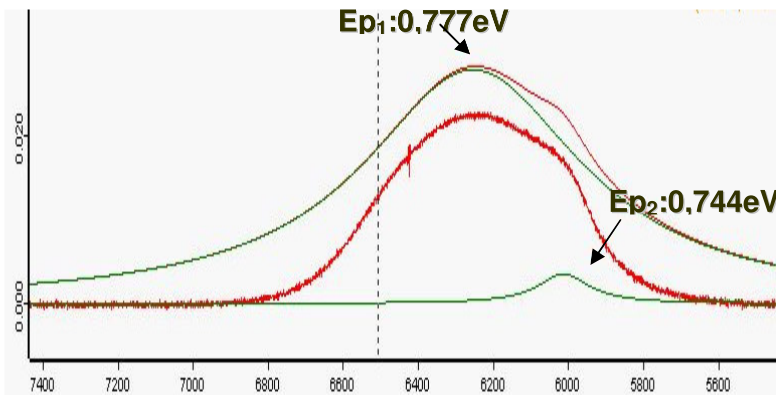

Fig.9.27: Fit on 1523 (As:57,5%)

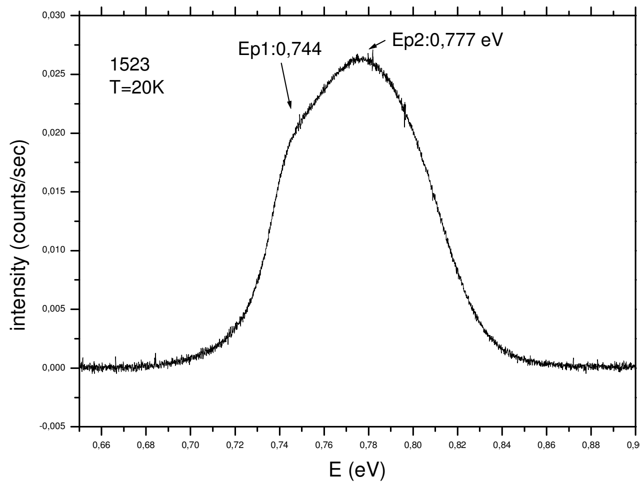

Fig.9.28: PL at 20K of the 1523 sample

The case of 1522 , at the highest As content of 61%, is similar. As shown in fig.9.29 we defined two peaks by the fitting and a difference Ep2-Ep1 of 13 meV (compared with 28,6 meV obtained from Hall effect measurements).

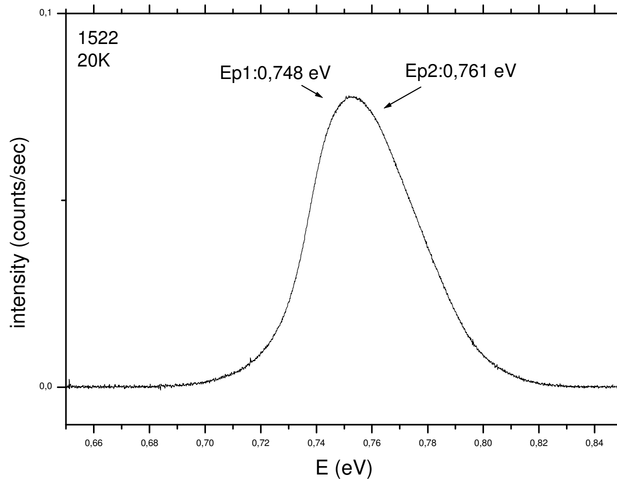

Fig.9.29: PL at 20K of the 1522 sample

If we analyse in details the peak features, fitting the curve, in the case of 1521 (Fig.9.30) we find a higher peak (probably band-band transition emission) and two lower energy peaks.

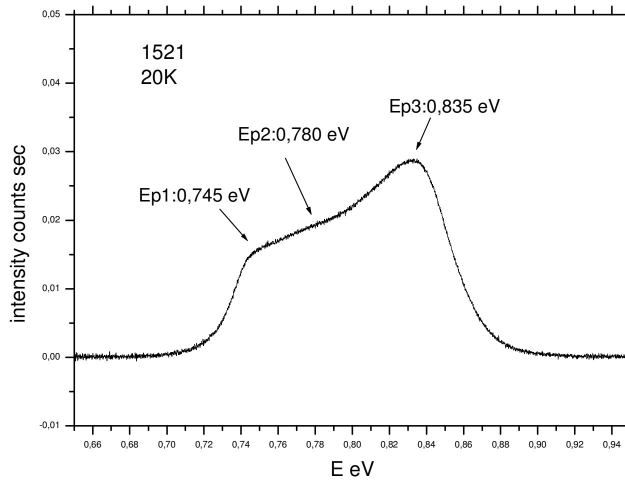

Fig.9.30: detail and fitted Energy peaks of 1521's PL at 20K

In this case the Energy difference between the mean peak (Ep_3) and the lower Energy peak (Ep_2) is calculated at 49 meV, near to the 38,6 meV resulted from Hall effect measurements. Maybe the other level, (Ep3-Ep1) at 90 meV is only optical and not electrical activated, since we don't notice a deeper centre in Hall effect measurement.

9.7 Conclusions

We have studied the InAsP:Mn system grown by MOVPE. The growth conditions were optimized by RAS in-situ analysis. First of all we found that InAsP on InP substrate showed a very fast surface reconstruction, observing that InP substrate was the best choice. Then we found that a BcpMn partial pressure must not exceed 10 mPa for doping to avoid cluster formations and surface deterioration during deposition. We systematically changed the As content in the InAsP alloy and checked the Mn activation energy by Hall Effect measurements and PL (fig.9.31). In this way we verified the Mn activation energy as an acceptor centre depends on InAsP composition. We obtained at maximum a p doping of $3X10^{18}cm^{-3}$, probably still too low to achieve magnetic effects.

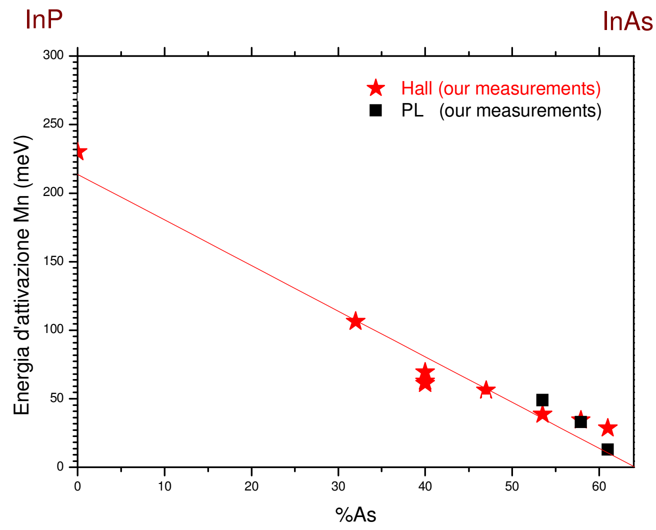

Fig.9.31: Energy activation of manganese in InAsP obtained by Hall effect measurements (stars), fit of the Hall data (line) and PL at 20 K (rectangles) as comparison.

Sample	TMIn Flow (Pa)	TBA Flow (Pa)	PH3 Flow (Pa)	DMn Flow (mPa)	Meas. As %	T(°C)	Holes Density	μ(cm2/Vs)	Ea(meV)
1504	1	1	195	10	47	600	$7{,}95X10^{17}$	19,85	51,6
1505	1	0,75	195	10	40	600	$5{,}71X10^{17}$	62,23	62,59
1506	1	0,87	195	10	43	600			
1509	1	0,80	195	10	44,8	600	$4{,}4X10^{14}$	22,37	No Mn
1513	1	0,80	195	40	40	600	$9{,}65X10^{17}$	42,68	69,35
1514	1	0,75	195	17	40	600	$6{,}38X10^{17}$	54,94	61,15
1515	1	0,37	195	13	32	600	$1{,}96X10^{17}$	62,3	106,4
1520	1	1,5	195	17	/	600			
1521	1	1,5	195	10	53,5	600	$9{,}1X10^{17}$	60,51	38,67
1522	1	1,75	195	10	61	600	$1{,}52X10^{18}$	49,32	28,6
1523	1	1,63	195	13-10	57,9	600	$1{,}36X10^{18}$	58,63	34,4

Table 9.1: InAsP Samples growth parameters and Electrical properties measured.

References IX

[9.1] M.Lampalzer et. Al. Journal of Cryst.Growth 248 (2003) 474-478

[9.2] Jürgen König et al. “Ferromagnetism in (III,Mn)-V Semiconductors“

[9.3] K.Huang and B.W.Wessels, Appl.Phys.Lett. 52 (1988) 1155-1157

[9.4] G.A.Antypas and T.O.Yep,J.Appl.Phys.55,2951 (1984)

[9.5] C.Kaspari, M.Pristovsek and W.Richter Phys.Stat.Sol. (b) 242, n.13, 2561-2569 (2005)

[9.6] M. Pristovsek, R. Jakomin, C.Meissner, M. Kneissl “Towards a magnetic semiconductor by MOVPE Tailoring Mn-Acceptor depth in InAsP” DGKK 2007, Marburg

[9.7] C.Goletti et.al. Phys.Rev.B vol.64 193301

[9.8] M.Zorn, T.Trepk, J-T Zettler, C.Meyne, K.Knorr, Th.Wethkamp, B.Juhno, M.Miller, L.Samuelson and W.Richter Indium Phosphide and related materials, 1996. IPMR ’96, pag. 586-589

[9.9] T.Hannappel et al. Journal of Chrystal Growth 221 (2000) 124-128

Conclusions

This PhD work had the purpose to investigate the properties of different kind of III-V In-P based semiconductors grown by MOVPE doped with transition metals, in particular Iron and Manganese. The centre of activity was the MOVPE growth, since the first step for every study was the materials optimization, concerning both undoped and doped layers. A systematic study regarding the research of the best deposition parameters was developed, involving analysis techniques, such as HRXRD, PL and Hall measurements.

At first InGaP/GaAs layers grown by MOVPE were studied. Several samples were grown with the aim to intercept the condition for a lattice match with the GaAs substrate and to minimize the background doping. The samples lattice matched grown (Indium concentration, 48,84%) showed a good quality, as proved by PL spectra that showed a really narrow FWHM, around 8 meV, comparable to the best results in literature. The minimum background doping was about $4{,}4X10^{15}$ cm^{-3} and, differently from the cases in literature, we found a p-type background doping, probably due to C-contamination derived from Metal-Organic precursors.

A doping optimization with Silicon was therefore carried out: we obtained a linear dependence of the Silicon doping, measured by Hall effect as a function of the Disilan flux. In this way a large range of doping samples, from $10^{16}cm^{-3}$ to $10^{19}cm^{3}$ was realized.

The n doped InGaP were then implanted with Iron especially with the intent to analyze the Iron's compensation effect and its lattice placement in the structure.

Conductivity/Voltage measures were necessary to verify the compensation effect: the Iron implanted samples showed a resistivity up to nine orders of magnitude higher than the as grown, with a transport mechanism governed by SCLC (space charge limited current), typical of a semi-insulating materials.

Putting in comparison samples treated with different annealing temperatures using an approach based on the Schmidlin-Roberts model, it could be argued that the 600°C annealing, differently from the 450°C annealing, takes effectively to a compensation caused by Iron implantation, probably thanks to the better recovering at higher temperature. In fact, the transport is not more dominated by donors traps but by the introduced Iron levels. Only in this latter case in fact, from calculations of the activation energy, an energy level placed at Ev+0,72 eVcan be derived. It has

been connected to Fe^{2+} species as reported in literature. Moreover, from PIXE and RBS analysis was possible to calculate the substitutional Iron fraction, as a function of the annealing temperatures. Though this fraction decreases, as expected, at higher temperatures, it remains quite high, between 30% and 50% even at 600°C (with a very high stable fraction considering the 10% observed in the InP case) and it is higher for previously more n-doped layers. We can therefore conclude that subsitutional Fe in InGaP is more stable than in InP and that the diffusion during annealing is also inhibited if the doping before implantation is higher.

Another part of the present study was oriented to improve implantation as a step of a technological process. In this case it is useful to analyse the influence between Iron implanted and the different doping elements introduced during MOVPE growth.
Therefore we performed a study on the MOVPE re-growth of Zn doped InP on Iron implanted InP substrates, to control the inter-diffusion effects between Zinc and Iron. We pursued a systematic study, similar to the previous one and at first we optimized the undoped material, in which an n-type background doping of about $8X10^{14}cm^{-3}$ was verified. Then we evaluated the high Zn diffusion effect through a model based on the second Fick's law. By performing SIMS profiles measures, we estimated a Zinc saturation in InP layers around $1,2X10^{18}cm^{-3}$ and a Zinc concentration value of $4X10^{17}cm^{-3}$ after which the diffusion toward the substrate occurs.
So that, the re-growth of InP:Zn by MOVPE on InP Iron implanted were performed in different conditions. Preliminary results show that if Zinc density is around $10^{17}cm^{-3}$, it does not diffuse into the substrate and it does not have any effect on the Fe profile.
On the other hand, in case in which Zinc density is around $2X10^{18}cm^{-3}$, it diffuses and influences the Fe implanted profile. Moreover, the Fe implanted prevents further Zn diffusion, which, therefore, tends to accumulate in the substrate near to the surface. This result shows an important effect connected to Iron implanted, that beyond a compensation element could act like a barrier for impurity diffusion in electronic devices.

The other system considered, InGaAs/InP is at the moment in a working state. Preliminary results show a difficulty to incorporate the right concentration high density of Indium (53%) as required to achieve lattice match. Some samples were grown, showing an Indium concentration below 47% or even more than 73%. However, using a different interface steps, mirror like samples were grown in spite of a not pseudomorphic deposition. These samples showed an interesting optical quality, a fairly narrow PL peak, whose FWHM was around 58 mev, in spite of a not pseudomorphic deposition.

In the final part of this PhD activity, developed in Berlin at the TU, we considered another type of transition metal dopant, Manganese, exploiting different properties respect to the Iron studied up to now.

In particular, Manganese in III-V semiconductors, can provide at the same time holes carriers and magnetic dipoles. Each of these is an indispensable element for achieving magnetic effects, dependent, as known, on spin-holes interactions. The motivation was therefore to explore the possibility to realize semiconductors materials and in particular diluted semiconductors materials, doping III-V semiconductors with a magnetic element. With the aim to avoid cluster formation, caused by the low solid solubility of Manganese in III-V semiconductors, instead of enhancing the Manganese concentration, another solution was evaluated. In particular, we studied a system like InAsP/InP, examining the possibility to change As concentration in the alloy, tailoring the manganese level depth in the band gap. In this system the activation energy, connected with the manganese level, decreases at higher As concentrations.

Firstly, we searched the best solution regarding the substrate. By monitoring in-situ the deposition with RAS analysis was possible to determine that the time of InAsP reconstruction on InP was absolutely faster than on GaAs, therefore we opted for the former one. Moreover, checking the signal connected to the total reflectance, we could estimate the maximum bcpMn's (precursor of manganese) pressure above which the surface would deteriorated, starting to origin a 3-dimensional kind reconstruction, probably connected to Mn-P or Mn-As clusters formation. We determined that a 10 mPa pressure would have probably prevented a clusters creation, so we chose this parameter for the following depositions. Several InAsP:Mn layers have been grown, with different As concentration (range between 32 and 61%). By trying approach as possible the level connected to Manganese to the valence band, a minimum activation energy of 28,6 meV was obtained. Moreover from Hall effect measurements we obtained the expected trend: a decreasing of the activation energy at higher Arsenic contents. With the purpose to confirm the effective role of Manganese we performed PL measurements at different temperatures on the InAsP samples, observing superimposed peaks, connected to different kinds of radiative transitions. Checking their different behaviour with the temperature and fitting the peaks, in the way to discriminate the different energies associated, we hypothesized that one process was caused by band-band transition and the other by conduction band- Mn acceptor's level transition. The PL energy connected to the Mn level, indeed, fairly agrees with the activation energy, calculated after Hall effect measurements. Considering that the InAsP:Mn growth is still in a developing phase, the achievement of the precise control of Mn activation energy, changing Arsenic concentration is certainly promising. The highest

holes concentration obtained was $4X10^{18}cm^{-3}$, probably still low to accomplish magnetic structures. Anyway, it seems that a narrow margin, with Arsenic between 61% and 65%, can be still explored to improve the carriers activation, moving the Mn level to a lower value than the minimum obtained (28,6 meV). This certainly will be matter of the following activity steps, together with improving of the contact qualities to investigate magnetic effects.

Another possibility will be the study of Mn implantation on this kind of materials, since as observed before, it can be useful to achieve higher doping concentrations, beyond the solid solubility and preventing clusters formation.

In the near future, this approach will be extended to different kind of III-V semiconductors, especially the already studied heterostructures based on InGaP, InP and InGaAs. In this way it would be interesting to explore the possibility of obtaining diluted magnetic semiconductors, exploiting the former experience in ion implantation (very promising as observed for GaN:Mn implanted, having Curie Temperatures next to RT), with the opportunity to compare it with the traditional doping experiments, investigated in the latter section.

Parts of this work have been published or presented in:

B.FRABONI, T. CESCA, A. GASPAROTTO, G. MATTEI, G: IMPALLOMENI, F. PRIOLO, **R. JAKOMIN**, M. LONGO, L. TARRICONE
"Electrical and structural characterization of Fe implanted InGaP"
PHYSICA B 401-402, 278-281, 2007

B. FRABONI, E. PIANA, T. CESCA, A. GASPAROTTO, M. LONGO**, R. JAKOMIN**, L. TARRICONE
"Deep level controlling the electrical properties of Fe implanted GaInP/GaAs".
APPLIED PHYSICS LETTER 90, 182106-1/182106-3, 2007

M. PRISTOVSEK**, R. JAKOMIN**, C.MEIβNER, M. KNEISSEL
"Toward a magnetic semiconductor by MOVPE: Tailoring Mn acceptor density depth in InAsP"
22nd DGKK Workshop (2007) - "Epitaxy of III/V Semiconductors"
06.12-07.12. in Marburg (D)

Thanks to….

Thanks to prof. Luciano Tarricone that gave me the possibility to be part of his group and to have a very beautiful experience, thanks him for what he taught me and for the patience and care with which he followed my work.

Thanks to Dr. Massimo Longo, who constantly followed me in my activity. I'm grateful for the enthusiasm and the helpfulness with which he shared his experience and I am happy that I could worked with him.

Thanks to Prof. Michael Kneissl that gave me the chance to work with his group, for his kindness and for being always open for discussions.

Thanks to Dr. Markus Pristovsek that taught me many things about MOVPE, RAS and many other scientific things. I am grateful for the opportunity to have worked with him.

Thanks to Dr. Renato Magnanini that introduced me to PL measurement and gave me the opportunity to learn the teaching approach with the students.

Thanks to Prof. Antonella Parisini for the interesting discussions about semiconductor properties and for being always kind and available to help me.

Thanks to Salvatore Vantaggio that with his many skills is not only valuable but essential. Thanks for his friendship, the coffee companionship and the frequent help for various things.

Thanks to Prof. Wolfgang Richter that introduced me to a wonderful experience in Berlin and that gave me always support and advices during my activity.

Thanks to Prof.Carlo Ghezzi that gave me some precious advices and for being always available for discussions.

Thanks to Prof. Andrea Gasparotto and Dr. Tiziana Cesca, from Padova University, that introduced me to ion implantation, RBS and PIXE analysis and that gave us the opportunity to work with them and their group.

Thanks to Dr. Beatrice Fraboni from Bologna University for I-V and DLTS electrical measurements and the chance to collaborate with her and her group.

Thanks to Dr. Enos Gombia and Dr. Roberto Mosca, from IMEM-CNR, for the electrical measurements and the possibility that they gave me to learn the ECV technique.

Thanks to Dr. Claudio Bocchi and Dr. Germini, from IMEM-CNR, for the HRXRD measurements.

Thanks to Ing. Nicola Del Monte and prof. Paolo Cova, from the Engineering Department of the Parma University, that gave me the possibility to work in their laboratory for photolithographic techniques.

Thanks to the new PhD. Student, Michele Baldini for his help and advices.

Thanks to the previous group students and their precious work, Dr.Stefano Rampino and Dr.Michele Begotti

Vielen herzlichen Dank an die gesamte Kneissl – Arbeitsgruppe:
particularly:
Thanks to Dr. Massimo Drago for his friendship, the support in Berlin life and all the things that he taught me about nitrides.
Thanks to Joachim Stellmach that supported me for HRXRD measurements and that was always very friendly and helpful.
Thanks to Christian Meißner that supported me in Hall measurements and helped me in many things, including brief german lessons.
Thanks to Raimund Kremzow and Martin Leyer that supported me during MOVPE activity in all the situations.

Grazie ad i miei genitori, a mio fratello Marcello ed ai miei amici, per tutto quello che rappresentano e che fanno per me.